Ancient TL

www.ancienttl.org · ISSN: 2693-0935

Issue 34(2) - December 2016
https://doi.org/10.26034/la.atl.v34.i2

ISSN 0735-1348

Ancient TL

A periodical devoted to Luminescence and ESR dating

Department of Physics, East Carolina University, 1000 East 5th Street, Greenville, NC 27858, USA
http://www.ecu.edu/cs-cas/physics/ancient-timeline/

December 2016, Volume 34 No.2

Ancient TL

Started by the late David Zimmerman in 1977

Ancient TL

IRSL dating of fast-fading sanidine feldspars from Sulawesi, Indonesia

Bo Li[1*], Richard G. Roberts[1], Adam Brumm[2,3],
Yu-Jie Guo[1], Budianto Hakim[4], Muhammad Ramli[5], Maxime Aubert[6,2],
Rainer Grün[2], Jian-xin Zhao[7], E. Wahyu Saptomo[8,1]

[1] Centre for Archaeological Science, School of Earth and Environmental Sciences
University of Wollongong, New South Wales, Australia
[2]Research Centre of Human Evolution, Environmental Futures Research Institute,
Griffith University, Queensland, Australia
[3] School of Earth and Environmental Sciences, University of Wollongong, New South Wales, Australia
[4] Balai Arkeologi Makassar, Indonesia
[5] Balai Pelestarian Cagar Budaya, Jambi, Indonesia
[6] Place, Evolution and Rock Art Heritage Unit (PERAHU), Griffith University, Queensland, Australia
[7] School of Earth Sciences, University of Queensland, Brisbane, Queensland, Australia
[8] Pusat Penelitian Arkeologi Nasional, Jakarta, Indonesia

[*]Corresponding Author: bli@uow.edu.au
Received: August 10, 2016; in final form: August 31, 2016

Abstract

The volcanic origin of the sediments from Sulawesi, Indonesia, provides a particular challenge for luminescence dating due to the dim optically stimulated luminescence (OSL) from quartz, and the high anomalous fading rate in the infrared (IR) stimulated luminescence (IRSL) from feldspars. In this study, we present results of dating the sanidine feldspars from 2 samples taken from an archaeological site (Leang Bulu Bettue) in the Maros karsts of South Sulawesi. We tested the post-IR IRSL (pIRIR) procedures in order to find a stable luminescence signal that is less affected by anomalous fading. It was found that there is a highly variable anomalous fading rate in the IRSL and pIRIR signals for different grains and aliquots, and a low temperature IR stimulation (at 50 °C or 100 °C) used in a pIRIR procedure cannot completely remove the anomalous fading for the subsequent pIRIR signals. The large uncertainties associated with fading rates prevent the application of fading-correction procedures. We propose a method to obtain reliable D_e estimates by extrapolation of the relationship between D_e and laboratory fading rate (g-value). The resultant luminescence ages show consistency with other radiometric age determinations from the site. Our results suggest that a systematic and detailed investigation of the relationship between D_e and anomalous fading rate for different grains or aliquots is necessary for dating volcanic feldspars.

Keywords: Post-IR IRSL, Volcanic feldspars, Sanidine, Luminescence dating, Sulawesi, Indonesia

1. Introduction

Although luminescence dating has been successfully applied to many kinds of sediments from various environmental settings, dating the quartz and feldspar grains from volcanic provinces has proved challenging. One of the main reasons for this difficulty is that quartz from volcanic regions commonly emits a dim OSL signal, or no signal at all (e.g., Berger & Huntley, 1994; Fattahi & Stokes, 2003; Westaway & Roberts, 2006). The luminescence signals of feldspars are usually brighter than those of quartz from volcanic regions;

however, a high anomalous fading rate is usually observed for the blue luminescence from volcanic feldspars (Wintle, 1973; Tsukamoto & Duller, 2008; Tsukamoto et al., 2011).

Recent progress on understanding anomalous fading for feldspar provides the possibility of isolating a non-fading component in IRSL for feldspars, using either a post-IR IRSL (pIRIR) approach (Thomsen et al., 2008) or a multiple-elevated-temperature (MET) pIRIR procedure (Li & Li, 2011). These pIRIR procedures have been widely tested and applied to sediment samples from different regions in the world (see Li et al., 2014, for a comprehensive review of the progress, potential and remaining problems in using these pIRIR signals for dating). Tsukamoto et al. (2014) successfully applied a pIRIR procedure to date volcaniclastic sediments (lahar deposits) from alkaline basalts in Italy. These authors found that the laboratory fading rates of IRSL from feldspars in their samples of scoria fallout and lahar deposits can be largely reduced by applying a high preheat temperature and pIRIR stimulation temperatures, suggesting that the pIRIR method may provide a potential method for dating sediments of volcanic origin.

Previous efforts to date sediments of volcanic origins from Indonesia have used red TL or ultraviolet OSL signals from quartz, and IRSL signals from potassium-rich feldspar (K-feldspar). The OSL signals are, in general, too dim for dating purposes (Morwood et al., 2004; Roberts et al., 2009). The light-sensitive component of the red TL signal is less easily bleached than the OSL or IRSL traps, is small in size and is obtained by subtraction, resulting in imprecise and potentially inflated ages (Westaway & Roberts, 2006). The IRSL signals measured previously showed exceptionally high rates of anomalous fading and a suitable correction could not be applied. It is not until recently that the newly developed pIRIR and MET-pIRIR procedures were successfully applied to date the sediments from this region, including at the open-air site of Talepu in the Walanae Depression of South Sulawesi, which registers the earliest known presence of hominins on this island (van den Bergh et al., 2016), and at the *Homo floresiensis* type-site on Flores, the limestone cave of Liang Bua (Sutikna et al., 2016).

In this study, we tested and applied different pIRIR procedures to date volcanic sanidine extracts from the sediments from an archaeological site, Leang Bulu Bettue, on Sulawesi.

2. Study site and samples

The limestone karst border plains of Maros are located on the southwestern peninsula of the island and cover an area of approximately 400 km^2. This region contains some of the oldest surviving rock art on the planet, as demonstrated by recent U/Th dating of coralloid speleothems overlying hand stencils and large animal paintings (Aubert et al., 2014). The oldest dated rock art motif (a hand stencil) yielded a minimum age of 39.9 ka (Aubert et al., 2014). Prior to the present research, the oldest excavated archaeological findings in Maros dated to 35.6–34.5 thousand calibrated radiocarbon years before present (cal. ka BP), as revealed by excavations at Leang Burung 2 rock-shelter (Glover, 1981). Some 20 km to the north, where the karst outcrops in the adjoining Pangkep district, excavations at Leang Sakapao 1 yielded *in situ* stone artefacts and shellfish remains with a maximum age of 30–20 cal. ka BP (Bulbeck et al., 2004). In 2013–2015, we conducted deep-trench excavations at a previously uninvestigated Maros site, Leang Bulu Bettue (Fig. 1a and b), yielding cultural deposits that may exceed in antiquity the oldest evidence for humans in this karst region.

The tunnel-like cave mouth at Leang Bulu Bettue is 4 m wide and the roof at the mouth measures 3 m in height, while the interior chamber is 27.3 m long, 12.6 m wide and up to 9.2 m high (Fig. 1c). The excavated area is located just inside the entrance to the cave shelter and in an adjoining rock-shelter (inside the dripline). Our trench exposed a deeply stratified and undisturbed sequence of sedimentary layers (Fig. 1d). The archaeological contents of these layers will be reported in detail in a separate study. We provide here a brief summation of the stratigraphic sequence and cultural contents as they pertain to the uppermost (i.e., youngest) deposits (Layers 1–5), relevant to the present study. The chronological samples (i.e., radiocarbon, U-series and luminescence) were taken from the west and south wall profiles. Here we show the west wall profile only (Fig. 1d), so that all the chronological samples can be shown on a single section. Excavations into a deeper series of deposits below Layer 5, and efforts to establish a chronology for this earlier part of the stratigraphic sequence, are still ongoing.

Below the topmost layer, a thin Neolithic level (Layer 1), are cemented flowstones intercalated with calcite-rich silts (Layers 2–3). This capping flowstone unit is underlain by thin silty clays (Layers 4a and 4b) that slope downwards from the rear of the cave and level out and thicken in the main shelter, where they inter-finger with localised ashy lenses (Layers 4c–e). This combined sequence is 1.5 m thick. Below this is a 50 cm-thick sandy clay (Layer 4f) that is preserved only near the eastern wall of the cave, and which is underlain by a 50 cm-thick sandy clay (Layer 5). Layers 4a–f yielded rich cultural remains, including abundant evidence for pigment processing and use. Stone artefacts and fossil fauna are present in much lower densities in Layer 5. The chronology of the upper part of the Leang Bulu Bettue section (Layers 1–5) was established using AMS ^{14}C dating of freshwater gastropod (*Tylomelania perfecta*) shells, solution multi-collector inductively coupled plasma mass spectrometry (MC-ICP-MS) U- series dating of *in situ* stalagmites, laser ablation (LA) U-series dating of faunal remains, and luminescence dating. The location and results of the chronological samples are shown in Fig. 1d.

Layer 1 has a maximum radiocarbon age (on *in situ* charcoal) of 1.7–1.6 cal. ka BP (Wk-37740). No charcoal or other plant carbon or materials suitable for ^{14}C-dating was found below Layer 1. However, several stalagmites were recovered from the upper surfaces of both Layers 4a and 4b. These speleothems were intact, still in upright position, and had formed on top of cemented pedestals of brecciated archae-

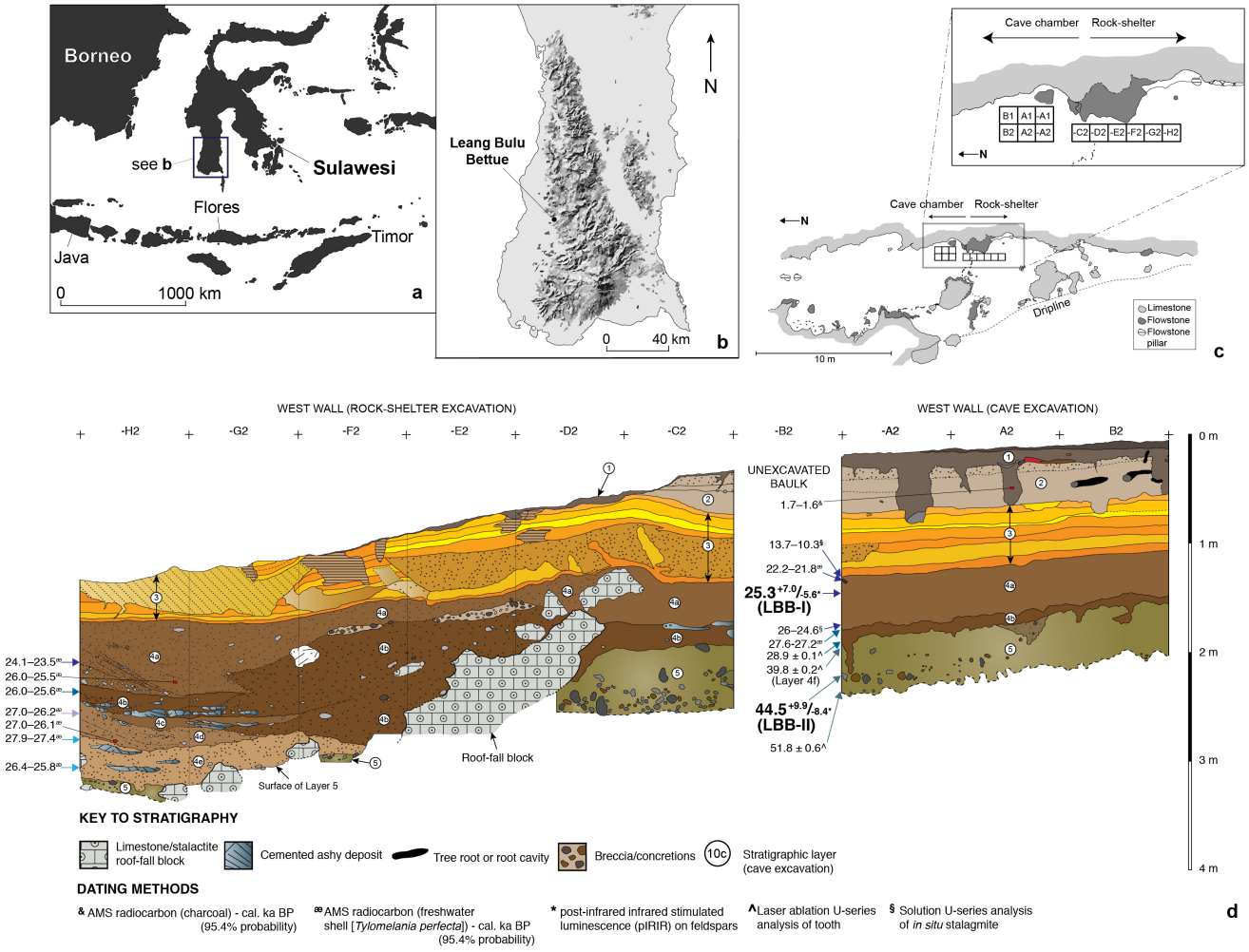

Figure 1. (a and b) Location of Leang Bulu Bettue in the Maros karsts of Sulawesi, Indonesia. (c) Plan of Leang Bulu Bettue indicating the location of the excavations. (d) Stratigraphic profile of the west walls of the excavated trenches. Sample locations and resultant age determinations for luminescence samples LBB-I and LBB-II, as well as stalagmites and (most) faunal remains, are shown projected on the west trench faces at approximate depths and according to stratigraphic layer, rather than in the original sample locations. Sample LBB-I was collected from the south wall of Square A2 and LBB-II was collected from the south wall of Square A1 (sections not shown here). The date for Layer 4f is shown in relative stratigraphic position as Layer 4f is only evident in the southeast walls of the excavated trenches (not shown here). With the exception of the calibrated radiocarbon ages, all age determinations are reported in thousands of years (ka).

ological sediment, indicating that they are *in situ* and not redeposited from other locations within the cave. Solution MC-ICP-MS U-series dating of a 30 cm high mound-like stalagmite that grew on the upper surface of Layer 4a shows that this speleothem formed between 13.7 ka to 10.3 ka ago, with the former providing a minimum age for this deposit. An 18 cm high stalagmite from the top of underlying Layer 4b was also dated using the solution MC-ICP-MS U-series technique. This stalagmite formed between 26 ka to 24.5 ka ago, allowing us to bracket the time-depth of Layer 4a to between 13.7 ka and ~26 ka ago. A *T. perfecta* shell recovered *in situ* from close to the top of Layer 4a (131 cm depth), ~10 cm below the cemented pedestal of archaeological detritus underlying the Layer 4a dated stalagmite, yielded an AMS ^{14}C age of 18,126 ± 51 BP (22.8–21.8 cal. ka BP at 2σ). This ^{14}C date is consistent with the associated speleothems earliest known growth stage (13.7 ± 1.8 ka), and hence we contend that it provides a reasonable estimate for the upper age of Layer 4a (i.e., ~22.3 cal. ka BP).

Furthermore, a pig molar recovered *in situ* from Layer 4b yielded a minimum LA U-series age of 28.9 ± 0.1 ka, which is consistent with the stalagmite chronology. Layers 4b–e span ~30–26 ka, as inferred from solution MC-ICP-MS U-series dating of the overlying stalagmite, LA U-series analysis of faunal remains, and AMS ^{14}C dating of *T. perfecta* shells. An anoa tooth from Layer 4f yielded a minimum LA U-series age of 39.8 ± 0.2 ka, suggesting this unit spans ~40–30 ka. Similarly, LA U-series analysis of a bovid molar from the base of Layer 5 provided an in- sequence minimum age of 51.8 ± 0.6 ka.

To contribute further to the accuracy and reliability of the chronology for this site we conducted and tested the IRSL

and pIRIR procedures on two sedimentary samples taken from Layers 4a and 5, respectively, from the south wall profile. The uppermost sample LBB-I was collected from the middle of the Layer 4a, which, as already noted, is bracketed by the stalagmite and *T. perfecta* shell recovered for ^{14}C dating from the upper part of Layer 4a and the stalagmite from atop the underlying unit, Layer 4b. Sample LBB-II was collected from the middle of Layer 5. Both samples were taken by hammering 20-cm long opaque plastic tubes (5 cm in diameter) into the cleaned section face. The tubes were removed and wrapped in light-proof plastic for transport to the Luminescence Dating Laboratory at the University of Wollongong. Additional bags of sediment were collected from the tube holes and sealed in zip-lock plastic bags for laboratory measurements of sample radioactivity and field water content (see Sec. 3).

Under dim red laboratory illumination, each sample was treated using standard procedures to extract sand-sized grains of K-feldspar (Aitken, 1998). First, any carbonates and organic matter were removed using solutions of HCl acid and H_2O_2, respectively. The remaining material was then dried and mineral grains of 90–180 μm and 180–212 μm in diameter were separated by sieving. The sanidine feldspar grains were isolated from quartz and heavier minerals (using a sodium polytungstate solution of density 2.58 g/cm^3) and then etched in 10 % HF acid for 40 min to clean the grain surfaces and remove (or greatly reduce in volume) the outer α-irradiated layer of each grain. The etched sanidine feldspar grains were given a final rinse in HCl acid to remove any precipitated fluorides, and were then dried.

3. Environmental dose rate determination

Mineralogy analysis of the sediments from Leang Bulu Bettue suggests that the stratigraphic units exhibit a homogeneous pyroclastic composition dominated by calcite and sanidine feldspars (from ~20 % to ~80 %), and negligible quartz (only ~1–2 %). The high percentage of sanidine feldspars in mineral composition of the sediments from Leang Bulu Bettue indicates that these feldspars are likely to be volcanic and to originate from the Camba Formation in the highlands to the east of the Maros karsts (McDonald, 1976).

The dose rate for the K-feldspars consists of 4 components: the external gamma, β- and cosmic-ray dose rates, and the internal β-dose rate. The γ-dose rate was not measured in the field, so we estimated this component from thick-source alpha counting (TSAC) measurements of U and Th and from X-ray fluorescence (XRF) measurements of K using sediments collected from the 30-cm sphere surrounding the sampling tubes, which captures the penetrating range of most gamma rays in sediments. The β-dose rate was measured directly by a Risø GM-25-5 multicounter system (Bøtter-Jensen & Mejdahl, 1988; Jacobs & Roberts, 2015) using the sediment samples recovered from each tube. The minor contribution from cosmic rays was estimated from the burial depth and water content of each sample, the thickness of cave roof overhead (~80 m), the zenith angle dependence of cosmic rays, and the latitude, longitude and altitude of Leang Bulu Bettue (Prescott & Hutton, 1994). These external components of the total dose rate were adjusted for sample water content, using the measured (field) water content of each sample (which ranged from 29 % to 35 %) and also an assumed water content of 30 % for all samples; in all cases, we used a value of $\pm$ 5 % as the standard error of the mean to capture the likely range of time-averaged values for the entire period of sample burial. For the internal dose rate calculation, a K concentration of 10 $\pm$ 2 % (following Smedley et al., 2012) is assumed based on the theoretical K concentration of 10.69 % for sanidine, and a Rb concentration of 400 $\pm$ 100 ppm was assumed (Huntley & Hancock, 2001). The dosimetry data for all samples are summarised in Table 1.

4. Equivalent dose determination

4.1. Luminescence equipment

IRSL measurements were made using an automated Risø TL-DA-20 reader equipped with IR diodes (870 Δ 40 nm) for stimulation (Bøtter-Jensen et al., 2003). These delivered a total IR power of ~135 mW/cm^2 to the sample position. Irradiations were carried out using a ^{90}Sr/^{90}Y β-source mounted on the reader. IRSL signals were detected using an Electron Tubes Ltd 9235B photomultiplier tube fitted with Schott BG-39 and Corning 7-59 filters to transmit only wavelengths of 320–480 nm. Aliquots were prepared by mounting the etched K-feldspar grains as a monolayer of ~5 mm diameter in the centre of a 9.8 mm diameter stainless steel disc, using Silkospray silicone oil as an adhesive; this resulted in each aliquot containing several hundred grains. It is noted that we have measured 1,000 individual grains from sample LBB-I using an IR laser (830 Δ 10 nm, 400 W/cm^2) (Bøtter-Jensen et al., 2003), and we found that less than 1 % of the grains gave detectable IRSL signals. So we consider that the IRSL signal from single aliquot containing a few hundred grains may likely to be emitted from only one or a few grains.

4.2. Single-aliquot pIRIR procedures

In this study, the samples were firstly analysed using the multiple elevated temperature (MET) pIRIR procedure of Li & Li (2011). This procedure utilises the IRSL signals measured by progressively increasing the stimulation temperature from 50 °C to 250 °C in steps of 50 °C. Li & Li (2011) reported that the sensitivity-corrected MET-pIRIR signals obtained at elevated temperatures (> 200 °C) exhibited negligible rates of anomalous fading, thereby avoiding the need for any fading correction. This procedure was successfully applied to date the sediments from the Talepu site on the same island (van den Bergh et al., 2016). However, our initial measurements of K-feldspar extracts from the Leang Bulu Bettue samples revealed that they emitted very weak IRSL signals, which prevented D_e determination using the MET-pIRIR procedure. Fig. 2a shows typical MET-pIRIR signals

Table 1. Burial depths, grain sizes, water contents, dosimetry data, D_e and ages for the sanidine feldspar samples from Leang Bulu Bettue.

Sample	**Depth** (cm)	**Grain size** (μm)	**Water content** (%)	$\dot{D}_\gamma$ (Gy/ka)	$\dot{D}_{\beta_{external}}$ (Gy/ka)	$\dot{D}_{\beta_{internal}}$ (Gy/ka)	$\dot{D}_{cosmic}$ (Gy/ka)	$\dot{D}_{total}$ (Gy/ka)	**Isochron** D_e[(a)] (Gy)		**Age**[(b)] (ka)	
									$IRSL_{100}$ & $pIRIR_{290}$	$pIRIR_{290}$	$IRSL_{100}$ & $pIRIR_{290}$	$pIRIR_{290}$
LBB-I (Layer 4a)	160	180–212	30 ± 5 (29)	2.258 ± 0.106	2.642±0.205	0.67 ± 0.15	0.08 ± 0.01	5.65 ± 0.28	87^{+12}_{-10}	153^{+39}_{-31}	$13.7^{+2.2}_{-1.9}$	$25.3^{+7.0}_{-5.6}$
LBB-II (Layer 5)	197	90–180	30 ± 5 (30)	2.178 ± 0.097	2.222 ± 0.170	0.48 ± 0.13	0.07 ± 0.01	4.95 ± 0.23	200^{+26}_{-23}	230^{+48}_{-40}	$38.4^{+5.6}_{-5.0}$	$44.5^{+9.9}_{8.4}$

[(a)]The isochron D_e were obtained from the intercepts of the pink lines ($pIRIR_{290}$) and blue lines ($IRSL_{100}$ and $pIRIR_{290}$) on the y-axis in Fig. 8. The error terms are 1 σ.

[(b)]The final ages are those obtained from $pIRIR_{290}$ signals. All the ages were calculated by subtracting the residual doses from corresponding D_e values.

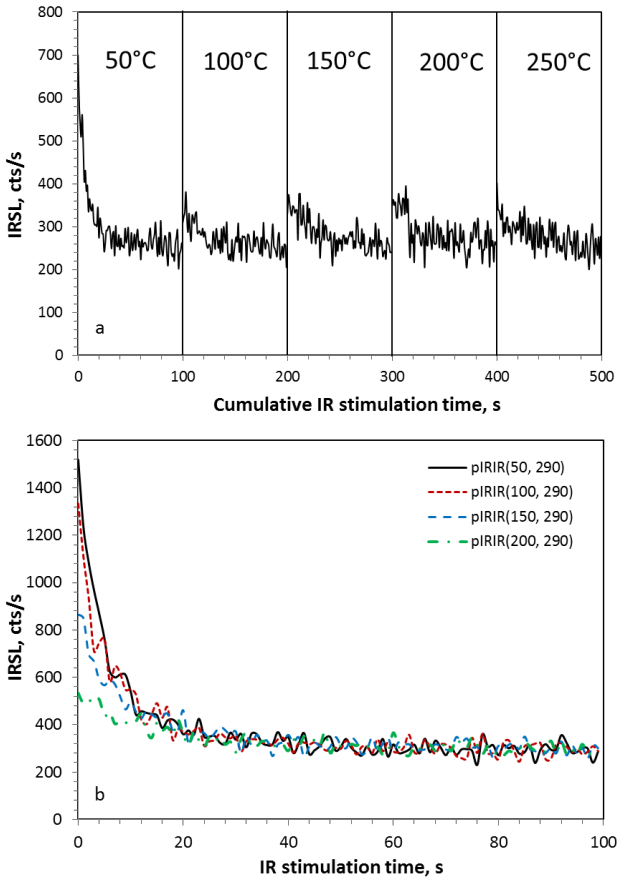

Figure 2. (a) Typical natural MET-pIRIR curves for K-feldspar grains from sample LBB-II, measured at different stimulation temperature (as indicated above each curve). (b) Typical $pIRIR_{290}$ signals from the same sample obtained after IR bleach at different temperatures from 50 °C to 200 °C.

observed for sample LBB-II at different stimulation temperatures. Even at a stimulation temperature of 250 °C, the decay of MET-pIRIR signal is negligible, presumably due to the cumulative loss of signal following multiple stimulations at lower temperature. As a result, we could not date the Leang Bulu Bettue samples using the MET-pIRIR procedure.

To measure the dim feldspar grains at Leang Bulu Bettue, we tested the two-step $pIRIR_{290}$ procedure of Thiel et al. (2011) (Table 2), in which an IR bleach is given at a low temperature (e.g., ∼50 °C) before the IRSL signal is measured at a high temperature (290 °C), because the $pIRIR_{290}$ signal is usually more intense than the 250 °C MET-pIRIR signal. It was suggested that a small rate of fading of the $pIRIR_{290}$ signal has a negligible effect on the calculated age of samples with D_e values less than ∼500 Gy (Li & Li, 2012), so it is hoped that the $pIRIR_{290}$ procedure should produce reliable estimates of D_e for the Leang Bulu Bettue samples. Fig. 2b shows the typical $pIRIR_{290}$ signals obtained after IR bleach at different temperatures from 50 °C to 200 °C. Here we will use the term $pIRIR_{(T1,T2)}$ to refer to the temperatures used in the different two-step pIRIR procedures - where T1 is the first IR stimulation temperature and the T2 is the post-IR

Table 2. The two-step $pIRIR_{290}$ procedure

Step	Treatment	Observed
1	Give regenerative dose[(a)]	
2	Preheat at 320 °C for 60 s	
3	IRSL measurement at T1 for 200 s	$L_{x(T1)}$
4	IRSL measurement at T2 (290 °C) for 200 s	$L_{x(290C)}$
5	Give test dose	
6	Preheat at 300 °C for 60 s	
7	IRSL measurement at T1 for 200 s	$T_{x(T1)}$
8	IRSL measurement at T2 (290 °C) for 200 s	$T_{x(290C)}$
9	IR bleach at 325 °C for 100 s	
10	Return to step 1	

[(a)]For the natural sample, the given dose = 0 Gy and the observed signals are L_n and T_n. The procedure is repeated for several regenerative doses, including a zero dose and a repeat dose.

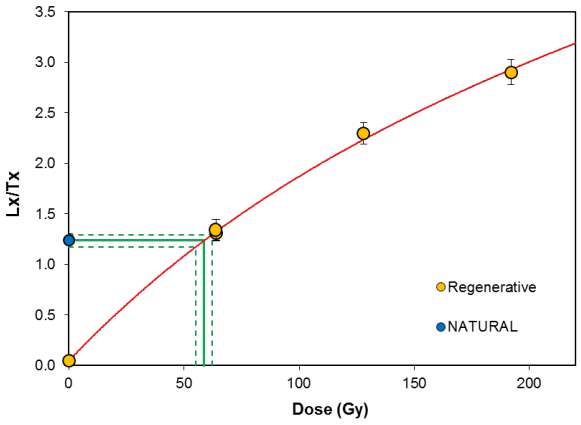

Figure 3. (a) Typical dose response curve for a single aliquot of LBB-II, showing the sensitivity-corrected $pIRIR_{(50,290)}$ natural and regenerative dose signals. The curve has been fitted to the regenerative dose data using a saturating exponential function.

stimulation temperature (T2 is fixed at 290 °C in our study). As seen from Fig. 2b, much brighter pIRIR signals were observed at a stimulation temperature of 290 °C, especially for $pIRIR_{(50,290)}$ and $pIRIR_{(100,290)}$ signals, which allowed the D_e to be determined with a reasonable precision. We also noted that the signal intensity decreases significantly as the first IR stimulation temperature is above 100 °C (e.g., 150 °C and 200 °C). We, therefore, focus on the $pIRIR_{(50,290)}$ and $pIRIR_{(100,290)}$ signals only in the following study.

4.3. D_e estimation using the $pIRIR_{(50,290)}$ procedure

The D_e values of the Leang Bulu Bettue samples were firstly measured using the $pIRIR_{(50,290)}$ procedure with a preheat at 320 °C for 60 s following either natural or regenerative doses and test doses. Typical dose response curve for one of the aliquots from LBB-II is shown in Fig. 3. The extent of recuperation and the recycling ratio are obtained routinely during construction of the dose response curve for D_e estimation (Fig. 3). It is found that, for most of the aliquots, the recycling ratios are consistent with unity and recuperation values are generally less than 10 % (i.e., the signal intensity measured after a zero dose relative to the natural intensity). Those aliquots that had recycling ratio outside the range 0.90–1.10 were discarded for D_e determination.

The $pIRIR_{(50,290)}$ D_e values obtained for LBB-I are shown in Fig. 4. A wide range of D_e values is observed for all of the samples; that is, the over-dispersion (OD) values of the distributions range from 50 % to 80 %. Based on the pattern of the D_e distribution, it may suggest that the sample might suffer from incomplete bleaching prior to burial. In this case, the minimum age model (MAM) could be applied to estimate the D_e values (Galbraith et al., 1999; Galbraith & Roberts, 2012). To test whether or not incomplete bleaching is the reason for the broad D_e distribution, the MAM was applied to estimate age for sample LBB-I, and compared with the U-series ages for the stalagmites and the ^{14}C age for the *T. perfecta* shell taken from the same layer (Fig. 1). Assuming an OD value of 20 % for well bleached samples, the MAM yield a D_e value of 10.7 ± 3.6 Gy, corresponding to an age of 2.0 ± 0.7 ka. This age, however, significantly underestimates the U-series time range of the stalagmite from atop Layer 4a, which is estimated to have formed between 13.7 ka and ∼26 ka ago. Similarly, a MAM age of 2.8 ± 1.3 ka was obtained for the sample LBB-II. This sample was taken from layer 5, which is below the two dated stalagmites, so it is expected to be older than ∼30–40 ka. Hence, the MAM ages of both LBB-II and I clearly underestimate the true ages by a substantial margin. We noted that assuming a different OD value ranging from 10 % to 30 % does not change the results significantly. We therefore conclude that the MAM should not be applied to estimate D_e values for our samples and incomplete bleaching is not the main reason for the broad D_e distributions observed.

An alternative explanation for the wide spread of D_e values is that there was a significant mixture of grains of different ages. This is, however, also unlikely because the stratigraphy of the section is horizontal and shows no evidence of post-depositional disturbance (Fig. 1d). Multiplying the dose rate of LBB-I by the ^{14}C age (∼22 ka) for the *T. perfecta* shell from the upper part of Layer 4a and the U-series age (∼26 ka) of the stalagmite from the upper surfaces of Layer 4b allows us to estimate the expected D_e value for the sample LBB-I, which lies between ∼125 Gy and ∼148 Gy. If we compare the $pIRIR_{(50,290)}$ D_e values from individual aliquots of sample LBB-I with the expected D_e (see Fig. 4), it is observed that most of the $pIRIR_{(50,290)}$ D_e values are underestimated. Since one of the most possible reasons for underestimation in IRSL dating of feldspar is anomalous fading, the underestimation in $pIRIR_{(50,290)}$ D_e values suggest that the $pIRIR_{(50,290)}$ may also suffer from anomalous fading. To confirm this, 8 aliquots from sample LBB-II were measured for an anomalous fading test. A single-aliquot measurement procedure similar to those described by Auclair et al. (2003), but based on the $pIRIR_{(50,290)}$ procedure, was applied. The fading rates (g-values) were calculated for the $pIRIR_{(50,290)}$ signal and normalised to the time of prompt measurement

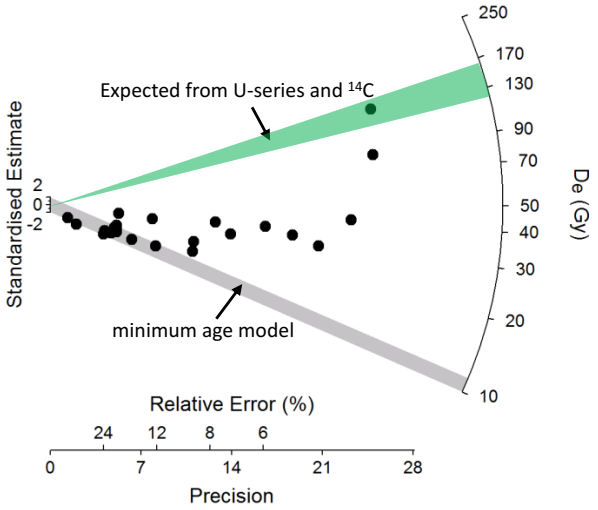

Figure 4. Radial plots showing the D_e distributions of the $pIRIR_{(50,290)}$ signals for the sample LBB-I. The green shaded area shows the expected D_e range based on multiplying the dose rate of LBB-I by the U-series ages of the two stalagmites from the upper surfaces of both Layers 4a and 4b. The grey shaded area shows the D_e value calculated using the minimum age model (MAM).

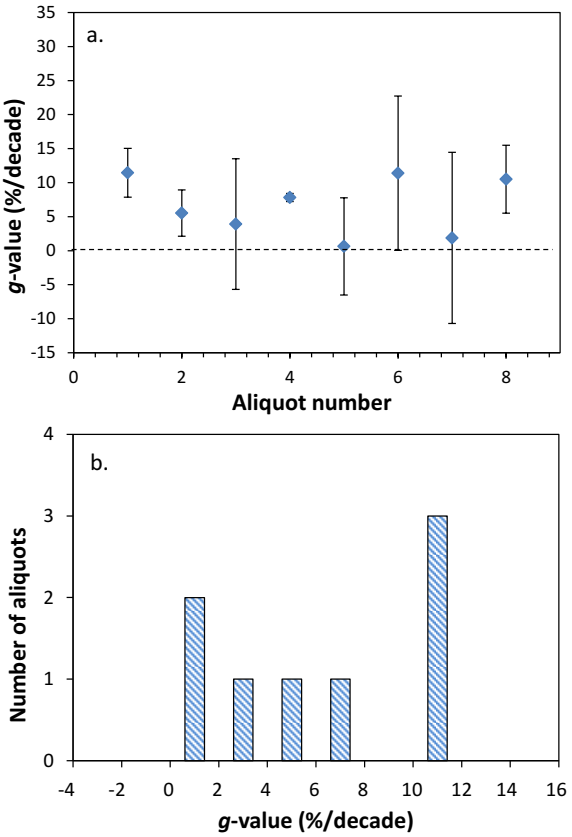

Figure 5. (a) The g-values of $pIRIR_{(50,290)}$ signals for 8 aliquots from sample LBB-II. (b) Histogram of the g-values shown in (a).

of the IRSL signal (t_c = 970 s). The g-values obtained are shown in Fig. 5a for individual aliquots and are summarised in the histogram in Fig. 5b. As demonstrated in Fig. 5a and Fig. 5b, a large range of g-values is observed, from a negligible value consistent with zero to a much higher value of ~12 %/decade, although the g-values are generally associated with large uncertainties due to the low signal intensity of our samples. The results indicate that the anomalous fading rates of the $pIRIR_{(50,290)}$ signals are highly variable among different aliquots or grains, which could result in the large variation in the D_e values shown in Fig. 4. We conclude, therefore, that an IR bleaching at 50 °C for 200 s is not sufficient to remove the signals associated with the easy-to-fade traps for our samples. It should be noted that the 50 °C IRSL signals are too dim to allow for reliable estimation of fading rates.

4.4. D_e estimation using the $pIRIR_{(100,290)}$ procedure

It has been demonstrated that the stimulation temperature in the prior IR stimulation may play an important role in reducing anomalous fading for the pIRIR signals (Li & Li, 2011). Li & Li (2012) suggested that an IR stimulation at 50 °C may be insufficient to remove all of the easy-to-fade signals, but increasing the prior-IR stimulation temperature may be helpful to remove the fading component more effectively. Li & Li (2012) suggested that an IR stimulation at 200 °C is sufficient to remove all the easy-to-fade signals for their Chinese loess samples. Unfortunately, however, the dim IRSL signal from Leang Bulu Bettue prevents the application of a high IR stimulation up to 200 °C. As demonstrated in Fig. 2b, a prior IR stimulation at 150 °C or above results in a significant drops in the intensity of the subsequent $pIRIR_{290}$ signals. Instead, a prior IR stimulation at 100 °C does not reduce the subsequent $pIRIR_{290}$ signal considerably. We therefore adopted the $pIRIR_{(100,290)}$ procedure to test whether it is possible to reduce the anomalous fading rate in the $pIRIR_{290}$ signal for our samples more effectively.

We first chose the sample LBB-I to test the $pIRIR_{(100,290)}$ procedure, as the age of this sample is well confined by the U-series stalagmite and ^{14}C ages from the same layer (Layer 4a). A total of 40 aliquots were measured and their corresponding $pIRIR_{(100,290)}$ D_e values were summarised in radial plot (Fig. 6a) and histogram (Fig. 6b), respectively. For comparison, the $pIRIR_{(50,290)}$ D_e values from 23 aliquots from the same sample were also shown in the same figures. As seen, it appears that increasing the prior IR stimulation from 50 °C to 100 °C do help to increase the D_e values in the $pIRIR_{290}$ signals. For example, the $pIRIR_{(100,290)}$ D_e values are systematically higher than the $pIRIR_{(50,290)}$ D_e values (Fig. 6b). However, a large scatter is still observed in the $pIRIR_{(100,290)}$ D_e values and most of them are still significantly underestimated when compared to the expected value based on the U-series and ^{14}C ages (Fig. 6a). The results indicate that the $pIRIR_{(100,290)}$ procedure may be able to reduce the fading component more effectively than the $pIRIR_{(50,290)}$ procedure, but it still cannot completely remove the fading component.

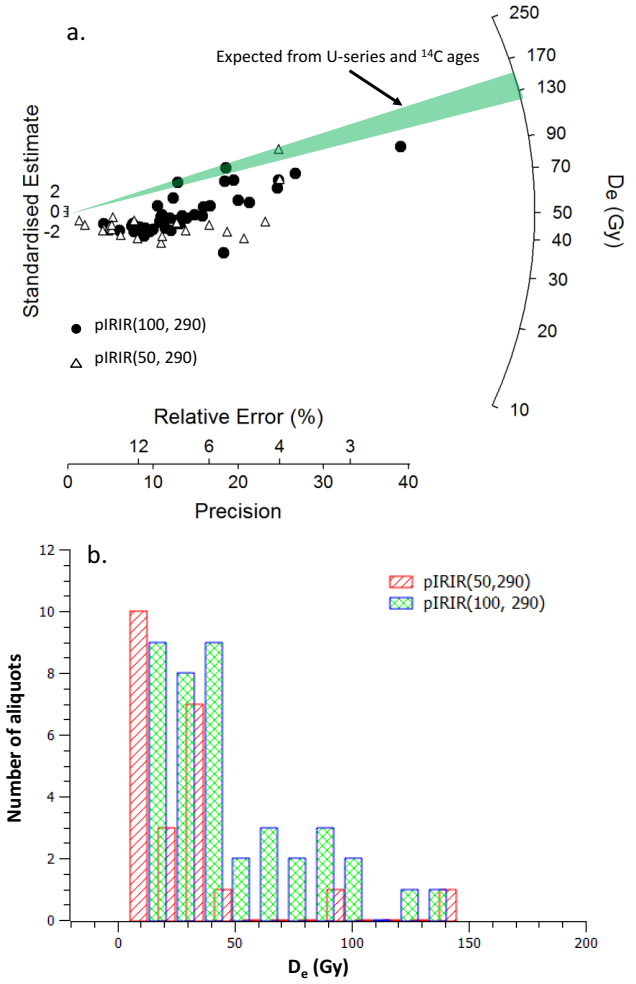

Figure 6. (a) Radial plot showing the D_e distributions of the $pIRIR_{(50,290)}$ and $pIRIR_{(100,290)}$ signals for LBB-I. The green shaded area in (a) shows the expected D_e range based on multiplying the dose rate of LBB-I by the U-series ages of the two stalagmites from the upper surfaces of both Layers 4a and 4b. (b) The same data sets in (a) displayed as histograms.

4.5. The relationship between D_e and *g*-value

One straightforward way to deal with anomalous fading is to correct for this phenomenon based on laboratory fading test or *g*-values (e.g., Huntley & Hancock, 2001; Kars et al., 2008). However, the fading correction procedures are model dependent, and may produce unreliable results. Huntley & Hancock (2001) pointed out that their fading correction procedure may result in overcorrection for a high fading rate (e.g., above ∼6 %/decade) and it should only be applied to samples with natural doses lying in the linear region of the corresponding dose response curves.

Therefore, the fading correction procedure of Huntley & Lamothe (2001) should not be applied to the $pIRIR_{290}$ results for our samples because high anomalous fading rates were observed. Although the correction method proposed by Kars et al. (2008) seems not to suffer from this problem, the large uncertainties in the *g*-values measured for our samples, due to the low signal intensity, result in significantly large or infinite uncertainties in the fading-corrected ages. An alternative method to deal with anomalous fading is to isolate a non-fading signal for dating, based on either pIRIR or MET-pIRIR procedures (e.g., Thomsen et al., 2008; Li & Li, 2011). We have demonstrated that a simple $pIRIR_{(50,290)}$ or $pIRIR_{(100,290)}$ procedure cannot isolate a non-fading signal for our samples, and it is impractical to apply a MET-pIRIR procedure or a $pIRIR_{(200,290)}$ procedure to overcome this problem due to the low sensitivity of the samples studied (Fig. 2). Based on the results from LBB-I, we note that the highest D_e values, for both of the $pIRIR_{(50,290)}$ and $pIRIR_{(100,290)}$ signals, are consistent with that expected from U-series dating (Fig. 4 and Fig. 6a). This indicates that the aliquots or grains associated with the highest D_e values may have negligible fading. To test this, the same aliquots used for $pIRIR_{(100,290)}$ D_e estimation were subsequently measured for anomalous fading test based on the $pIRIR_{(100,290)}$ procedure. Fig. 7 shows the histograms of the *g*-values obtained from the 100 °C IRSL and $pIRIR_{290}$ signals for individual aliquots measured for each of the samples. It shows that systematically higher anomalous fading rates, ranging from ∼5 %/decade to 22 %/decade, were obtained for the 100 °C IRSL signal. The *g*-values obtained from the $pIRIR_{290}$ signal are, however, dominated in the range of ∼ 0–12 %/decade.

The results shown in Fig. 7 suggest that, although the 100 °C IR stimulation is able to reduce the anomalous fading rate by more than the IR stimulation at 50 °C, a wide range of *g*-values was still observed for the $pIRIR_{290}$ signal from different aliquots. The results indicate that different aliquots may underestimate the true D_e or age in different extents. It is, therefore, expected that there should be a negative correlation between the D_e values and corresponding *g*-values for different aliquots from the same sample; that is, those aliquots having lower *g*-values should have higher D_e values, and vice versa.

To test this, the *g*-values obtained from the 100 °C IRSL and $pIRIR_{290}$ signals were plotted against their corresponding D_e values for individual aliquots in Fig. 8a and Fig. 8b for each of the samples, respectively. A clear negative correlation between the *g*-values and D_e was observed for all the samples (note the log scale on the y-axis for the D_e values; see discussions below), confirming that it is the variable fading rates among different aliquots that results in the large variation and different extents of underestimation in the D_e values.

The negative relationship between D_e value and fading rate for individual grains has been reported in previous studies (e.g., Lamothe & Auclair, 1999; Lamothe et al., 2012). Based on this observation, Lamothe & Auclair (1999) proposed an isochron method (so-called *fadia*) to deal with samples that have a large variation in fading rates. In their study, the authors plotted the additive-dose signal intensities measured immediately after irradiation against those measured after set periods of time for a series of grains, and obtained a linear relationship between them. The data sets were then

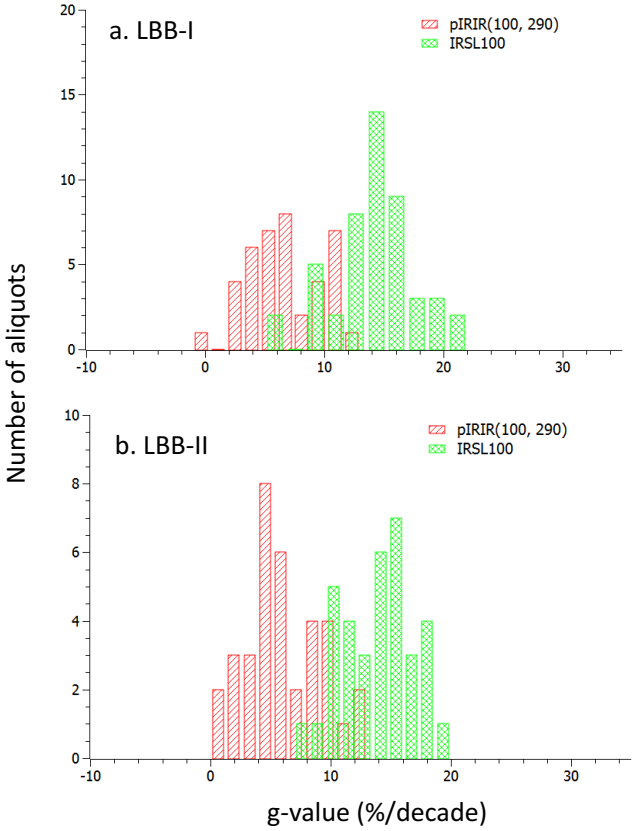

Figure 7. Histograms showing the g-values obtained from the 100 °C IRSL and $pIRIR_{290}$ signals for individual aliquots measured for each of the samples.

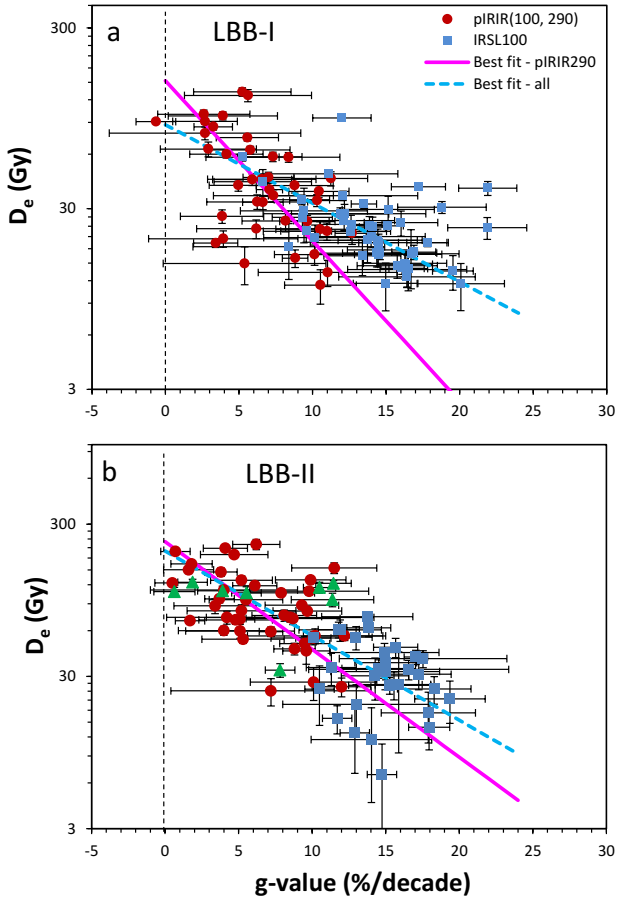

Figure 8. The D_e values obtained from the $IRSL_{100}$ and $pIRIR_{(100,290)}$ signals plotted against their corresponding g-values for individual aliquots for each of the samples, respectively. The results obtained from the $pIRIR_{(50,290)}$ signals are also shown for samples LBB-II (green triangles in b). The pink lines in the figures show the best fitting lines for the $pIRIR_{(100,290)}$ data only. The dashed blue lines show the best fitting lines for both the $IRSL_{100}$ and $pIRIR_{(100,290)}$ signals.

extrapolated to a 1 : 1 line, which represents zero fading, to correct for their additive-dose growth curves. Using a similar concept, Lamothe et al. (2012) extrapolated the trend between D_e values and g-values to a fading rate of zero, which yielded a result consistent with the expected age of their sample. For the LBB samples, we found that the relationship between the logarithm of D_e and g-value appears to broadly follow a linear relationship (Fig. 8), suggesting that an isochron method could be used to estimate D_e values at zero g-value by extrapolation onto the y-axis. In order to confirm that such a linear relationship is physically plausible, we calculated theoretical isochrons using the model described in Kars et al. (2008); Li & Li (2008). In this model, the natural and laboratory growth curves can be established for different anomalous fading rates, which allow one to calculate the apparent D_e values at different fading rates.

Fig. 9a shows the isochron lines for a series of natural doses (from 100 Gy to 1,000 Gy). It can be seen that the logarithm of the apparent D_e values have a good linear relationship with the g-values up to 12 %/decade, especially for the natural doses between 100 Gy and 600 Gy. For the natural doses larger than 600 Gy, there is a breakup of the linearity at low g-value range (e.g., 0–3 %/decade). In order to test whether one can use an isochron method to estimate the natural dose, the data series in Fig. 9a in the g-value range of 0–12 %/decade and 0–21 %/decade were linearly fitted, respectively. The isochron D_e were estimated from the intercepts of best fitting lines on the y-axis, and these are compared with the natural doses in Fig. 9b. It is shown that, for natural doses smaller than 300 Gy, fitting the data in the g-value range of 0–12 %/decade yields better results that are consistent with the natural doses within 2 %. For the natural doses from 300 Gy to 700 Gy, however, better results are produced by fitting the data from the g-value range of 0–21 %/decade (i.e., the isochron D_e are consistent with the natural doses within 3 %). For the natural dose larger than 700 Gy, the isochron D_e start to yield considerable underestimation by more than 5 %, which is expected due to the breakup of the linearity at low g-value range (Fig. 9a).

Based on this observation, we have applied linear regression onto the experimental data in Fig. 8 to estimate the D_e values corresponding to zero g-value (i.e., non-fading). We

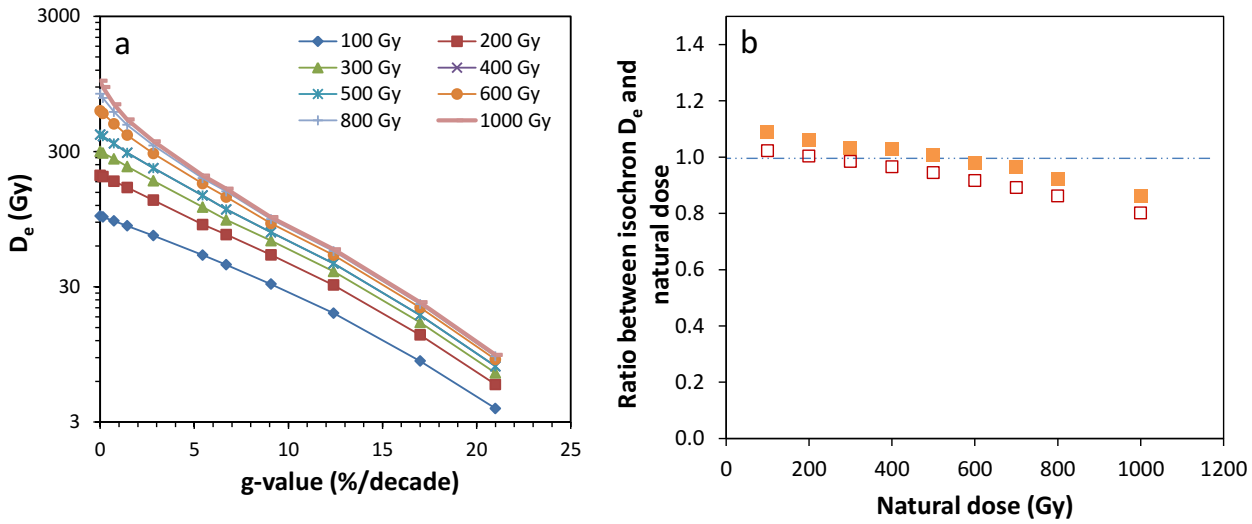

Figure 9. (a) Theoretical isochrons (D_e as a function of g-values) for different natural doses from 100 Gy to 1,000 Gy, obtained using the model described in Kars et al. (2008) and Li & Li (2008). The parameters used to produce the results are as follows: frequency factor $s = 3 \times 10^{15}\, s^{-1}$, characteristic saturation dose $D_0 = 400$ Gy, environmental dose rate= 5 Gy/ka and laboratory dose rate = 0.08 Gy/s. The D_0 and dose rates are similar to those for our samples. (b) The ratio between the isochron De and natural doses. The isochron D_e were estimated from the intercepts of linear regression using the data series of (a). The filled squares were obtained by fitting the data in the g-value range of 0–21 %/decade, while the open squares were obtained by fitting only the data in the range of 0–12 %/decade.

have used the Model 3 linear regression algorithm implemented in Isoplot 3.75 (Ludwig, 2012), which combines the errors associated with both the x- and y-values. For the sample LBB-I, this yields a D_e estimate of 153^{+39}_{-31} Gy by fitting the data set of $pIRIR_{(100,290)}$ only (pink line). This corresponds to an age of $25.1^{+6.9}_{-5.5}$ ka after correction for the residual dose (see below). If both the data sets of $pIRIR_{(100,290)}$ and $IRSL_{100}$ signals are fitted (dashed blue line), a D_e estimate of $87.4^{+12}_{-10.3}$ Gy is obtained, which corresponds to an age of $13.6^{+2.2}_{-1.9}$ ka after correction for the residual dose. Although both ages are consistent with the U- series ages of ~13.7–26 ka obtained from the stalagmites bracketing the sample, the age ($13.6^{+2.2}_{-1.9}$ ka) obtained by fitting both data sets is younger than the ^{14}C age for the *T. perfecta* shell taken above the sample. Hence, we consider the age obtained based on the data of $pIRIR_{(100,290)}$ as being more reliable. Two suppositions can explain the underestimation of the age obtained by including the data of $IRSL_{100}$ for fitting: (1) most of the g-values of the $IRSL_{100}$ signal are larger than 10 %/decade, which lies on the sublinear part of the isochron lines (Fig. 9a); (2) the D_e values of the $IRSL_{100}$ signals are very low (most of them are less than 30 Gy), so it is possible that the effect of thermal transfer or residual dose may have a significant contribution to the apparent D_e estimates. As a result, the D_e values of the $IRSL_{100}$ signal from some aliquots with high g-values may be higher than those expected according to their fading rate. For this reason, we consider that the age produced by fitting both the data sets of $pIRIR_{(100,290)}$ and $IRSL_{100}$ signals should be viewed as a minimum age estimate.

We adopted the same method to determine the D_e for the other sample LBB-II (see Fig. 8b), and the isochron of $pIRIR_{(100,290)}$ signal (pink lines in Fig. 8) yields a D_e value of 230^{+48}_{-40} Gy. The isochron obtained by fitting both $IRSL_{100}$ and $pIRIR_{(100,290)}$ signals give D_e value of 200^{+26}_{-23} Gy for the same sample. The luminescence ages from Leang Bulu Bettue, together with 1σ uncertainties obtained for all our samples, are summarised in Table 1. Our results suggest that the sampled sediments in Layers 4a and 5 were deposited $25.1^{+6.9}_{-5.5}$ ka and $44.1^{+9.8}_{-8.2}$ ka ago, respectively. These ages are in correct stratigraphic order, and the age estimate for LBB-I is consistent with the high-precision U-series ages obtained for the stalagmites bracketing Layer 4a and the ^{14}C age for the *T. perfecta* shell taken from the upper part of this layer (Fig. 1). Moreover, as noted above, LA U-series analysis of a bovid molar from the base of Layer 5 provided an in-sequence minimum age of 51.8 ± 0.6 ka, which is stratigraphically consistent with our depositional age of $44.5^{+9.8}_{-8.2}$ ka (1σ) for the sample LBB-II.

This coherent sequence of ages for the upper part of the stratigraphic sequence, and the consistency with the independent age control at this site, further supports the reliability of the isochron method proposed in this study and our contention that the feldspar grains were bleached to a low level (corresponding to a residual dose of ~10 Gy, see the next section) prior to deposition.

4.6. Residual signal and dose recovery test for the $pIRIR_{(100,290)}$ procedure

It has been shown previously that the elevated temperature pIRIR traps are not fully bleached even after prolonged sunlight exposure, and this can result in significant residual

doses at the time of sediment deposition (e.g., Thomsen et al., 2008; Li & Li, 2011; Li et al., 2013). To estimate the extent of any residual dose, we exposed 4 natural aliquots of each sample to a solar simulator for ∼4 h and the remnant doses were measured using the $pIRIR_{(100,290)}$ procedure in Table 2. The residual doses obtained are 11.5 ± 1.1 Gy and 12.6 ± 1.8 Gy for LBB-I and -II, respectively. These values were then subtracted from the D_e estimate to determine final ages for our samples.

The performance of the $pIRIR_{(100,290)}$ procedure was tested using a dose recovery test (Galbraith et al., 1999). Similar to the residual dose measurement, 4 natural aliquots from LBB-II were bleached in a solar simulator for 4 h and then given a β-dose of 80 Gy. These aliquots were then measured using the $pIRIR_{(100,290)}$ procedure. A recovered dose of 93 ± 5 Gy was obtained, corresponding to a recovery ratio of 1.00 ± 0.07, after correction for residual dose, indicating that the experimental conditions used here are able to recover the given dose accurately.

5. Discussion

Our study on the sanidines from the Leang Bulu Bettue sediments demonstrates the presence of high anomalous fading rates in the IRSL signals from sanidines, which resulted in a severe age underestimation for these samples. Our results further support the results of previous studies that high temperature and disordered volcanic feldspars, such as sanidines, generally have higher fading rates than orthoclases and microclines (Aitken, 1985; Visocekas et al., 1994, 1998; Huntley & Lian, 2006). We also show that the high anomalous fading rates cannot be overcome using a $pIRIR_{290}$ procedure for most of the aliquots measured, although the $pIRIR_{290}$ signals exhibit a much less pronounced fading rate compared to the prior IRSL signals measured at lower temperature (50 °C or 100 °C). Furthermore, it appears that different grains or aliquots from our samples have considerably different fading rates in their IRSL and pIRIR signals, which results in a large among-aliquot variation in their corresponding D_e values (Fig. 4, 5, 6, 7). Such a wide spread in D_e values could easily lead to a false impression that these samples have been insufficiently bleached or contain a mixture of grains with different ages, which may result in erroneous age estimation if a minimum age model was adopted (Fig. 4). We suggest, therefore, that it is important to conduct a detailed anomalous fading test when using pIRIR procedure, especially for dating volcanic feldspars. We proposed a method to deal with the problem associated with variable fading rate encountered for dating the sanidine feldspars from the archaeological site Leang Bulu Bettue, based on the relationship between the D_e values and g-values (Fig. 8). Our method is, in principle, similar to the method of Lamothe & Auclair (1999) and Lamothe et al. (2012) proposed to deal with samples that have a large variation in fading rates. In their studies, the authors extrapolated the linear relationship between D_e and g-value. In our study, in contrast, we extrapolated of the relationship between the $log(D_e)$ values and g-values, based on numerical simulation using the physical model of Huntley & Lian (2006). Our results suggest that reliable D_e estimate can be obtained by extrapolation of the relationship between the $log(D_e)$ values and g-values to zero fading (i.e., g-value = 0 %/decade). The pIRIR ages obtained for our samples are consistent with the empirical results from other independent dating techniques from the same site, confirming the validity of the isochron method.

6. Conclusions

The volcanic sanidines from two Late Pleistocene archaeological layers at Leang Bulu Bettue on the Indonesian island of Sulawesi have a highly variable anomalous fading rate in their IRSL signal for different grains and aliquots. The dim IRSL signal intensity prevents the application of a MET-pIRIR procedure, and a low temperature IR stimulation (at 50 °C or 100 °C) used in a $pIRIR_{290}$ procedure cannot completely remove the anomalous fading for the subsequent $pIRIR_{290}$ signals. Reliable D_e estimation can be achieved by extrapolation of the relationship between D_e and g-values for the same sample, which provides a useful way to date the sediments containing volcanic feldspars of similar luminescence characteristics.

Acknowledgments

The dating work was supported by an Australian Research Council Future Fellowship to B.L. (FT140100384), an Australian Research Council Australian Laureate Fellowship to R.G.R. (FL130100116), and a postgraduate scholarship from the China Scholarship Council and the University of Wollongong to Y.G. (201206010053). The Leang Bulu Bettue excavations were funded by an Australian Research Council (ARC) DECRA fellowship (DE130101560) to A.B., with additional support provided by the Wenner Gren Foundation (Post-Ph.D. grant), University of Wollongong, and Griffith University. The Indonesian fieldwork was authorised by RISTEK and the Pusat Penelitian Arkeologi Nasional (ARKENAS). For facilitating this research, we thank ARKENAS director I.M. Geria, and the former directors of Makassars Balai Pelestarian Cagar Budaya and Balai Arkeologi, M. Said and G.M. Sudarmika, respectively. We also acknowledge the support of Y. Jafari and T. Lachlan in the Luminescence Dating Laboratory at the University of Wollongong. Fieldworkers included: B. Burhan, A.M. Saiful, L. Siagian, Suryatman, R. Sardi, A. Jusdi, Abdullah, A. P. Mubarak, Hasliana, Hasrianti, D. Susanti, R. Salempang, H. Arsyad, Muhtar, Sungkar, R. Ali, L. Lantik, Asri, H. Lahab, O. Amrullah, Idrus, M. Husain, Busran, A. Agus and D.P. McGahan.

References

Aitken, Martin J. *Thermoluminescence dating*. Studies in archaeological science. Academic Press, 1985.

Aitken, Martin J. *An Introduction to Optical Dating*. Oxford University Press, 1998.

Aubert, M, Brumm, A, Ramli, M, Sutikna, T, Saptomo, E W, Hakim, B, Morwood, M J, van den Bergh, G D, Kinsley, L, and Dosseto, A. *Pleistocene cave art from Sulawesi, Indonesia*. Nature, 514(7521): 223–227, 2014.

Auclair, Marie, Lamothe, Michel, and Huot, S. *Measurement of anomalous fading for feldpsar IRSL using SAR*. Radiation Measurements, 37(4-5): 487–492, 2003.

Berger, G W and Huntley, D J. *Tests for optically stimulated luminescence from tephar glass*. Quaternary Science Reviews, 13 (5-7): 509–511, 1994.

Bøtter-Jensen, L and Mejdahl, V. *Assessment of beta dose-rate using a GM multicounter system* . Nuclear Tracks and Radiation Measurements, 14: 187–191, 1988.

Bøtter-Jensen, L, Andersen, C E, Duller, Geoff A T, and Murray, Andrew S. *Developments in radiation, stimulation and oberservation facilities in luminescence measurements*. Radiation Measurements, 37: 535–541, 2003.

Bulbeck, D, Sumantri, I, and Hiscock, P. *Leang Sakapao 1, a second dated Pleistocene site from South Sulawesi, Indonesia*. In Keates, Susan G and Pasveer, Juliette M (eds.), *Quaternary Research in Indonesia*, pp. 111–128. 2004.

Fattahi, Morteza and Stokes, Stephen. *Dating volcanic and related sediments by luminescence methods: a review*. Earth-Science Reviews, 62: 229–264, 2003.

Galbraith, Rex F and Roberts, Richard G. *Statistical aspects of equivalent dose and error calculation and display in OSL dating: An overview and some recommendations*. Quaternary Geochronology, 11: 1–27, 2012.

Galbraith, Rex F, Roberts, Richard G, Laslett, G M, Yoshida, H, and Olley, J M. *Optical dating of single and multiple grains of Quartz from Jinmium Rock Shelter, Northern Australia: Part I, Experimental design and statistical models*. Archaeometry, 41 (2): 339–364, 1999.

Glover, I C. *Leang Burung 2: an Upper Palaeolithic rock shelter in south Sulawesi, Indonesia*. Modern Quaternary Reasearch in Southeast Asia, pp. 1–38, 1981.

Huntley, D J and Hancock, R G V. *The Rb contents of the K-feldspar grains being measured in optical dating*. Ancient TL, 19(2): 43–46, 2001.

Huntley, D J and Lamothe, Michel. *Ubiquity of anomalous fading in K-feldspars and the measurement and correction for it in optical dating*. Canadian Journal of Earth Sciences, 38: 1093–1106, 2001.

Huntley, D J and Lian, Olav B. *Some observations on tunnelling of trapped electrons in feldspars and their implications for optical dating*. Quaternary Science Reviews, 25(19-20): 2503–2512, 2006.

Jacobs, Zenobia and Roberts, Richard G. *An improved single grain OSL chronology for the sedimentary deposits from Diepkloof Rockshelter, Western Cape, South Africa*. Journal of Archaeological Science, 63(C): 175–192, 2015.

Kars, R H, Wallinga, J, and Cohen, K M. *A new approach towards anomalous fading correction for feldspar IRSL dating — tests on samples in field saturation*. Radiation Measurements, 43: 786–790, 2008.

Lamothe, Michel and Auclair, Marie. *A solution to anomalous fading and age shortfalls in optical dating of feldspar minerals*. Earth and Planetary Science Letters, 171: 319–323, 1999.

Lamothe, Michel, Barré, Magali, Huot, Sébastien, and Ouimet, Stéphanie. *Natural luminescence and anomalous fading in K-feldspar*. Radiation Measurements VL -, 47(9): 682–687, 2012.

Li, Bo and Li, Sheng-Hua. *Investigations of the dose-dependent anomalous fading rate of feldspar from sediments*. Journal of Physics D: Applied Physics, 41(22): 225502, 2008.

Li, Bo and Li, Sheng-Hua. *Luminescence dating of K-feldspar from sediments: A protocol without anomalous fading correction*. Quaternary Geochronology, 6(5): 468–479, 2011.

Li, Bo and Li, Sheng-Hua. *A reply to the comments by Thomsen et al. on "Luminescence dating of K-feldspar from sediments: A protocol without anomalous fading correction"*. Quaternary Geochronology, 8(C): 49–51, 2012.

Li, Bo, Roberts, Richard G, and Jacobs, Zenobia. *On the dose dependency of the bleachable and non-bleachable components of IRSL from K-feldspar: Improved procedures for luminescence dating of Quaternary sediments*. Quaternary Geochronology, 17: 1–13, 2013.

Li, Bo, Jacobs, Zenobia, Roberts, Richard, and Li, Sheng-Hua. *Review and assessment of the potential of post-IR IRSL dating methods to circumvent the problem of anomalous fading in feldspar luminescence*. Geochronometria, 41(3): 178–201, 2014.

Ludwig, Kenneth R. *User's Manual for Isoplot 3.75*. Berkeley Geochronology Center, 3.75 edition, 2012.

McDonald, R C. *Limestone morphology in South Sulawesi, Indonesia*. Zeitschrift für Geomorhologie, Supplementbände, 26: 79–91, 1976.

Morwood, M J, Soejono, R P, Roberts, R G, Sutikna, T, Turney, C S M, Westaway, K E, Rink, W J, Zhao, J x, van den Bergh, G D, Due, Rokus Awe, Hobbs, D R, Moore, M W, Bird, M I, and Fifield, L K. *Archaeology and age of a new hominin from Flores in eastern Indonesia*. Nature, 431(7012): 1087–1091, 2004.

Prescott, J. R. and Hutton, J T. *Cosmic ray contributions to dose rates for luminescence and ESR dating: Large depths and long-term time variations*. Radiation Measurements, 23(2-3): 497–500, 1994.

Roberts, R G, Westaway, K E, Zhao, J x, Turney, C S M, Bird, M I, Rink, W J, and Fifield, L K. *Geochronology of cave deposits at Liang Bua and of adjacent river terraces in the Wae Racang valley, western Flores, Indonesia: a synthesis of age estimates for the type locality of Homo floresiensis*. Journal of Human Evolution, 57(5): 484–502, 2009.

Smedley, R K, Duller, G A T, Pearce, N J G, and Roberts, H M. *Determining the K-content of single-grains of feldspar for luminescence dating*. Radiation Measurements VL -, 47(9): 790–796, 2012.

Sutikna, Thomas, Tocheri, Matthew W, Morwood, Michael J, Saptomo, E Wahyu, Jatmiko, Awe, Rokus Due, Wasisto, Sri, Westaway, Kira E, Aubert, Maxime, Li, Bo, Zhao, Jian-xin, Storey, Michael, Alloway, Brent V, Morley, Mike W, Meijer, Hanneke J M, van den Bergh, Gerrit D, Grün, Rainer, Dosseto, Anthony, Brumm, Adam, Jungers, William L, and Roberts, Richard G. *Revised stratigraphy and chronology for Homo floresiensis at Liang Bua in Indonesia*. Nature, 532(7599): 366–369, 2016.

Thiel, Christine, Buylaert, J P, Murray, Andrew, Terhorst, Birgit, Hofer, Ingo, Tsukamoto, Sumiko, and Frechen, Manfred. *Luminescence dating of the Stratzing loess profile (Austria) - Testing the potential of an elevated temperature post-IR IRSL protocol*. Quaternary International, 234(1-2): 23–31, 2011.

Thomsen, K J, Murray, Andrew S, Jain, M, and Bøtter-Jensen, L. *Laboratory fading rates of various luminescence signals from feldspar-rich sediment extracts*. Radiation Measurements, 43(9-10): 1474–1486, 2008.

Tsukamoto, S and Duller, G A T. *Anomalous fading of various luminescence signals from terrestrial basaltic samples as Martian analogues*. Radiation Measurements, 43(2-6): 721–725, 2008.

Tsukamoto, S, Duller, G A T, Wintle, A G, and Muhs, D. *Assessing the potential for luminescence dating of basalts*. Quaternary Geochronology, 6(1): 61–70, 2011.

Tsukamoto, Sumiko, Kataoka, Kyoko, Oguchi, Takashi, Murray, Andrew S, and Komatsu, Goro. *Luminescence dating of scoria fall and lahar deposits from Somma-Vesuvius, Italy*. Quaternary Geochronology, 20(C): 39–50, 2014.

van den Bergh, Gerrit D, Li, Bo, Brumm, Adam, Grün, Rainer, Yurnaldi, Dida, Moore, Mark W, Kurniawan, Iwan, Setiawan, Ruly, Aziz, Fachroel, Roberts, Richard G, Suyono, Storey, Michael, Setiabudi, Erick, and Morwood, Michael J. *Earliest hominin occupation of Sulawesi, Indonesia*. Nature, pp. 1–19, 2016.

Visocekas, R, Spooner, N A, Zink, A, and Blanc, P. *Tunnel afterglow, fading and infrared emission in thermoluminescence of feldspars*. Radiation Measurements, 23(2-3): 377–385, 1994.

Visocekas, R, Tale, V, Zink, A, and Tale, I. *Trap Spectroscopy and Tunnelling Luminescence in Feldspars*. Radiation Measurements, 29(3-4): 427–434, 1998.

Westaway, Kira E and Roberts, Richard G. *A dual-aliquot regenerative-dose protocol (DAP) for thermoluminescence (TL) dating of quartz sediments using the light-sensitive and isothermally stimulated red emissions*. Quaternary Science Reviews, 25 (19-20): 2513–2528, 2006.

Wintle, Ann G. *Anomalous Fading of Thermoluminescence in Mineral Samples*. Nature, 245: 143–144, 1973.

Reviewer

Jim Feathers

Reviewer's comment

Michel Lamothe and colleagues introduced the idea of isochron dating to address the problem of anomalous fading in 1999 and then followed up in 2012. The paper here by Bo Li and colleagues develops this idea further and shows the strength of a too-long neglected method. The application here is to volcanic feldspars, but it would be worth pursuing other applications.

Ancient TL

Bayesian statistics in luminescence dating: The 'baSAR'-model and its implementation in the R package 'Luminescence'

Norbert Mercier,[1*] Sebastian Kreutzer,[1] Claire Christophe,[1,2]
Guillaume Guérin,[1] Pierre Guibert,[1] Christelle Lahaye,[1] Philippe Lanos,[1]
Anne Philippe,[2,3] and Chantal Tribolo[1]

[1]IRAMAT-CRP2A, UMR 5060 CNRS- Université Bordeaux Montaigne, Pessac, France
[2]Laboratoire de mathématiques Jean Leray, UMR 6629 CNRS, Université de Nantes, Nantes, France
[3]ANJA INRIA, Campus universitaire de Beaulieu, Rennes, France

[*]Corresponding Author: norbert.mercier@u-bordeaux-montaigne.fr
Received: July 6, 2016; in final form: September 13, 2016

Abstract

A function named `analyse_baSAR()` was written using the statistical programming language R and its code is now available within the R package 'Luminescence'. The function allows the application of the Bayesian hierarchical model 'baSAR' proposed by Combès et al. (2015) and comes with additional features to analyse luminescence data in a straight forward way. Example scripts are provided showing the possible numerical and graphical outputs.

Keywords: R, Bayesian statistics, Luminescence dating, Hierarchical model, SAR

1. Introduction

Analysing the distribution of obtained equivalent doses (D_e), to estimate a D_e and its standard error ($se(D_e)$) best representing the data after applying the single aliquot regenerative-dose (SAR) protocol (Murray & Wintle, 2000), either on single or multi-grain aliquots, is a vital step of the luminescence dating process. A summary of commonly applied statistical approaches in the luminescence dating community with their individual limitations is given by Galbraith & Roberts (2012).

Additionally, several differing suggestions have been made in the past to use Bayesian statistics (Bayes 1773; cf., e.g., Buck et al. 1996; Gelman et al. 2013 for a general introduction) for particular problems while analysing luminescence data and best estimate the D_e (or age) of particular interest, with regard to the underlying geochronological problem, e.g., Rhodes et al. (2003); Huntriss (2008); Peng & Dong (2014); Cunningham et al. (2015); Zink (2015).

It is out of the scope of this paper to compare or repeat details of the so far presented approaches, but we will rather focus on the work presented by Combès et al. (2015). They proposed an alternative to the central age (equivalent dose) model (usually termed: CAM) by Galbraith et al. (1999) using Bayesian statistics. The model by Combès et al. (2015) comprises a hierarchical structure in the sense that their central equivalent dose (in analogy to Combès et al. 2015 hereafter $\mathcal{D}$) is not directly deduced from the individual D_e values and their associated standard errors, as it is the case in the CAM model, but (a) from the normalised luminescence signal ratios (L_x/T_x) of each aliquot or grain leading to these individual values, and (b) from the type of function representing the distribution of the D_e values; the model is termed 'baSAR' henceforth. Combès et al. (2015) have chosen a Cauchy distribution to describe the dispersion around $\mathcal{D}$, as it *"[...] has the advantage of being close to a Gaussian near the mode and of having heavy tails [..]"* (Combès et al., 2015, p. 67) and with this allowing more spread in the data than a log-normal (or normal) distribution and ensures a greater statistical robustness. The $\mathcal{D}$ value defines the mode of the distribution and another parameter, $\sigma_{\mathcal{D}}$, measures the dispersion of the individual doses around $\mathcal{D}$.

Nevertheless, though the proposed baSAR-model, originally implemented using the language BUGS, has been tested on a series of samples (Guérin et al., 2015) and proved some advantages over the CAM model, its use by the luminescence community was so far limited due to a lack of any available user-friendly and flexible code. Here, we present the function `analyse_baSAR()` available in the **R** (R Development Core Team, 2016) package 'Luminescence' (version

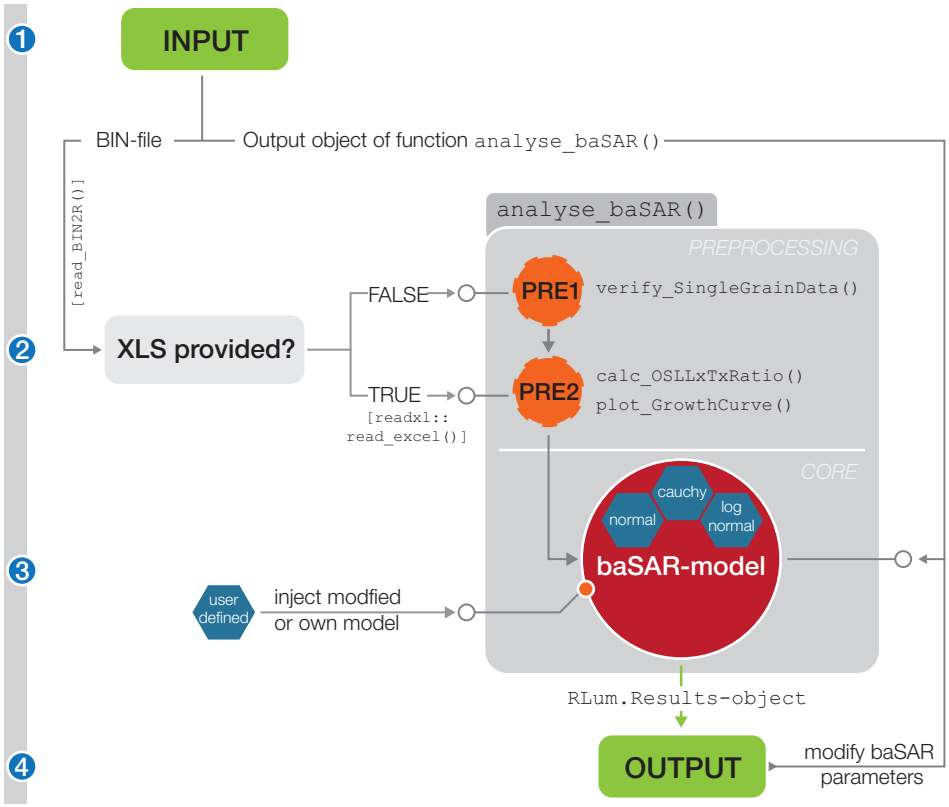

Figure 1. Possible input and output scenarios implemented in the function `analyse_baSAR()`. Alternatively of a BIN/BINX-file that is automatically imported using the function `read_BIN2R()` the user can provide the `RisoeBINfileData-object` produced by this function. This avoids potentially time consuming repeated imports of the measurement data in scenarios where the user wants to play with the function arguments. Furthermore, instead of an XLS-file a `data.frame` of similar structure is accepted as input. For further details see main text.

>= 0.6.4, Kreutzer et al. 2012 and Kreutzer et al. 2016, see also Dietze et al. 2013 and Fuchs et al. 2015 for guides and introductions). The function is not a copy & paste implementation of the proposed model, but a consequent enhancement of the published model, combined with the data processing features by the **R** package 'Luminescence'.

With our contribution we provide technical details on the implementation of the `analyse_baSAR()` function and running examples that can directly be applied by the user on own data. The code is provided under General Public Licence (GPL-3) conditions.

Below **R** code snippets are given as separated listings and typed in `monospace` letters. If not stated otherwise mentioned **R** `functions()` are part of the **R** package 'Luminescence'. Function calls from other **R** packages are indicated by `::`, e.g., `readxl::read_excel()`.

2. Enhancement and implementation

2.1. Enhancing the 'baSAR'-model

The function `analyse_baSAR()` includes all functionalities developed in the baSAR-model and enhances it as suggested by Combès et al. (2015) with regard to additional fitting functions and supported probability distributions.

- While the mathematical function fitting the dose response curve to pairs of L_x/T_x ratios and dose values in the original baSAR-model was limited to (I) a single saturating exponential + linear term

$$f_{\Theta=(a,b,c,d)} : x \rightarrow d + (c \cdot x) + \left(a(1 - exp(\frac{-x}{b}))\right) \quad (1)$$

with its curve parameters a, b, c and d, the function `analyse_baSAR()` includes a further two mathematical functions to describe the dose-response curve:

(II) a linear function

$$f_{\Theta=(c,d)} : x \rightarrow d + (c \cdot x) \quad (2)$$

(III) a single exponential function

$$f_{\Theta=(a,b,d)} : x \rightarrow d + \left(a(1 - exp(\frac{-x}{b}))\right) \quad (3)$$

- furthermore, the user now has the option to include the recycling point(s) in the calculation, and to force the dose response curve through the origin,
- and finally, in order to improve the application of the Bayesian statistics to the luminescence data, the function supports, in addition of the Cauchy distribution, a

Gaussian (normal) distribution and a log-normal distribution which can be chosen to characterise the dispersion of the individual D_e values.

2.2. Implementing `analyse_baSAR()`

From a technical point of view, the `analyse_baSAR()` function uses the software *JAGS* (Just Another Gibbs Sampler; Plummer 2003) available via the **R** interface 'rjags' (Plummer et al., 2016), which is a tool for the analysis of Bayesian hierarchical models using a Markov chain Monte Carlo (MCMC) simulation. The software *JAGS* needs to be installed separately and additionally to the **R** environment. Internally the function is separated in two parts: (I) a Bayesian core, i.e., the implementation of the baSAR-model and (II) a data preprocessing part (cf. Fig. 1).

This separation allows rather complex input/output scenarios and flexible data handling. Fig. 1 drafts a generalised view of possible workflow scenarios. Running examples with its function arguments are given in Sec. 3 and in the supplement. The subsequent numbering was chosen in accordance with the one (numbers in the blue circle) in Fig. 1.

1. The function distinguishes between two different input scenarios: (A) raw measurement data, e.g., a BIN/BINX-file, which is the standard output of Risø TL/OSL readers and (B) an output object produced by the function itself. If the latter one is provided the function automatically starts with the Bayesian calculation and the data preprocessing is skipped. If measurement data are provided (BIN-file), the measurement data are imported into the **R** session. For BIN/BINX-files this is done using the function `read_BIN2R()`.

2. Along with the measurement data (A) an *MS Excel*^{TM} (file ending either *.XLS or *.XLSX)[1] can be provided to limit the measurement data to the aliquots specified in the table (see screenshot in Fig. 2), i.e. the data processing will be continued with a reduced, previously selected dataset. If no XLS-file is provided (B) the data will be piped to the function `verify_SingleGrainData()`[2] to remove dim aliquots (not curves!), as such aliquots would bias the output. Removing dim or zero light grains (aliquots) is a usual task while dealing with single grain data.

   Once the data had been selected with either the one (A) or other (B) approach, L_x/T_x ratios are calculated from the single curves using the function `calc_OSLLxTxRatio()`. The data would be now ready for the baSAR-model, but they will be first piped to the function `plot_GrowthCurve()` to calculate D_e and D_0 values and, if wanted, it allows a visual feedback of the data. Nevertheless, these values (D_e and D_0) are not taken into account for the subsequent modelling, but are returned and can be used for further data subsetting, e.g., sorting grains by D_0 values.

3. After the data preprocessing is finished the ordinary Bayesian modelling starts as described by Combès et al. (2015) internally using the package 'rjags' and the software *JAGS*. The result is a comprehensive object of type `RLum.Results` (see supplement for examples and more details).

4. The results of the modelling can be used for further data processing or directly piped for another run into the function `analyse_baSAR()` itself. As written above, in the latter case the entire data preprocessing is skipped and the function jumps into the baSAR-model core, remembering the previous set function arguments, but the user can modify parameters on request for the Bayesian calculation, e.g., number of MCMC runs.

	A	B	C
1	**BIN_FILE NAME**	**DISC**	**GRAIN**
2	BINfile 1	4	27
3			
4	BINfile 2	11	89
5	BINfile 3	6	51
6			
7	BINfile 3	13	6
8	BINfile 3	3	22

Figure 2. Screenshot of an example *MS Excel*^{TM} sheet that can be provided as input to limit the number of aliquots according to the disc and grain number. As shown in the figure empty rows are allowed to structure the table and they will be ignored during the import.

The injection of own and/or modified models is possible in every scenario (see below). The current implementation is limited to BIN/BINX-files only.

3. Working example

In this section a simplified example of the function input and output is given for the current implementation. The details given for specific function arguments are intentionally vague. They may change in the future due to a continuous development process and would here remain of limited use for the reader. An always up-to-date and detailed description of the function arguments can be found by typing `?analyse_baSAR` in the **R** terminal.

3.1. Constructing the function call

In the following function call, the user provides a list of BIN-files (argument `object`) that were measured on different readers or at different dates.

```
results <- analyse_baSAR(
    object <- list(
        "Bin1.bin",
        "Bin2.binx",
        "Bin3.bin"),
```

[1] The import is realised using the function `readxl::read_excel()` (Wickham et al., 2016)

[2] Type `?verify_SingleGrainData` in the **R** terminal for further information.

As usually irradiations are carried out as durations and not as doses, the dose rate and its standard error of the irradiation source (argument `source_doserate`) needs to be provided[3] for each BIN-file. The standard error of the source dose rate is considered to be systematic and is therefore only added at the end to the standard error of the $\mathcal{D}$.

```
    source_doserate = list(
          c(0.10, 0.001),
          c(0.13, 0.002),
          c(0.12, 0.001)),
```

As stated above, to increase the flexibility of the calculation, the user can pass a list of discs/grains, each pair defining an aliquot, to be included in the calculation. This is possible either in the form of a `data.frame` or in using an *MS Excel*^{TM} sheet. The user might also prefer to use the `verify_SingleGrainData()` function, included in the `analyse_baSAR()` function, which automatically provides a list of grains exhibiting luminescence signals significantly higher than a pre-selected threshold (see `?verify_SingleGrainData`). Regardless of this option, in this example an XLS-file (argument `XLS_file`) is passed to the function comprising a sheet (`sheet`) with a pair list of discs and grains. This selection is further limited to the aliquots 1 to 30 by `aliquot_range`. Please note that currently the argument `aliquot_range` works only if an XLS-file is provided or the output of the function itself `analyse_baSAR()` is provided as input.

```
    XLS_file = "~/Bayesian/Site/Sample.xls",
    sheet = "Disc-Grain-list",
    aliquot_range = c(1:30),
```

In the next step signal and background integration limits are set and additional uncertainty (`sig0`) is added to each resulting L_x/T_x value, the over-dispersion of the count distribution (`sigmab`) is set to 0 in this example.

```
    signal.integral = c(5:10),
    signal.integral.Tx = c(5:10),
    background.integral = c(40:60),
    background.integral.Tx = c(40:60),
    sigmab = 0,
    sig0 = 0.025,
```

Controlling the Bayesian modelling is an important option and several arguments are provided to control the process. Here, namely the chosen probability `distribution` (`'cauchy'`, `'normal'` or `'log_normal'`), the number of Markov chain Monte Carlo runs (`n.MCMC`; default 100,000) and the applied fitting function (`fit.method`) and its options (`fit.force_through_origin` and `fit.includingRecyclingPoints`). The fitting arguments chosen here are also used during the data processing.

Deeper control of the modelling process is granted via argument provided via the `method_control`. In the example the number of used MCMC is set.

```
    distribution = "normal",
    n.MCMC = 100000,
    fit.method = "EXP",
    fit.force_through_origin = TRUE,
    fit.includingRecyclingPoints = TRUE,
    method_control = list(
     n.chains = 3),
```

The last arguments to be set control various terminal (`verbose`) and plot output (`plot`, `output.plot`, `plot_reduced`) options.

```
    plot = TRUE,
    output.plot = TRUE,
    plot_reduced = TRUE,
    verbose = TRUE
  )
```

The complete function call (putting the single snippets together) becomes:

Listing 1. Example combined function call

```
results <- analyse_baSAR(
    object <- list(
          "Bin1.bin",
          "Bin2.binx",
          "Bin3.bin"),
    source_doserate = list(
          c(0.10, 0.001),
          c(0.13, 0.002),
          c(0.12, 0.001)),
    XLS_file = "~/Bayesian/Site/Sample.xls",
    sheet = "Disc-Grain-list",
    aliquot_range = c(1:30),
    signal.integral = c(5:10),
    signal.integral.Tx = c(5:10),
    background.integral = c(40:60),
    background.integral.Tx = c(40:60),
    sigmab = 0,
    sig0 = 0.025,
    distribution = "normal",
    n.MCMC = 100000,
    fit.method = "EXP",
    fit.force_through_origin = TRUE,
    fit.includingRecyclingPoints = TRUE,
    method_control = list(
     n.chains = 3),
    plot = TRUE,
    output.plot = TRUE,
    plot_reduced = TRUE,
    verbose = TRUE
)
```

The code line numbers are similar to the one of the code snippets before as there are extracted from the combined call. The example function call appears rather complex and the number of arguments might be confusing, but most of them are preset and can be modified on request.

3.2. Graphical and terminal output

The (reduced) graphical feedback of the function is shown in Fig. 3, 4 and 5 providing useful information regarding the convergence process (Fig. 3) of the Bayesian analysis (three Markov chains are created by the code): convergence is observed if the slope of the trend of the red, green and black lines is almost zero, i.e., the posterior distributions (here three chains) had converged, the individual doses (Fig. 4), the dose response curve and the conventional D_e with the $\mathcal{D}$ marked within (Fig. 5).

[3] `source_doserate` is a required argument; leaving this argument empty will stop the function from running.

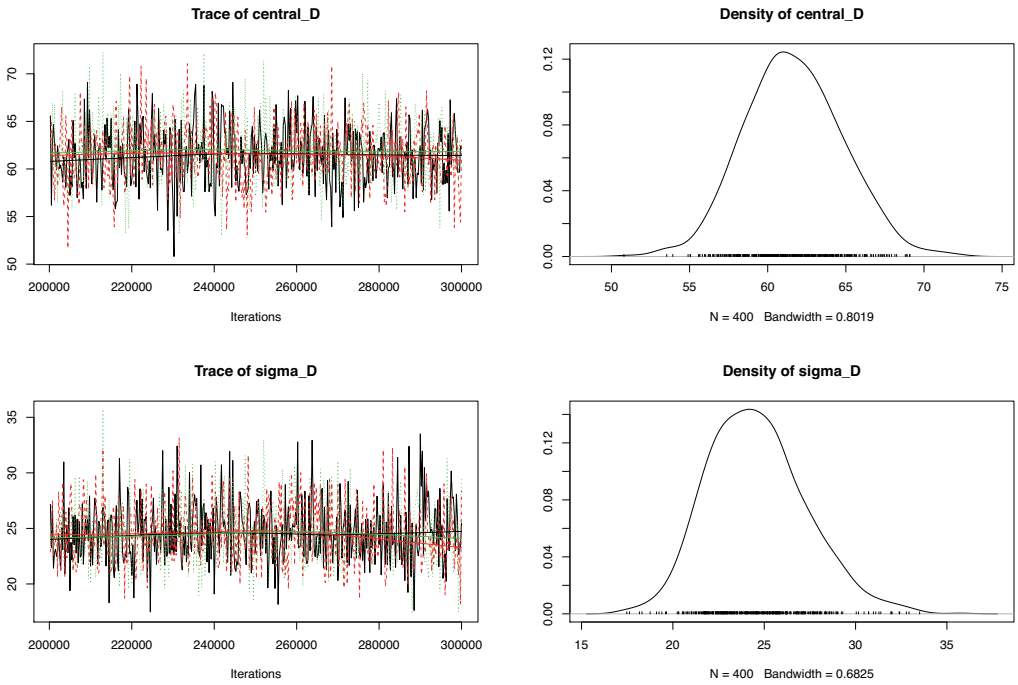

Figure 3. Exemplary plot output of the function `analyse_baSAR()`. The lefthand figures show three Markov chains, each one being a sample of the posterior distribution of $\mathcal{D}$ (top) and $\sigma_{\mathcal{D}}$ (bottom). The righthand figures are estimates of the posterior density functions for these two variables.

The corresponding **R** terminal output may look like the example given below.[4]

Listing 2. Exemplary **R** terminal output

```
[analyse_baSAR()] ------ RESULTS ------

-----------------------------------------------
Used distribution:                  normal
Number of aliquots used:            128/128
Considered fitting method:          EXP
Number MCMC iterations:             100000
-----------------------------------------------

                        mean   sd    HPD
>> Central dose:        61.24  2.82  [58.46;63.95]**
                                     [55.81;66.96]***
>> sigma_D:              23.9   2.39  [21.56;26.21]**
                                     [19.52;29.06]***
>> Final central De:    61.24  2.82      -     -
-----------------------------------------------

(systematic error contribution
to final De: 6.28741e-06 %)
** 68 % level | *** 95 % level
```

The first four lines return the applied parameters used by the baSAR-model. The following three lines report on the estimated $\mathcal{D}$ and $\sigma_{\mathcal{D}}$ and the final $\mathcal{D}$ including the systematic uncertainty provided via `source_doserate`. For $\mathcal{D}$ and $\sigma_{\mathcal{D}}$ the mean, the standard deviation, as well as the highest posterior densities (HPD) at their 68 % and 95 % confidence levels are provided. For an interpretation of the numerical output, the reader is referred to Combès et al. (2015).

The output of the function can now be piped again to the function but with modified parameters, e.g., the distribution is set to `'cauchy'` instead of `'normal'`. In this case the previously produced object `results` is now set as input (`object`) for the new function run.

Listing 3. Use previous output as input

```
results_new <- analyse_baSAR(
        object = results,
        distribution = 'cauchy')
```

Finally the obtained $\mathcal{D}$ is combined and plotted along with the D_e values in an abanico plot (Dietze et al., 2016) in Fig. 5.

3.3. Additional remarks

3.3.1 Selecting records

The function is written to deal with data measured using the SAR protocol only, i.e., the function is searching for OSL/IRSL curves following the pattern proposed by Murray & Wintle (2000). Any additional curve / measurement steps not belonging to this original protocol are not expected and need to be excluded from the input data set. Unfortunately it is not possible to account for all potential types of minor protocol modifications commonly applied in a particular laboratory. Therefore, if a BIN-file is provided, the function `analyse_baSAR()` respects the record selection made previously. This selection was made either with the software *Analyst* (Duller, 2015) or the base **R** function `subset()`. If the package 'Luminescence' is attached (the normal case if the `analyse_baSAR()` function is to be used) the function `subset` can be used in combination with objects produced by the function `read_BIN2R()`. In the example below only

[4] The output has been modified for a correct typesetting and the appearance in the **R** terminal may be different.

OSL curves are selected from the input data set.

Listing 4. Reduce BIN-file record to OSL curves

```
BIN_file_selection <- subset(
        x = BIN_file,
        subset = LTYPE == 'OSL')
```

The available list of selection criteria is defined by the corresponding file version of the BIN-file itself[5]. See the supplement for further examples of subsetting.

3.3.2 Additional parameters

Typing `?analyse_baSAR` in the **R** terminal reveals that the function `analyse_baSAR()` has an argument represented by three dots (`...`). This placeholder allows additional arguments to be passed to lower-level functions. These arguments are not listed as explicit function arguments and not necessary to run the function (usually because they have a meaningful default value). For example: an argument `skip` is passed to the function `read_excel::readxl()` and tells it to ignore the specified number of rows in the *Excel*^{TM} while importing the data. Please see the manual of the function for further information (`?analyse_baSAR`).

[5]It equals the list of columns in the software *Analyst*

3.3.3 User-defined model

In their paper, Combès et al. (2015) had chosen a Cauchy distribution, where the mode is defined by $\mathcal{D}$, and even though the function `analyse_baSAR()` allows normal and log-normal distributions as well, the user has the possibility to define their own model; in such cases, the model has to be passed to the function as a simple string of characters following the example below:

```
my_model <- "model {
  central_D ~ dunif(lower_centralD,upper_centralD)
  precision_D ~ dt(0, pow(0.16*central_D, -2), 1)T(0, )
  sigma_D <- 1/sqrt(precision_D)

 for (i in 1:Nb_aliquots) {
  #Priors
  a[i] ~  dnorm(6.5, 1/(9.2^2) ) T(0, )
  b[i] ~  dnorm(50, 1/(1000^2) )  T(0, )
  c[i] ~  dnorm(1.002, 1/(0.9^2) ) T(0, )
  g[i] ~  dnorm(0.5, 1/(2.5^2) ) I(-a[i], )
  sigma_f[i]  ~  dexp (20)

 #Cauchy distribution
 D[i] ~ dt ( central_D , precision_D, 1)

 #Likelihood
 S_y[1,i] <- 1/(sLum[1,i]^2 + sigma_f[i]^2)
 Lum[1,i] ~ dnorm ( Q[1,i] , S_y[1,i])
 Q[1,i]  <-
```

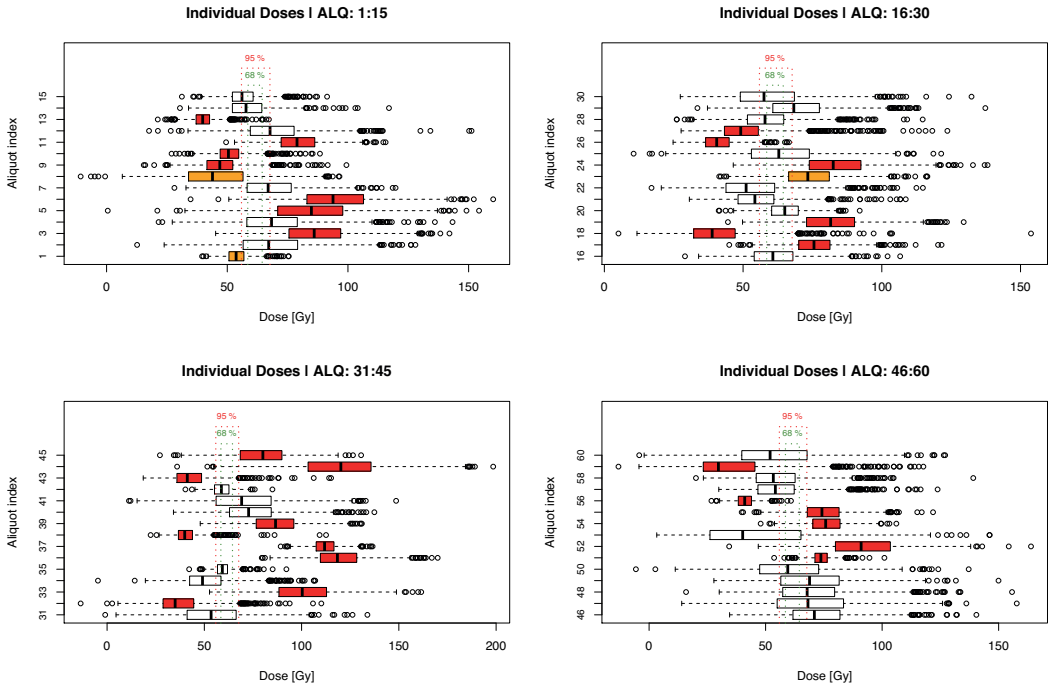

Figure 4. Boxplots of individual doses obtained during the bayesian calculation. Each box represents 50 % (interquartile range, IQR) of the data, the whiskers extend to 1.5 times this range. The HPD at its 68 % and 95 % level is indicated by the dashed lines (green and red). The plots may help to identify extreme values that might be worth a 2nd look. Box colours indicate distances of the IQR of the aliquots from the HPD. Chosen colour code: IQR outside of the HPD - 68 %: orange, IQR outside of the HPD - 95 %: red. All other boxes are coloured white. The aliquot index is indicated on the y-axis.

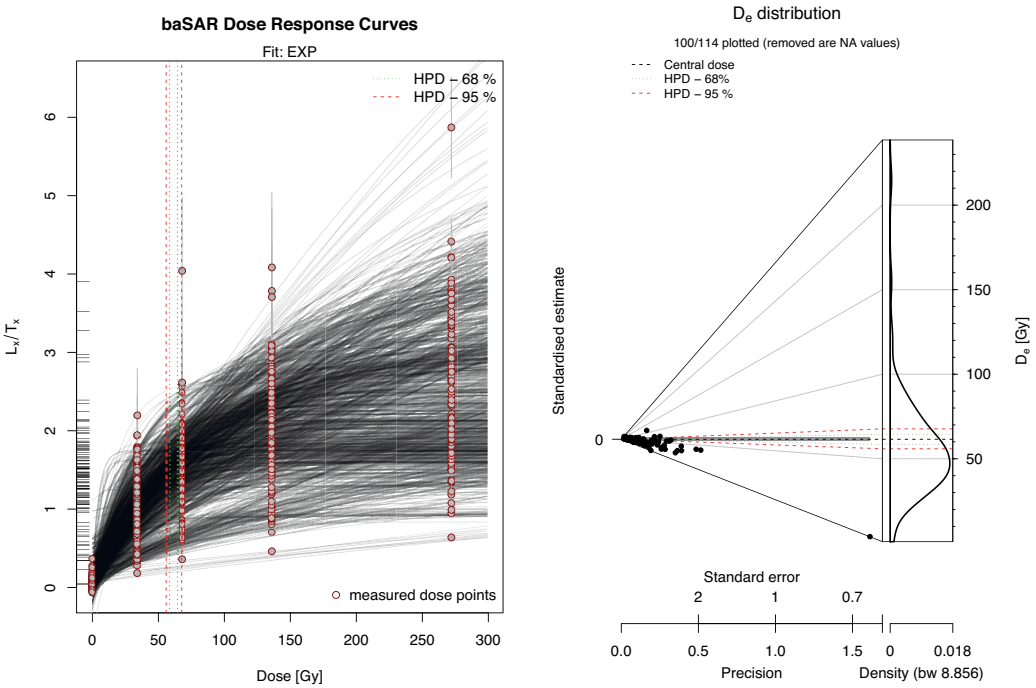

Figure 5. Dose response curves obtained using the baSAR-model (left plot) and dose distribution plot (right plot, here abanico plot; (Dietze et al., 2016)). Left plot: the individual dose response curves are plotted with the L_x/T_x values (measured dose points) used as input for the baSAR-model. For graphical reasons the maximum number of curves is limited to 1000 (randomly chosen). The plot allows to evaluate the general succession of the analysis. The right plot presents the D_e (not individual dose!) distribution. These D_e values are calculated during the preprocessing and can be considered as the 'conventional' approach of the data analysis. By contrast, the HPDs and the $\mathcal{D}$ (central dose) are indicated within the plot (dashed lines).

```
  GC_Origin * g[i] + LinGC * (c[i] * D[i] ) +
  ExpoGC * (a[i] * (1 - exp (-D[i] /b[i])))

  for (m in 2:Limited_cycles[i]) {
   S_y[m,i] <-  1/(sLum[m,i]^2 + sigma_f[i]^2)
   Lum[m,i] ~ dnorm( Q[m,i] , S_y[m,i] )
   Q[m,i]  <-
    GC_Origin * g[i] + LinGC*(c[i]*Dose[m,i]) +
    ExpoGC*(a[i] *(1 - exp(-Dose[m,i]/b[i])))
  }
 }
}"
```

For example, changing the numerical values for the first prior requires a modification of the *JAGS* code itself, i.e. the lines:

```
  #Priors
  a[i] ~  dnorm(6.5, 1/(9.2^2) ) T(0, )
```

might become

```
  #Priors
  a[i] ~  dnorm(10, 1/(100^2) ) T(0, )
```

However, it is worth mentioning that for any change of the priors or underlying assumption of the model **a rigour scientific justification is indispensable**.

Run a user-defined model is simply done by adding in the list parameters the following line:

Listing 5. Run a user-defined model

```
results <- analyse_baSAR(
 ...,
baSAR_model = my_model,
 ...
)
```

Please note that in cases where a new or a modified model is provided, the previously set of variables need to be respected, e.g., the variable `precision_D` (cf. model example above) must not be renamed, otherwise the function will crash.

4. Conclusions

An implementation and enhancement of the central dose model (baSAR) proposed by Combès et al. (2015) for the programming language **R** and the **R** package 'Luminescence' were presented along with examples. The baSAR-model can applied on single grain and multi grain aliquots measured with the SAR (Murray & Wintle, 2000) protocol. For the Bayesian modelling the software *JAGS* (Plummer, 2003) and the **R** package 'rjags' (Plummer et al., 2016) as interface is used.

This contribution did not present or discuss the underlying statistical assumptions, for this the user is referred to Combès et al. (2015). Finally it should be stressed that the availability of an easy to use software solution does not free

the user from carefully checking its own data and verify underlying assumptions.

Nota bene: For easy copy & paste code snippets and running examples the reader is referred to the supplement.

Acknowledgments

The authors gratefully acknowledge financial support by the LaScArBx. LaScArBx is a research programme supported by the ANR (ANR-10-LABX-52). SK is also thankful for the invaluable support by the **R** 'Luminescence' team and the cooperation and personal exchange funded by the DFG (SCHM 3051/3-1) in the framework of the programme "Scientific Networks", project title: "RLum.Network: Ein Wissenschaftsnetzwerk zur Analyse von Lumineszenzdaten mit **R**".

References

Bayes, T. *An Essay Toward Solving a Problem in the Doctrine of Chances*. Philosophical Transactions of the Royal Society of London, 53: 370–418, 1773.

Buck, C. E., Cavanagh, W. G., and Litton, C. *Bayesian Approach to Intrepreting Archaeological Data*. Wiley, 1996.

Combès, B., Philippe, A., Lanos, P., Mercier, N., Tribolo, C., Guérin, G., Guibert, P., and Lahaye, C. *A Bayesian central equivalent dose model for optically stimulated luminescence dating*. Quaternary Geochronology, 28: 62–70, 2015.

Cunningham, A. C., Evans, M., and Knight, J. *Quantifying bleaching for zero-age fluvial sediment: A Bayesian approach*. Radiation Measurements, 2015.

Dietze, M., Kreutzer, S., Fuchs, M. C., Burow, C., Fischer, M., and Schmidt, C. *A practical guide to the R package Luminescence*. Ancient TL, 31(1): 11–18, 2013.

Dietze, M., Kreutzer, S., Burow, C., Fuchs, M. C., Fischer, M., and Schmidt, C. *The abanico plot: visualising chronometric data with individual standard errors*. Quaternary Geochronology, 31: 12–18, 2016.

Duller, G. A. T. *The Analyst software package for luminescence data: overview and recent improvements*. Ancient TL, 33(1): 35–42, 2015.

Fuchs, M. C., Kreutzer, S., Burow, C., Dietze, M., Fischer, M., Schmidt, C., and Fuchs, M. *Data processing in luminescence dating analysis: An exemplary workflow using the R package 'Luminescence'*. Quaternary International, 362: 8–13, 2015.

Galbraith, R. F. and Roberts, R. G. *Statistical aspects of equivalent dose and error calculation and display in OSL dating: An overview and some recommendations*. Quaternary Geochronology, 11: 1–27, 2012.

Galbraith, R. F., Roberts, R. G., Laslett, G. M., Yoshida, H., and Olley, J. M. *Optical dating of single and multiple grains of Quartz from Jinmium Rock Shelter, Northern Australia: Part I, Experimental design and statistical models*. Archaeometry, 41(2): 339–364, 1999.

Gelman, A., Carlin, J. B., Stern, H. S., Dunson, D. B., Vehtari, A., and Rubin, D. B. *Bayesian Data Analysis, Third Edition*. CRC Press, 2013.

Guérin, G., Combès, B., Lahaye, C., Thomsen, K. J., Tribolo, C., Urbanova, P., Guibert, P., Mercier, N., and Valladas, H. *Testing the accuracy of a Bayesian central-dose model for single-grain OSL, using known-age samples*. Radiation Measurements, 2015.

Huntriss, A. *A Bayesian analysis of luminescence dating*. PhD thesis, University of Durham, 2008.

Kreutzer, S., Schmidt, C., Fuchs, M. C., Dietze, M., Fischer, M., and Fuchs, M. *Introducing an R package for luminescence dating analysis*. Ancient TL, 30(1): 1–8, 2012.

Kreutzer, S., Dietze, M., Burow, C., Fuchs, M. C., Schmidt, C., Fischer, M., Friedrich, J., Mercier, N., Smedley, R. K., Durcan, J., and King, G. *Luminescence: Comprehensive Luminescence Dating Data Analysis*, 2016. URL `https://CRAN.R-project.org/package=Luminescence`. R package version 0.6.4.

Murray, A. S. and Wintle, A. G. *Luminescence dating of quartz using an improved single-aliquot regenerative-dose protocol*. Radiation Measurements, 32(1): 57–73, 2000.

Peng, J. and Dong, Z. *A simple Bayesian method for assessing the standard error of equivalent dose estimates*. Ancient TL, 32(2): 17–23, 2014.

Plummer, M. *JAGS: A Program for Analysis of Bayesian Graphical Models using Gibbs Sampling*. DSC 2003 Working Papers, 124, April 2003. URL `http://mcmc-jags.sourceforge.net`.

Plummer, M., Stukalov, A., and Denwood, M. *Interface to the JAGS MCMC library*, 2016. URL `https://CRAN.R-project.org/package=rjags`. R package version 4-6.

R Development Core Team. *R: A Language and Environment for Statistical Computing*. Vienna, Austria, 2016.

Rhodes, E. J., Bronk R., C., Outram, Z., Batt, C., Willis, L., Dockrill, S., and Bond, J. *Bayesian methods applied to the interpretation of multiple OSL dates: high precision sediment ages from Old Scatness Broch excavations, Shetland Isles*. Quaternary Science Reviews, 22(10-13): 1231–1244, 2003.

Wickham, H., RStudio, Kalicinski, M., Valery, K., Leitienne, C., Colbert, B., and Hoerl, D. *Import excel files into R. Supports '.xls' via the embedded 'libxls' C library (http://sourceforge.net/projects/libxls/) and '.xlsx' via the embedded 'RapidXML' C++ library*, 2016. URL `https://CRAN.R-project.org/package=readxl`. R package version 0.1.1.

Zink, A. J. C. *Bayesian analysis of luminescence measurements*. Radiation Measurements, 2015.

Reviewer

Alastair Cunningham

Ancient TL

RLumShiny - A graphical user interface for the R Package 'Luminescence'

Christoph Burow[1*], Sebastian Kreutzer[2], Michael Dietze[3], Margret C. Fuchs[4], Manfred Fischer[5], Christoph Schmidt[5], Helmut Brückner[1]

[1] Institute of Geography, University of Cologne, 50923 Cologne, Germany
[2] IRAMAT-CRP2A, Université Bordeaux Montaigne, Maison de l'Archéologie, Esplanade des Antilles, 33607 Pessac Cedex, France
[3] Section 5.1 Geomorphology, GFZ German Research Centre for Geosciences, 14473 Potsdam, Germany
[4] Helmholtz-Zentrum Dresden-Rossendorf, Helmholtz Institute Freiberg for Resource Technology, Freiberg, Germany
[5] Geographical Institute, Geomorphology, University of Bayreuth, 95440 Bayreuth, Germany

[*]Corresponding Author: christoph.burow@uni-koeln.de

Received: November 28, 2016; in final form: December 5, 2016

Abstract

Since the release of the R package 'Luminescence' in 2012 the functionality of the package has been greatly enhanced by implementing further functions for measurement data processing, statistical analysis and graphical output. Along with the accompanying increase in complexity of the package, working with the command-line interface of R can be tedious, especially for users without previous experience in programming languages. Here, we present a collection of interactive web applications that provide a user-friendly graphical user interface for the 'Luminescence' package. These applications can be accessed over the internet or used on a local computer using the R package 'RLumShiny'. A short installation and usage guide is accompanied by the presentation of two exemplary applications.

Keywords: R, Software, GUI, Luminescence dating, Abanico Plot, Cosmic Dose Rate

1. Introduction

After its introduction in 1996 by Ihaka & Gentleman (1996) the programming language **R** (R Core Team, 2016) experienced a notable rise in popularity in the mid-2000s (Tippmann, 2015). This may owe to **R** being intuitive and easy to learn, open source, and available for all major computer platforms. A further major advantage of **R** is its easy extensibility by so-called packages, which are collections of pre-programmed routines and commands for all kinds of specialised purposes. To date, there are more than 9,600[1] packages available through the Comprehensive **R** Archive Network (CRAN)[2], contributed by users from various scientific fields. For the purpose of analysing luminescence data, Kreutzer et al. (2012) introduced the **R** package 'Luminescence'. The package provides a collection of functions to process luminescence data and includes, amongst others, routines for import and export of raw measurement files, statistical analysis of luminescence curves and spectra as well as plotting equivalent dose and/or age distributions. Throughout the years, the functionality of the package continuously increased, especially thanks to the helpful suggestions and comments by the users. As the field of applications with the latest release (version 0.6.4) is now larger than ever, the growth in functionality comes at the cost of increasing complexity. The practical guide by Dietze et al. (2013) or the worked example of Fuchs et al. (2015) aim at maintaining the usability of the package and giving a helping hand for users new to **R** and the 'Luminescence' package. In addition to tutorials dedicated to the use of **R** for luminescence data analysis available on the official

[1] https://mran.microsoft.com/, accessed: 2016-11-18.
[2] https://cran.r-project.org/, accessed: 2016-11-18.

website[3] of the **R** package 'Luminesecence' there is also a wide variety of excellent tutorials and books about **R** itself (e.g., Ligges, 2008; Adler, 2012; Crawley, 2012; Wickham, 2014).

While **R** is a comparatively easy-to-learn programming language, there is still a steep learning curve until a user is able to routinely achieve the desired results. In-depth knowledge of **R** fundamentals is not required when working with the 'Luminescence' package, but being familiar with the most important data structures in **R** is a must. In the simplest case, for a specific task, using the package only involves a single short function call, e.g., `Luminescence::plot_AbanicoPlot(data = de.data)` to produce an abanico plot (Dietze et al., 2016) of equivalent dose estimates. However, users may want to adjust the plot according to their requirements. While other software products such as *Origin*® or *SigmaPlot*® allow the user to comfortably click on each element of a plot to change its appearance, this is not possible in **R**. In **R** a plot cannot be changed after it has been drawn, and the user is required to re-run the function call with additional arguments that control the appearance of specific plot elements. For the `Luminescence::plot_AbanicoPlot()` function there are currently 33 such arguments, plus additional base **R** arguments that can be used to design the plot to ones desire. For more elaborate plots the function call in the **R** command-line rapidly increases in complexity. Users new to **R** may feel quickly overwhelmed and may hence not be able to exploit the full potential of the **R** command-line. But even experienced users may find it tedious to iteratively run the function until a satisfying results is produced. Considering that plotting data is also at least partly subject to personal aesthetic tastes in accordance with the information it is supposed to convey, iterating through all the possible options in the **R** command-line can be a time-consuming task. In Human-Computer Interaction an alternative approach to the command-line interface (CLI) is the graphical user interface (GUI), which allows direct, interactive manipulation and interaction with the underlying software. For users with little or no experience with command-lines a GUI offers intuitive access that counteracts the perceived steep learning curve of a CLI (Unwin & Hofmann, 1999).

Here, we present a GUI for the **R** package 'Luminescence' in the form of interactive web applications. These applications can be accessed online so that a user is not even required to have a local installation of **R**. The so-called shiny applications provide access to most of the plotting functions of the **R** package 'Luminescence' as well as to the functions for calculating the cosmic dose rate and for transforming CW-OSL curves (Table 1). We further introduce the **R** package 'RLumShiny' (Burow, 2016) that bundles all applications, is freely available through the CRAN and GitHub[4], and which can be installed and used in any local **R** environment. The general concept and basic layout of the applications are presented first. A short installation and usage guide of the **R** package 'RLumShiny' is then followed by a presentation of two applications for creating abanico plots and calculating the cosmic dose rate. For the latter, we also provide details on the underlying function `Luminescence::calc_CosmicDoseRate()` itself. Throughout the manuscript, **R** function calls and **R** related code listings are typed in `monospaced` letters. Functions of **R** packages other than 'RLumShiny' are given in the style of `package::function()`. **R** packages are given in single quotation marks and software programs are in *italics*.

2. Shiny applications

Even though **R** lacks native support for GUI functions, its capabilities of linking it to other programming languages allows to utilise external frameworks to build graphical user interfaces (Valero-Mora & Ledesma, 2012). Throughout the years there have been many attempts to provide the means for easier access to **R**. A non-exhaustive list of notable **R** packages linking to other languages or frameworks (given in parentheses) for building GUIs includes:

- 'rrgobi' (GGobi) (Temple Lang & Swayne, 2001; Temple Lang et al., 2016)
- 'gWidgets' (Tcl/Tk, GTK+, Java or Qt) (Verzani, 2014)
- 'cranvas' (Qt) (Xie, 2013)
- 'RGtk'/'RGtk2' (GTK+) (Robison-Cox, 2003; Lawrence & Temple Lang, 2010)
- iPlots (Java) (Urbanek & Theus, 2003; Urbanek & Wichtrey, 2013)
- 'tcltk' (Tcl/Tk) (Dalgaard, 2001a,b)

As an example, the 'tctlk' package implements an interface to the Tcl/Tk GUI toolkit and allows the user to build a Tk GUI with plain **R** code. The most prominent project making full use of the Tcl/Tk framework is the *R Commander*[5] (Fox, 2005, 2016), which provides a GUI to an exhaustive collection of statistical functions and is commonly used in teaching statistics (e.g., Konrath et al., 2013; Wagaman, 2013; Westbrooke & Rohan, 2014).

One of the more recent attempts to provide a GUI toolkit for **R** was the introduction of the 'shiny' package (Chang et al., 2016) by RStudio® in late 2012[6], which allows for building interactive web applications straight from **R**. Simple **R** code allows automatic construction of HTML, CSS and JavaScript based user interfaces. GUIs built using 'shiny' are often referred to as 'shiny applications' due to the package's name. Prior knowledge in any of these (markup-)languages is not required. The application is rendered in a web browser

[3] http://www.r-luminescence.de/, accessed: 2016-11-20.
[4] https://github.com/, accessed: 2016-11-20.
[5] *R Commander* is distributed as the **R** package 'Rcmdr' (Fox & Bouchet-Valat, 2016)
[6] https://cran.r-project.org/src/contrib/Archive/shiny/, accessed: 2016-11-18.

Table 1: Shiny applications available in the **R** package 'RLumShiny' (v0.1.1). Each application can be started using the function `app_RLum()` with the corresponding keyword as input for the parameter `app` (e.g., `app_RLum(app = 'abanico')`). * All functions are part of the 'Luminescence' package.

Application	Keyword	Function(s)*
Abanico Plot	"abanico"	`plot_AbanicoPlot()`
Radial Plot	"radialplot"	`plot_RadialPlot()`
Histogram	"histogram"	`plot_Histogram()`
Kernel Density Estimate Plot	"KDE"	`plot_KDE()`
Dose Recovery Test	"doserecovery"	`plot_DRTResults()`
Cosmic Dose Rate	"cosmicdose"	`calc_CosmicDoseRate()`
CW Curve Transformation	"transformCW"	`CW2pHMi()`, `CW2pLM()`, `CW2pLMi()`, `CW2pPMi()`

and keeps up a bidirectional communication to **R**. Any user input on the web application is automatically registered by **R**, which performs the desired action or necessary calculation and finally returns its output back to the GUI. In essence, rather than using the CLI the user operates **R** through the many pre-built and customisable input and output elements (*widgets*) for displaying plots, tables and printed output of **R** objects. One of the main advantages of 'shiny' is that the applications can be served and shared online as a web service, either by using RStudio's hosting service[7] or by installing **R** and the *Shiny Server* software on a (private) Linux server. To access the applications users only need a working internet connection and a common HTML 5 compatible browser; a local **R** environment is *not* needed. Another advantage over previous listed GUI frameworks is that 'shiny' is based on modern programming and markup languages, which allows easy integration of existing JavaScript libraries, thus greatly increasing the capabilities of 'shiny' and **R** itself.

Shiny applications generally work in any **R** environment, but we highly recommend the integrated development environment (IDE) by RStudio (RStudio Team, 2016) when the applications are run locally.

3. The R package 'RLumShiny'

While Duller (2015) acknowledges that the **R** package 'Luminescence' is capable of "extremely complex analysis", the lack of a GUI is rightfully criticised for limiting the potential user group to those with at least basic knowledge in programming. To account for the lack of a GUI and hence to make the 'Luminescence' package more accessible for users with no prior knowledge of **R** we created a collection of shiny applications (Burow et al., 2014). These applications provide a GUI to selected functions of the 'Luminescence' package, mainly, but not exclusively, focussing on its plotting capabilities (Table 1).

These shiny applications are bundled as an **R** package named 'RLumShiny' (Burow, 2016), which is distributed and freely available through the CRAN. The first version of 'RLumShiny' was released on CRAN in March 2015[8] and accumulated over 5,000 downloads[9] since then, even though it was never formally introduced to the scientific community. While it may not seem intuitive, these shiny applications were deliberately not included in the 'Luminescence' package. Much like the **R** package 'RLumModel' (Friedrich et al., 2016) for simulating luminescence in quartz, 'RLumShiny' uses the functions and object system of 'Luminescence'. But the dependency is unidirectional, meaning that 'Luminescence' does not require either of the mentioned packages in order to work. Both packages can be regarded as extensions to 'Luminescence' providing optional and particular features. For the user bundling the shiny applications in a separate package has the advantage of less overhead when installing 'Luminescence'. As 'RLumShiny' requires a couple of other **R** packages (first and foremost 'shiny' and all its sub-dependencies) installing 'Luminescence' may not only take significantly longer, but may also install packages that the user eventually does not need in case the applications are not used. Furthermore, 'RLumShiny' includes functions that extend the capabilities of 'shiny' itself (Table 2) and which should not appear in a package dedicated to the analysis of luminescence data.

From a developer's point of view, it is also easier to develop and maintain a separate **R** package as it eliminates the necessity to constantly update the code to account for changes in 'Luminescence'. Conversely, development of the 'Luminescence' package is not decelerated by the need to update the applications. Each release version of 'RLumShiny' is built and tested against a specific version of 'Luminescence'. In case of an update to a function in 'Luminescence' that breaks the corresponding shiny application in 'RLumShiny' the user is always able to revert to an earlier, compatible version of the 'Luminescence' package.

Since version 0.6.0 the 'Luminescence' package includes the homonymous function `Luminescence::app_RLum()`, a wrapper for the actual `app_RLum()` function in 'RLumShiny'. By that, users of the 'Luminescence' package are made

[7] http://www.shinyapps.io/, accessed: 2016-11-18.

[8] https://cran.r-project.org/src/contrib/Archive/RLumShiny/, accessed: 2016-11-18.

[9] Download statistics taken from https://cranlogs.r-pkg.org/, accessed: 2016-11-18.

Table 2: Functions in the **R** package 'RLumShiny' (v0.1.1). The main function is `app_RLum()`, which must be used to start any of the applications given in Table 1. All other functions are used internally and extend the functionality of the 'shiny' package.

Function	Description
`app_RLum()`	Run luminescence shiny applications.
`jscolorInput()`	Creates a JSColor widget to be used in shiny applications.
`popover()`	Create a bootstrap button with popover.
`tooltip()`	Create bootstrap tooltips for any HTML element to be used in shiny applications.

aware of the existence of a GUI, even if 'RLumShiny' is not installed. In case of the latter, running this function informs the user that 'RLumShiny' is not installed and provides instructions on how to do so if desired. Once installed it is possible to start a shiny application by either using `Luminescence::app_RLum()` or `RLumShiny::app_RLum()`.

The 'RLumShiny' package is actively developed and maintained on the web-based Git[10] repository hosting service GitHub[11]. The 'RLumShiny' applications are also available as a web service hosted on a web server maintained by the corresponding author of this article[12].

3.1. Installation and usage

To install the latest stable version of 'RLumShiny' from CRAN, simply run the code given in Listing 1 in an **R** console.

Listing 1: Install the 'RLumShiny' package from the CRAN.

```
install.packages('RLumShiny')
```

Alternatively, the user can download the latest development version of 'RLumShiny' from GitHub (Listing 2). This, however, requires the 'devtools' package, which will be installed first when executing the first two code lines of Listing 2.

Listing 2: Install the development version of 'RLumShiny' through GitHub.

```
if (!require('devtools'))
    install.packages('devtools')
devtools::install_github('R-Lum/RLumShiny')
```

Both Listing 1 and Listing 2 will install the 'RLumShiny' package and all its dependencies, i.e., other **R** packages that are required to run the applications (amongst others, most notably 'shiny' and 'Luminescence'). The user only needs to make sure to have installed the most recent version of **R** to get the most recent version of the 'RLumShiny' package (but at least version $\geq$3.1.2).

To start any of the applications included in 'RLumShiny' the user only needs to run `app_RLum()` with the corresponding keyword given in Table 1. As an example, Listing 3 shows how to run the shiny application for creating abanico plots.

Listing 3: Run the shiny application for creating abanico plots.

```
library('RLumShiny')
app_RLum(app = 'abanico')
```

Note that `library('RLumShiny')` needs to be run first when starting a new **R** session, otherwise **R** cannot find the `app_RLum()` function and returns an error. `app_RLum()` only has one named argument called `app`, which accepts all keywords listed in Table 1. Additionally, the function also accepts most arguments of the `shiny::runApp()` function (see `?shiny::runApp`). Thereby it is possible to, e.g., start an application in the so-called showcase mode[13], which presents the application along with the **R** files in the application's directory in a shared tabset.

An alternative to installing and using the 'RLumShiny' package on a local computer is to host the applications as a web service using the *Shiny Server*[14] software. This enables sharing the applications with a wider user base, whether it be an organisation, a working group or anyone interested in using it by making it freely accessible on the internet. Some of the advantages include that, amongst all potential users of the service, only one person is required to set up and maintain the Shiny Server. It has to be considered, however, that setting up a Shiny Server requires a server (or web space), which may need to be purchased or rented first, and a person with sufficient knowledge in administrating a Linux server. Furthermore, the open source version of *Shiny Server* only has a limited amount of features compared to the Pro version that is subject to fee. Nonetheless, the advantages of running a freely accessible, local or access limited Shiny Server can far outweigh these drawbacks and once set up, can provide unlimited and platform independent access to the shiny applications (cf. Fig. 1).

Due to the complexity it is, however, not within the scope of the article to provide a *Shiny Server* installation guide. The reader is referred to RStudio's offi-

[10] A version control system used in software development.

[11] https://github.com/R-Lum/RLumShiny, accessed: 2016-11-18.

[12] http://shiny.r-luminescence.de, accessed: 2016-11-18.

[13] For reference see http://shiny.rstudio.com/articles/display-modes.html, accessed: 2016-11-18.

[14] https://www.rstudio.com/products/shiny/shiny-server/, accessed: 2016-11-18.

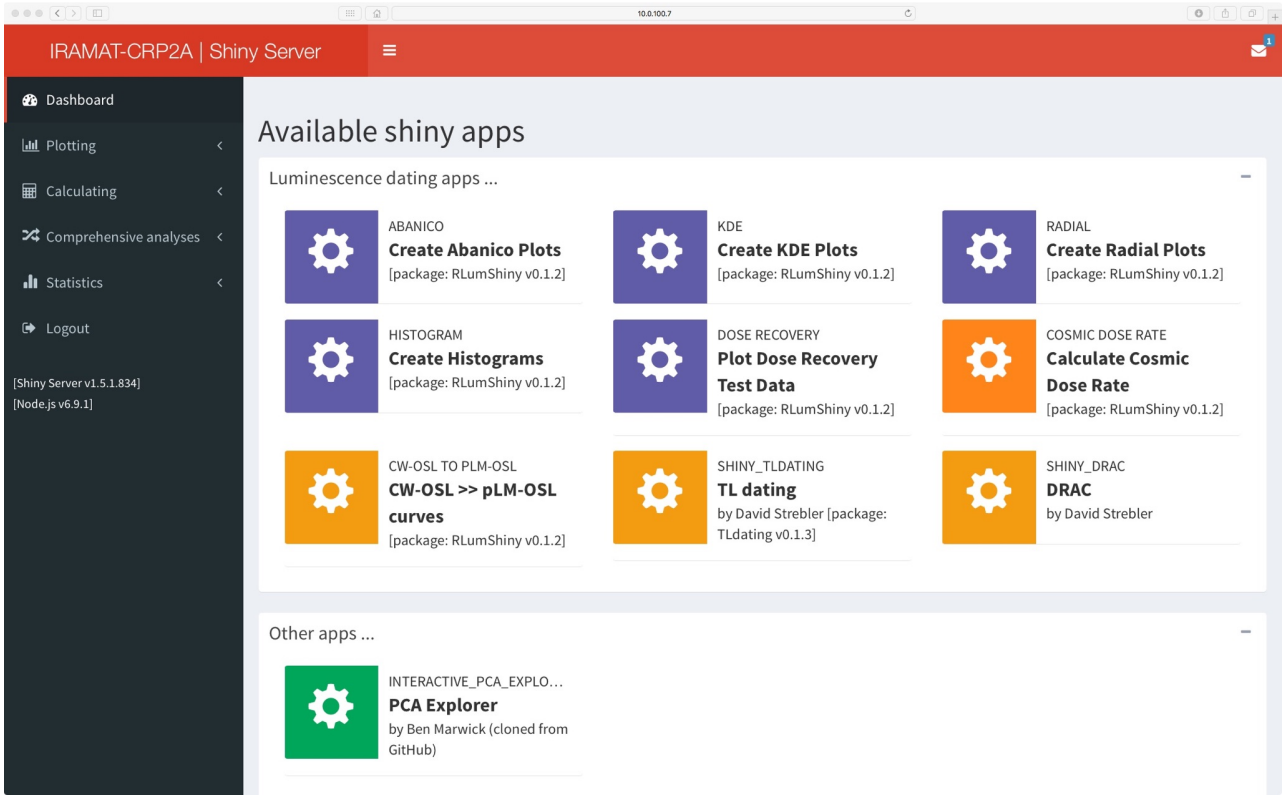

Figure 1: Example for a locally set up Shiny Server, here at the IRAMAT-CRP2A in Bordeaux. Installed are all applications available through the package 'RLumShiny' and additional applications freely available via GitHub or CRAN. The server is accessible within the local network of the IRAMAT-CRP2A only.

cial administrator's guide[15] instead. In some cases it may also be viable to use RStudio's self-service platform http://shinyapps.io, a hosting environment where users can easily upload, run and share their shiny applications. The service offers different subscription plans depending on the desired number of allowed applications, service availability and feature content.

3.2. Application layout and capabilities

Almost all shiny applications included in the 'RLumShiny' package follow a common layout style (Fig. 2). The exception to the rule is the application for calculating the cosmic dose rate, which will be presented separately in Section 3.3.2. The following layout descriptions hence refer to all applications other than the one for calculating the cosmic dose rate. A general characteristic all shiny applications share, however, is the responsive design, meaning that the layout adjusts dynamically while taking into account the characteristics of the device used. Shiny applications are thus always correctly rendered and perfectly usable on desktop computers, mobile phones and anything in between.

Currently, each application in the 'RLumShiny' package usually consists of two separate panels: an input panel on the left-hand side and an output panel on right-hand side. The top of each panel contains a varying amount of tabs (depending on the app) and a context-dependent content area below. In case of the input panel the content areas include various input widgets by which the parameters of the underlying function can be manipulated. Depending on the required data type of the manipulated function parameter these widgets include buttons, checkboxes, sliders, numeric and text input fields and others. Each time the user interacts with these elements the output is automatically updated, i.e., plots are redrawn and numeric output is recalculated.

The first tab of the input panel is always the "Data"-tab, where the user is able to provide the input data. In some cases the user is also able to provide a second data set, e.g., in the application for creating abanico plots (Section 3.3.1). Input data, usually equivalent doses and their individual errors, can be provided as plain text files. Additional options allow specifying the column separator or if the first line should be treated as column headers.

With respect to the output panel the first tab is always a plot, followed by one or two tabs showing an interactive table of the input data. In case of the plotting applications the last output tab shows a dynamically generated **R** script that can be copied to a text editor or *RStudio* and used to reproduce the current plot as seen in the "Plot"-tab. We regard

[15] http://docs.rstudio.com/shiny-server/, accessed: 2016-11-18.

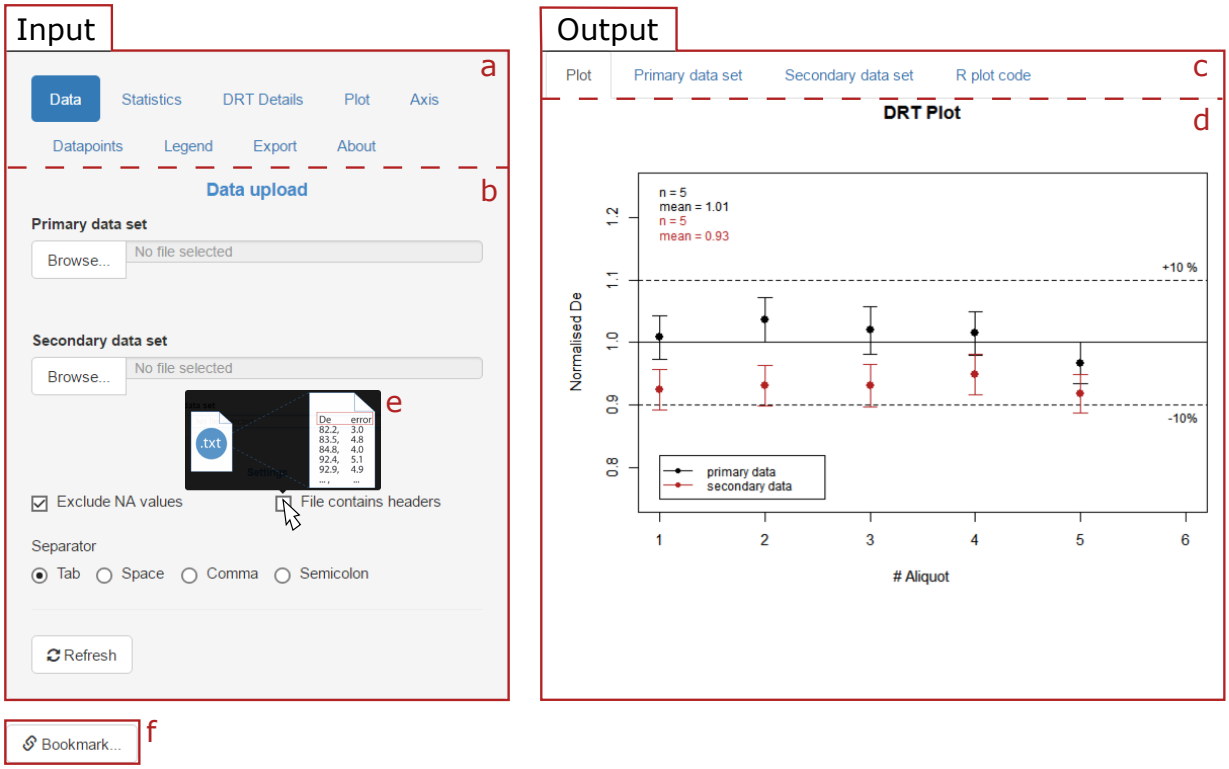

Figure 2: General layout of shiny applications in the 'RLumShiny' package. The applications follow a common GUI layout with two separate panels for input (left) and output (right). Both panels consist of a header with a varying amount of tabs (a, c) and a context-depend content area (b, d). In the example shown here (`app_RLum(app = 'doserecovery')`) (b) shows the "Data" tab content where the user is allowed to provide up to two data sets as an ASCII text file. Additional check boxes and radio buttons allow for providing the files in various style formats. Some of the input elements provide custom tooltips with graphical or text information (e). The "Bookmark" button (f) below the input panel allows saving the current state of the application. The user is provided an URL, which can be used to restore the session, i.e. all previous settings and provided data are automatically restored.

this as a valuable addition as (i) users may use this as a help to understand all the arguments of a particular function and are able to see how they should be used, and (ii) it provides the means to fully reproduce the plot from the CLI or in an existing **R** script.

Naturally, all applications for generating plots offer an export section, which is accessed by the second to last tab on the input panel (Fig. 3). There, the user is able to save the generated plot in a vector graphics format (PDF, SVG or EPS). Note that the plot dimensions in the exported file usually differ from those seen in the "Plot"-tab, as the latter is dynamically rescaled depending on the current size of the viewport. The height and width of the exported image can be specified separately. Additionally, the user can download an **R** script that includes the code required to reproduce the plot from the CLI.

3.3. Example applications

In the current version of 'RLumShiny' (v0.1.1) more than half of all included applications are exclusively there for creating graphical output. The remaining applications are to calculate the cosmic dose rate and to transform continuous-wave OSL curves to a pseudo hyperbolic, linearly or parabolic modulated curve (Table 1). In the following, specific capabilities of the 'RLumShiny' package are exemplified by the applications for creating an abanico plot and for calculating the cosmic dose rate.

3.3.1 Abanico Plot

The abanico plot was introduced by Dietze et al. (2016), a novel plot type for showing chronometric data with individual standard errors. In essence, it is a combination of a radial plot (Galbraith, 1988) and a kernel density estimate (KDE) plot (cf. Galbraith & Roberts, 2012), which can be created using the **R** function `Luminescence::plot_AbanicoPlot()`. To produce a ready-to-use plot the user only needs to provide some input data. Yet, `Luminescence::plot_AbanicoPlot()` offers 33 arguments and an uncounted number of base **R** arguments that can be used to style the plot to ones desire. As plots generated in **R** cannot be changed after they have been drawn the user is required to repeatedly run the function call

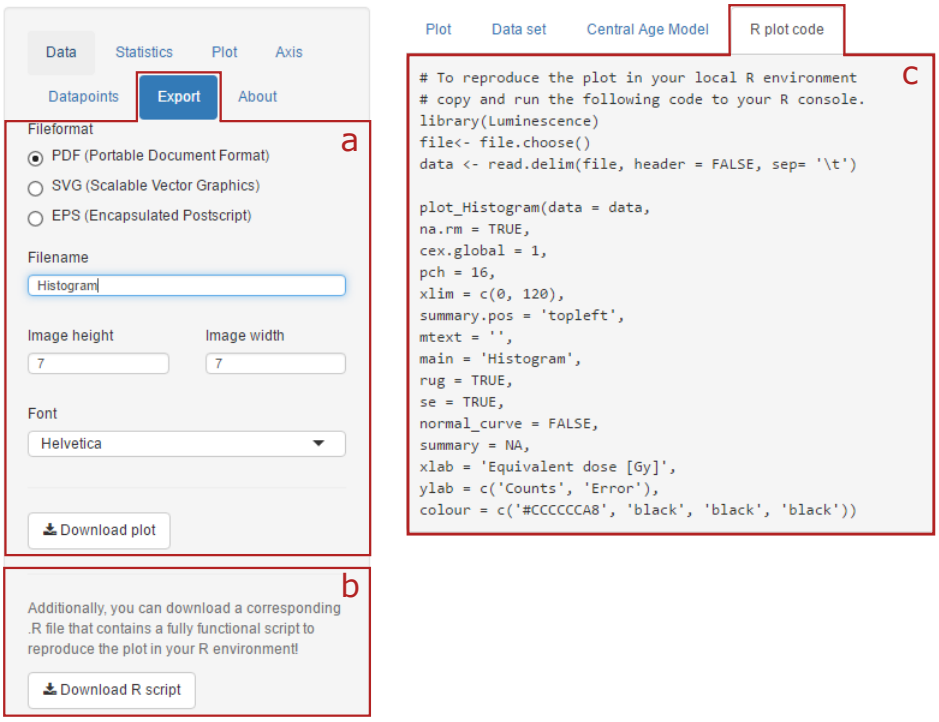

Figure 3: File export options available for the histogram application (`app_RLum(app = 'histogram')`). All plotting applications of the **R** package 'RLumShiny' include an export tab in the input panel, which (a) offers the possibility to save the generated plot as a vector graphics file (file types: PDF, SVG, EPS). Additionally, (b) the user can download an **R** script file that includes the code shown in in the output panel (c), which can be used to reproduce the generated plot in any other **R** environment that has the 'Luminescence' package installed. Alternatively, the user can also just copy and paste the code in (c) and execute it in an **R** console.

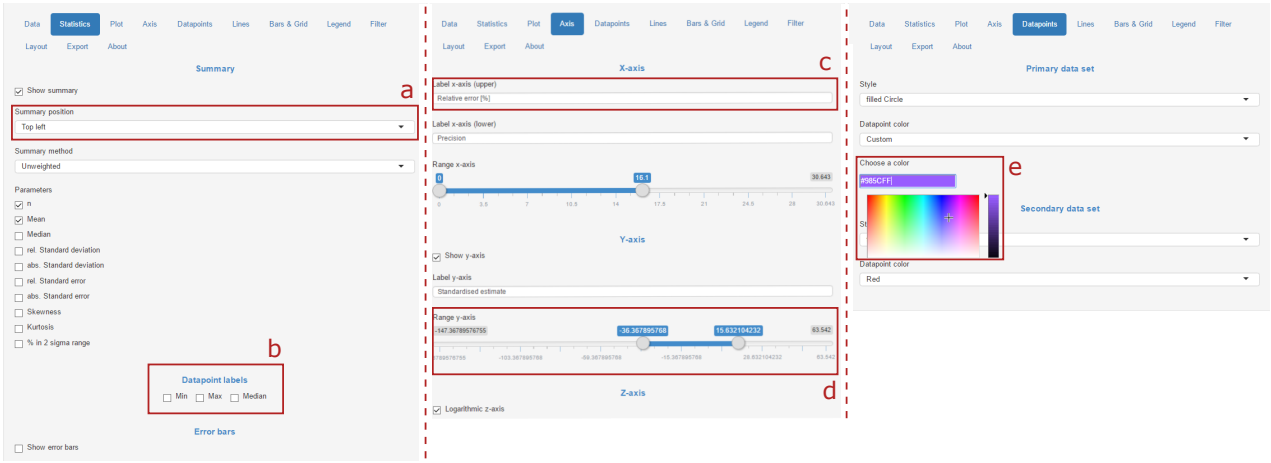

Figure 4: A selection of input options available in the shiny application to generate abanico plots. a) Mutually exclusive options such as the summary position are often manipulated using a drop down menu. b) Binary options like showing or hiding numerical information on the plot can be controlled by checkboxes. c) Plot annotations and axis labels can be changed by text input fields. d) Function arguments requiring a single numeric value or a range of values can be controlled by regular or double-ended range sliders. e) 'RLumShiny' includes the JavaScript library *JSColor* (Odvarko, 2014) along with a custom 'shiny' binding. In this example, if the user chooses "Custom" for the datapoint colour a text input field and a colour table appears, from which a colour can be picked. Alternatively, a hexadecimal RGB value can be typed in directly.

while iteratively changing the input parameters. Even for experienced users this may be a tedious and time-consuming task.

Compared to all other shiny applications in 'RLumShiny' the GUI for generating abanico plots offers the highest number of input widgets (Fig. 4). Generally, a numeric range (e.g., axis limits) is usually controlled with a regular or double-ended range slider, binary options (e.g., showing or hiding the summary) with checkboxes and mutually exclusive options (e.g., line type) with radio buttons or drop down menus. Text fields are mostly used to manipulate plot annotations and axis labels.

The `jscolorInput()` function in 'RLumShiny' extends the 'shiny' interface by including the web colour picker *JSColor*[16] (Odvarko, 2014). When the user chooses "Custom" as input in one of the colour drop down menus (e.g., in the "Datapoint"-tab) a new text input field appears. There, the user is able to enter a hexadecimal RGB value or to pick a colour from a small colour table that appears when the user clicks in the input field.

3.3.2 Cosmic dose rate

The shiny application for calculating the cosmic dose rate is chosen as an example (i) to take the opportunity to provide details on the underlying function `Luminescence::calc_CosmicDoseRate()`, (ii) as its layout differs from all other applications in 'RLumShiny', and (iii) as it includes a unique feature.

Despite its universal use, the equation to calculate the cosmic dose rate provided by Prescott & Hutton (1994) is falsely stated to be valid from the surface to 10^4 hg cm^{-2} (1 hg cm^{-2} = 100 g cm^{-2}) of standard rock[17]. The original expression by Barbouti & Rastin (1983) only considers the muon flux (i.e., the hard-component of the cosmic flux) and is, by their own account, only valid for depths between 10 hg cm^{-2} and 10^4 hg cm^{-2}. Thus, for near-surface samples (i.e., for depths <167 g cm^{-2}) the equation of Prescott & Hutton (1994) underestimates the total cosmic dose rate as it neglects the influence of the soft-component of the cosmic flux. For samples at zero depth and at sea-level the underestimation can be as large as ~0.1 Gy ka^{-1}. In a previous article, Prescott & Hutton (1988) give another approximation of the equations in Barbouti & Rastin (1983) in the form of

$$\dot{D}_c = 0.21\, e^{(-0.07\, x\, +\, 5\times10^{-4}\, x^2)} \quad (1)$$

where $\dot{D}_c$ is the cosmic dose rate in Gy ka^{-1} and x is the depth in hg cm^{-2}. This expression is valid for depths between 150 g cm^{-2} and 5000 g cm^{-2}. For shallower depths (<150 g cm^{-2}) the cosmic dose rate must be read from Figure 1 in Prescott & Hutton (1988). As a result, `Luminescence::calc_CosmicDoseRate()` employs Equation 2 of Prescott & Hutton (1994) only for

[16] http://jscolor.com/, accessed: 2016-11-18.

[17] To obtain the depth in units of centimeters values given in g cm^{-2} must be divided by the material's density (in g cm^{-3}). Example: In a sediment of density 1.8 g cm^{-3}, 167 g cm^{-2} equates to a sample depth of ~93 cm.

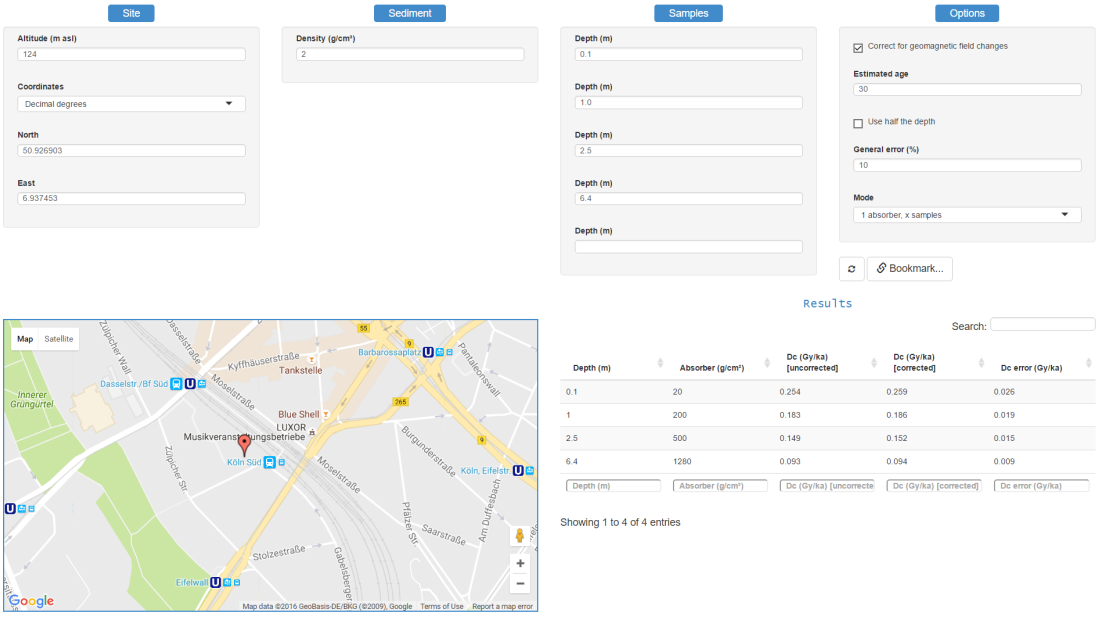

Figure 5: Shiny application for calculating the cosmic dose rate using the **R** function `Luminescence::calc_CosmicDose()`. In contrast to most other applications in 'RLumShiny' this application only provides numerical output (bottom right). A unique feature of this application is the use of Google Maps™ (using the 'googleVis' package (Gesmann & de Castillo, 2011)), which serves as a visual control to whether the provided longitude and latitude are correct.

depths >167 g cm^{-2}, i.e., only for the hard-component of the cosmic flux. Cosmic dose rate values for depths <167 g cm^{-2} were carefully reproduced from Figure 1 in Prescott & Hutton (1988) and fitted with a 6-degree polynomial curve. When the user provides a sample depth smaller than 167 g cm^{-2} the cosmic dose rate is thus estimated from the fitted curve instead.

With regards to the shiny application for `Luminescence::calc_CosmicDoseRate()` its comparatively small number of arguments (n = 9) favoured a "flatter" design, i.e., making all options available in one panel without separate tabs (Fig. 5). This resulted in a horizontally aligned interface, with the user input at the top and the output at the bottom. A unique feature of this application is the implementation of a Google Map by using the 'googleVis' package (Gesmann & de Castillo, 2011). As the latitude and longitude are compulsory for calculating the cosmic dose rate, the provided values are also used for finding the place on the Google Map. This serves as a visual control as to whether the provided values are correct. Finally, the application enhances the underlying `Luminescence::calc_CosmicDoseRate()` by allowing the user to provide the longitude and latitude in different coordinate formats, which are internally converted to decimal degrees as required by the function.

4. Discussion

This contribution introduced so-called shiny applications, which provide a graphical user interface to a selected number of functions of the **R** package 'Luminescence'. Built using the 'shiny' framework, the user is presented a scalable and intuitive GUI allowing for direct manipulation and interaction with the underlying **R** functions.

While we are confident that these applications lower the entry threshold for users new to **R** or the **R** package 'Luminescence', installing and using the 'RLumShiny' package in a local **R** environment is still not (and probably never will be) as straightforward as standalone software such as *Analyst* (Duller, 2015) or *RadialPlotter* (Vermeesch, 2009). The user is still required to install **R**, an IDE (e.g., *RStudio*) and finally all required **R** packages, notably 'Luminescence' and 'RLumShiny'. Usage of 'RLumShiny' is kept as easy as possible, however, as the user only needs to remember one single function (`app_RLum()`) and the keywords given in Table 1 to start a particular application.

Ideally, shiny applications are shared as web applications served by a dedicated server running **R** and *Shiny Server*. While this requires potentially investing in a corresponding infrastructure (e.g., renting web space) and a person experienced in setting up and maintaining a Linux server, the aforementioned drawbacks are largely eliminated. Once a Shiny Server is up and running, all the users need to do is to enter a specific URL in a HTML 5 compatible web browser; a local **R** environment is no longer needed. Furthermore, access permissions to the shiny applications can be controlled by the server administrator.

A general limitation to providing a GUI to **R** in general and the 'Luminescence' package in particular is that the user is always limited to the options provided by the GUI. For example, the function `Luminescence::plot_AbanicoPlot()` accepts a theoretically infinite number of input data, but is restricted to two data sets in the shiny application; otherwise, the GUI would become too convoluted. The user is thus required to revert to the CLI when the GUI does not provide the necessary means to fulfil the desired task. In essence, a CLI will always be more powerful than a GUI.

A specific limitation of the 'RLumShiny' package is that the currently included applications cover only a fairly restricted amount of functions of the 'Luminescence' package. Most applications provide a GUI to plotting functions and to a few functions dedicated to very specific problems (such as calculating the cosmic dose rate or transforming CW-OSL curves). There is no application dedicated to the analysis of raw luminescence data (e.g., `Luminescence::analyse_SAR.CWOSL()`) yet, which, without doubt, would also profit from a GUI. It is the aim of the authors to develop more shiny applications in the future. We may also invite other **R** users to contribute and further improve the package.

In summary, we believe the presented shiny applications, bundled in the **R** package 'RLumShiny', are a welcome contribution to the luminescence community and a useful addition to the **R** package 'Luminescence'. It is designed to be used by both users with, and without, prior knowledge of **R**.

5. Conclusion

The authors of the **R** package 'Luminescence' (Kreutzer et al., 2016) are fully aware that, despite its capabilities for complex and non-standard analysis of luminescence data, working with the command-line interface of **R** can be tedious at best and overwhelming at worst. Even though much work is put into simplifying the usage of the package to continuously lower the entry threshold, at least basic knowledge of **R** will always be required. Thus, the potential user base of the package cannot be exhausted, at least as long as the CLI is the only means of utilising the 'Luminescence' package.

As an alternative to the CLI, a graphical user interface allows for direct, interactive manipulation and interaction with the underlying software. For users with little or no experience with command-lines a GUI offers intuitive access that counteracts the perceived steep learning curve of a CLI (Unwin & Hofmann, 1999). To account for the demand of a GUI for the **R** package 'Luminescence' we presented a series of so-called shiny applications. These applications are built using the 'shiny' framework (Chang et al., 2016), which allows building a HTML, CSS and JavaScript based GUI straight from **R**. These applications are bundled in the **R** package 'RLumShiny' (Burow, 2016), which is freely available either through the CRAN (`https://CRAN.R-project.org/package=RLumShiny`) or from GitHub (`https://github.com/R-Lum/RLumShiny`).

The shiny applications included in 'RLumShiny' can be (i) used on a local computer with a working **R** environment, or (ii) shared as web applications with a wider audience (e.g., an organisation or working group) by setting up a Shiny Server. A Shiny Server run by the authors of this article can be freely accessed under http://shiny.r-luminescence.de. Note, however, that the performance of this server is fairly limited and not indicative for the general performance of shiny applications.

The current version of 'RLumShiny' (v0.1.1) includes a total of seven applications providing a GUI to ten functions of the 'Luminescence' package. Hence, there are many more functions that may greatly benefit from a GUI, and it is the aim of the authors to provide more shiny applications in the future. Finally, herewith we invite everyone to contribute to this package. 'RLumShiny' and the included JavaScript library *JSColor* (Odvarko, 2014) are licensed under the GNU General Public License version 3 (GPL-3). Code derived from the 'shinysky' package (AnalytixWare, 2014) is covered by the MIT licence.

Acknowledgments

We are thankful to the **R** Core Team for providing the **R** programming environment (R Core Team 2016) and the CRAN mirrors for open access to **R** packages. Cooperation and personal exchange between the package developers is gratefully funded by the DFG (SCHM3051/3-1) in the framework of the program 'Scientific Networks'. The work of SK is financed by a programme supported by the ANR (n°ANR-10-LABX-52).

References

Adler, J. *R in a Nutshell*. Oreilly & Associates Incorporated, 2nd edition, 2012.

AnalytixWare. *shinysky: A set of Shiny UI components/widgets.*, 2014. URL https://github.com/AnalytixWare/ShinySky. R package version 0.1.2.

Barbouti, A.I. and Rastin, B.C. *A study of the absolute intensity of muons at sea level and under various thicknesses of absorber*. Journal of Physics G: Nuclear and Particle Physics, 9: 1577–1595, 1983.

Burow, C. *RLumShiny: 'Shiny' Applications for the R Package 'Luminescence'*, 2016. URL https://CRAN.R-project.org/package=RLumShiny. R package version 0.1.1.

Burow, C., Kreutzer, S., Dietze, M., Fuchs, M.C., Fischer, M., Schmidt, C., and Brückner, H. *Shiny R.Lum - Interactive web applications for the R packages 'Luminescence' and 'ESR'*. In *German Luminescence- and ESR-Meeting 2014, Gießen.*, 2014. URL http://www.r-luminescence.de/grafik/poster_screenshots/2014_Poster_LED_Giessen_g.jpg. Poster presentation.

Chang, W., Cheng, J., Allaire, JJ., Xie, Y., and McPherson, J. *shiny: Web Application Framework for R*, 2016. URL https://CRAN.R-project.org/package=shiny. R package version 0.13.2.

Crawley, M.J. *The R Book*. Wiley, 2nd edition, 2012.

Dalgaard, P. *A Primer on the R-Tcl/Tk Package*. R News, 1(3): 27–31, 2001a.

Dalgaard, P. *The R-Tcl/Tk interface*. In Hornik, K. and Leisch, F. (eds.), *Proceedings of the 2nd International Workshop on Distributed Statistical Computing*, 2001b.

Dietze, M., Kreutzer, S., Fuchs, M.C., Burow, C., Fischer, M., and Schmidt, C. *A practical guide to the R package Luminescence*. Ancient TL, 31: 11–18, 2013.

Dietze, M., Kreutzer, S., Burow, C., Fuchs, M.C., Fischer, M., and Schmidt, C. *The abanico plot: visualising chronometric data with individual errors*. Quaternary Geochronology, 31: 12–18, 2016.

Duller, G.A.T. *The Analyst software package for luminescence data: overview and recent improvements*. Ancient TL, 33(1): 35–42, 2015.

Fox, J. *The R Commander: A Basic-Statistics Graphical User Interface to R*. Journal of Statistical Software, 14(9): 1–42, 2005.

Fox, J. *Using the R Commander: A Point-and-Click Interface for R*. Chapman and Hall/CRC, 2016.

Fox, J. and Bouchet-Valat, M. *Rcmdr: R Commander*, 2016. URL https://CRAN.R-project.org/package=Rcmdr. R package version 2.3-1.

Friedrich, J., Kreutzer, S., and Schmidt, C. *Solving ordinary differential equations to understand luminescence: RLumModel, an advanced research tool for simulating luminescence in quartz using R*. Quaternary Geochronology, 35: 88–100, 2016.

Fuchs, M.C., Kreutzer, S., Burow, C., Dietze, M., Fischer, M., Schmidt, C., and Fuchs, M. *Data processing in luminescence dating analysis: An exemplary workflow using the R package 'Luminescence'*. Quaternary International, 362: 8–13, 2015.

Galbraith, R. and Roberts, R.G. *Statistical aspects of equivalent dose and error calculation and display in OSL dating: An overview and some recommendations*. Quaternary Geochronology, 11: 1–27, 2012.

Galbraith, R.F. *Graphical Display of Estimates Having Differing Standard Errors*. Technometrics, 30: 271–281, 1988.

Gesmann, M. and de Castillo, D. *Using the Google Visualisation API with R*. The R Journal, 3(2): 40–44, December 2011.

Ihaka, R. and Gentleman, R. *R: A Language for Data Analysis*. Journal of Computational and Graphical Statistics, 5(3): 299–314, 1996.

Konrath, A.C., Henning, E., Walter, O.M.F.C, da Cunha Alves, C., and Samohyl, R.W. *Applications in teaching Statistical Quality Control with different R interfaces*. In *Global Engineering Education Conference (EDUCON), 2013 IEEE*, pp. 146–155, March 2013. doi: 10.1109/EduCon.2013.6530099.

Kreutzer, S., Schmidt, C., Fuchs, M.C., Dietze, M., Fischer, M., and Fuchs, M. *Introducing an R package for luminescence dating analysis*. Ancient TL, 30: 1–8, 2012.

Kreutzer, S., Dietze, M., Burow, C., Fuchs, M.C., Schmidt, C., Fischer, M., Friedrich, J., Mercier, N., Smedley, R.K., Durcan, J., and King, G. *Luminescence: Comprehensive Luminescence Dating Data Analysis*, 2016. URL https://CRAN.R-project.org/package=Luminescence. R package version 0.6.4.

Lawrence, M. and Temple Lang, D. *RGtk2: A Graphical User Interface Toolkit for R*. Journal of Statistical Software, 37(8): 1–52, 2010. URL http://www.jstatsoft.org/v37/i08/.

Ligges, U. *Programmieren mit R (Statistik und ihre Anwendungen)*. Springer, 3rd edition, 2008.

Odvarko, J. *jscolor - JavaScript Color Picker (v1.4.4)*. https://github.com/EastDesire/jscolor, 2014. GitHub repository.

Prescott, J.R. and Hutton, J.T. *Cosmic ray and gamma ray dosimetry for TL and ESR*. Nuclear Tracks and Radiation Measurements, 14: 223–227, 1988.

Prescott, J.R. and Hutton, J.T. *Cosmic ray contributions to dose rates for luminescence and ESR dating: large depths and long-term time variations*. Radiation Measurements, 23: 497–500, 1994.

R Core Team. *R: A Language and Environment for Statistical Computing*. R Foundation for Statistical Computing, 2016. URL https://www.R-project.org/.

Robison-Cox, J. *Putting RGtk to Work*. In Hornik, K., Leisch, F., and Zeileis, A. (eds.), *Proceedings of the 3rd International Workshop on Distributed Statistical Computing*, 2003.

RStudio Team. *RStudio: Integrated Development Environment for R*. RStudio, Inc., 2016. URL https://www.rstudio.com/.

Temple Lang, D. and Swayne, D.F. *GGobi meets R: an extensible environment for interactive dynamic data visualization*. In Hornik, K. and Leisch, F. (eds.), *Proceedings of the 2nd International Workshop on Distributed Statistical Computing*, 2001.

Temple Lang, D., Swayne, D., Wickham, H., and Lawrence, M. *rggobi: Interface Between R and 'GGobi'*, 2016. URL https://CRAN.R-project.org/package=rggobi. R package version 2.1.21.

Tippmann, S. *Programming tools: adventures with R*. Nature, 517: 109–110, 2015.

Unwin, A. and Hofmann, H. *GUI and Command-line - Conflict or Synergy?* In Berk, K. and Pourahmadi, M. (eds.), *Computing Science and Statistics*, Proceedings of the 31st Symposium on the Interface, pp. 246–253, 1999.

Urbanek, S. and Theus, M. *iPlots - High Interaction Graphics for R*. In Hornik, K., Leisch, F., and Zeileis, A. (eds.), *Proceedings of the 3rd International Workshop on Distributed Statistical Computing*, 2003.

Urbanek, S. and Wichtrey, T. *iplots: iPlots - interactive graphics for R*, 2013. URL https://CRAN.R-project.org/package=iplots. R package version 1.1-7.

Valero-Mora, P. and Ledesma, R. *Graphical User Interfaces for R*. Journal of Statistical Software, 49(1): 1–8, 2012. ISSN 1548-7660. doi: 10.18637/jss.v049.i01. URL https://www.jstatsoft.org/index.php/jss/article/view/v049i01.

Vermeesch, P. *RadialPlotter: a Java application for fission track, luminescence and other radial plots*. Radiation Measurements, 44: 409–410, 2009. URL http://www.ucl.ac.uk/~ucfbpve/radialplotter/.

Verzani, J. *gWidgets: gWidgets API for building toolkit-independent, interactive GUIs*, 2014. URL https://CRAN.R-project.org/package=gWidgets. Based on the iwidgets code of S. Urbanek and suggestions by S. Urbanek and P. Grosjean and M. Lawrence. R package version 0.0-54.

Wagaman, A. S. *Meeting Student Needs for Multivariate Data Analysis: A Case Study in Teaching a Multivariate Data Analysis Course with No Pre-requisites*. ArXiv e-prints, 2013. URL https://arxiv.org/pdf/1310.7141v1.

Westbrooke, I. and Rohan, M. *Statistical Training in the Workplace*. In MacGillivray, H., Phillips, B., and Martin, M.A. (eds.), *Topics from Australian Conferences on Teaching Statistics*, pp. 311–327, New York, 2014. Springer New York. ISBN 978-1-4939-0603-1. doi: 10.1007/978-1-4939-0603-1_17.

Wickham, H. *Advanced R*. Chapman & Hall, 2014.

Xie, Y. *Interactive statistical graphics based on Qt*, 2013. URL https://github.com/ggobi/cranvas. R package version 0.8.5.

Reviewer

Shannon Mahan

Reviewer's comment

In this paper, Burow et al. present a graphical user interface (GUI) for the **R** package 'Luminescence' using the **R** 'shiny' package. **R** 'shiny' is a way to create GUIs for **R** functions and has the capability to be hosted as web applications. As many readers will already know, the **R** 'Luminescence' package is a very powerful tool for conducting statistical treatment of luminescence data and age determinations. One problem, that the authors also note, is that the command line interface of **R** is not very user friendly and can be frustrating and sometimes difficult for even users familiar with the language. The GUI helps avoid this issue and highlights many options in **R** that a user may not know or understand. Although some prior knowledge is necessary to run the GUI, and programs like *Analyst* and *Radialplotter* may always be more intuitive to use, the authors acknowledge this well and, in my opinion, do a good job of describing what 'RLumShiny' is and isn't capable of.

Thesis Abstracts

Index

Helena Asmar de Abreu Andrade

Sedimentary evolution and chronology of the Maçambaba Quaternary coastal barrier: the influence of the winds from opposite directions and their possible paleoclimate meaning

August 2015

Instituto de Geociências, Universidade de São Paulo, São Paulo, Brazil

Degree: M.Sc.

Supervisor: Paulo César Fonseca Giannini

The Maçambaba Quaternary coastal sand barrier is located between Saquarema and Arraial do Cabo, immediately westward of the abrupt change in the Rio de Janeiro state (Southeastern Brazil) coastline orientation, from SW-NE to W-E, which is one of the main factors determining the coastal upwelling phenomenon in this area. The cooling of the coastal waters by the upwelling explains the relatively low local precipitation indices (less than 1000 mm/year). This coastal barrier was studied with regard to geomorphology, sedimentology (grain size, heavy minerals and limestone petrography) and geochronology (^{14}C AMS and OSL dating). It is represented by two barriers parallel to the coast, tens of kilometers long, deposited during each one of the last events of relative sea level rise (RSL), in the upper Pleistocene (MIS 5e, with maximum RSL around 120 ky ago) and Holocene (MIS 1, with maximum RSL around 5.5 ky ago). The hypersaline Araruama lagoon system is a drowned incised valley up to 8 m deep and 30 km long, that separates the Pleistocene barrier from the pre-Quaternary basement. In the western half, another lagoon system, narrower, shallower and also hypersaline, occurs between the Holocene and Pleistocene barriers. It was generated contemporaneously with the Holocene barrier, thereby having a backbarrier character. Maximum ages obtained at the bottom of the incised valley (6.0 ky BP) and at the backbarrier lagoon deposits (7.0 ky BP) suggest that the two lagoon systems were flooded at the same time during the Holocene transgression. Two aeolian systems with opposite migration direction occur due the alternation between the SW and NE effective wind drift during that time. The system formed by the winds to NE is derived from the beach sands and is characterized by foredunes with increasing height from W to E and by blowouts in the eastern part. This reflects the more dissipative beach eastward and the increase of sediment supply related to the net longshore drift in that direction. The blowouts interrupt the foredunes and play the role of channels in overwash processes. The aeolian system with migration direction to SW occurs as active blowouts and isolated parabolics, which rework the distal part of the eastern washover fans, and as two parabolic paleo dunefields originated in the Araruama lagoon southern shore. These paleo dunefields were formed during the lagoon shore erosional periods. The oldest one, with OSL ages between 7.0 and 6.0 ky, is contemporary to the lagoon maximum flood and is related to the erosion induced by transgression, whilst the new one (OSL age 1.5 ky), immediately westward, is related to lagoon shore erosion linked to circulation changes induced by cuspate spits growth. Besides the evident sediment supply influence, the dune formation is also affected by the climate: the coastal upwelling, and consequently more arid climate in the area are favored by winds to SW. Thus, the age of the new generation of paleo dunefields to SW and the lagoonal calcrete formation age (2.4 cal ky BP) suggest upwelling intensification and aridity increase during the late Holocene.

A PDF of this thesis can be downloaded from: http://www.teses.usp.br/teses/disponiveis/44/44141/tde-22092015-150237/pt-br.php

Xinfu Bao

Lateral intra-stratigraphic sedimentological variations in archaeologically-rich Quaternary karstic complexes: implications on luminescence dating - the case of Galería, Sierra de Atapuerca, Spain

September 2016

CENIEH, Burgos, Spain
University of the Basque Country (EHU/UPV), Leioa, Spain

Degree: M.Sc.

Supervisors: Gloria I. López and Josep M. Parés

Galería is one of the most significant Pleistocene karst cavities situated in the Sierra de Atapuerca Complex (North-Central Spain), known worldwide for its richness in terms of hominid skeletal fossils, abundant Acheulean lithic artefacts as well as synchronous mammal remains and microvertebrate assemblages since excavations begun in the 1980s. Over the years, the Complex has been dated by multiple methods, including palaeomagnetic measurements and independent numerical chronologies including luminescence (in

the forms of thermo-luminescence TL, optically stimulated luminescence OSL, infrared stimulated luminescence IRSL, and their corresponding sub-techniques), electron spin resonance (ESR) and uranium-thorium (U-Th) dating applied to both clastic sediments and speleothems. Despite the abundance of methodologies, a conspicuous inconsistency between the previously published ages has been observed in an area that barely exceeds 17 m in length and where the different sampled sites are on similar and/or juxtaposed lithological units/levels, only a few centimeters apart.

In this research, lateral sedimentological facies variations within an individual archaeologically-rich layer of the Galera karstic infill were investigated using a novel multi-proxy investigative approach, including a first-time reported horizontal luminescence profiling. The results from the poly-mineral luminescence signal analysis and OSL ages, sedimentological characteristics (e.g. particle size, textural maturity, grain micro-morphology, mineralogical composition), dosimetry and magnetic properties (i.e. magnetic susceptibility, matrix micro-fabric anisotropy) of this layer helped not only to better elucidate the complexities of the evolution of the karstic landscape but also to ascertain the existence of multiple sediment sources and transport paths of the infilling sediments. In our case, the new single grain thermally-transferred TT-OSL ages showed ∼100,000 years difference from one end of the studied layer to the other, confirming different age values due to marked lateral sedimentological facies variations, most likely associated to varying environmental factors and mineral provenance.

This intra-stratigraphic, lateral profiling, multi-proxy analytical approach showed the need to do more detailed geological and stratigraphical work prior to any detailed geochronological endeavour. Moreover, it exposed the complexity of assigning singular and unique numerical ages to individual levels/units/strata in infilled karstic archaeological sites, demonstrating that more care should be taken when selecting sampling locations for age determination in areas of complex stratigraphy and layers of intricate sedimentology and depositional patterns.

Valentina Espinel Arias

Morphology, depositional facies and chronology of Quaternary eolianites of the Piauí and Ceará coast, Northeast Brazil

November 2015

Instituto de Geociências, Universidade de São Paulo, São Paulo, Brazil

Degree: M.Sc.

Supervisor: Paulo César Fonseca Giannini

The active dune fields and the eolianites between Luís Correa (Piauí State) and Pararucu (Ceará State), Northeastern Brazil, are located in the area of the Intertropical Convergence Zone influence, from which originate the trade winds responsible for their formation. The variation of the direction in which these winds reach the coast is the main criterion for dividing the study area into three sectors: west, center and east. In each sector, the direction of the effective wind, combined with the coastline orientation, determines the deflation plain development, which increases with the angle between wind and coast. The eolianites appear as discontinuous ridges, parallel to the direction of the effective wind. They occur in the deflation plain and exhibit similar morphology to active trailing ridges. Quartz grain dating by luminescence (OSL) and bioclast or calcite cement dating by ^{14}C AMS indicate ages between 650 and 5700 years. The eolianites nearest to the coastline are older than the farthest ones, a pattern expected in trailing ridges, which are successively left behind and stabilized as the dune field migrates. The concentration of Brazilian eolianites in this area is related to the adjacent inner continental shelf constitution, which is rich in branching red algae and rhodoliths. Keywords: carbonate paleodunes, deflation plain, trailing ridges, dating, Holocene paleoclimate

A PDF of this thesis can be downloaded from: http://www.teses.usp.br/teses/disponiveis/44/44141/tde-22122015-144856/pt-br.php

Shubhra Sharma

Palaeo Landslide-Induced Damming and the Resultant Geomorphic Landscape: Case Study of the Middle Satluj Valley near Sunni/Tattapani (Shimla/Mandi Districts), Himachal Pradesh, India

October 2016

Himachal Pradesh University, Dept. of Geography, Shimla, India
Wadia Institute of Himalayan Geology, Dehradun, India

Degree: Ph.D.

Supervisors: Prof. B.S. Marh and Dr. S.K. Bartarya

Fluvial landforms in the Himalaya have been widely investigated to understand relationship between monsoon variability and fluvial dynamics. There are studies on the genesis and climatic significance of fluvial terraces, debris flows, alluvial fans, landslides, epigenetic gorges, and paleo-flood deposits. However, integrating the variegated landforms particularly, the role of landslides in the landform evolution through sediment contribution, and their implications towards extreme events in the Himalayan region are yet to be demonstrated conclusively. The present study is undertaken in the middle Satluj valley, north-western Himalaya in which the geomorphic processes are modulated by the temporal changes in the Indian Summer Monsoon (ISM). Studies so far either focused on fluvial or colluvial landforms largely treating these in isolation. In the present thesis, an attempt is made to investigate yet unexplored middle segment of the river where all the landforms viz., the fluvial terraces, debris flow deposits, alluvial fans, paleo-landslide deposits, flood deposits and epigenetic gorges are studied as complete assemblage to comprehensively understand the response of fluvial system to the Late Quaternary climate variability. Given

the vulnerability of the Satluj River in recent times to the landslides and landslide induced floods, an attempt is made to understand the processes responsible for paleo-landslides and floods. Thus, the specific objectives of the thesis were (i) to understand the genesis of various landforms in the middle Satluj valley in the Late Quaternary with respect to climate variability and steady-state tectonic processes. (ii) Decipher the role played by paleo-landslides towards valley aggradation, river damming and consequent flooding. (iii) Finally, to build a comprehensive understanding of the landform evolution in the study area.

In the thesis detailed geomorphological mapping supported by sedimentology, stratigraphy and geochemistry is employed. The chronology relied upon the optically stimulated dating (OSL) dating technique on the quartz extract. Chronology constitute one of the major components of the thesis, where OSL dating of the Himalayan quartz is a challenge due to low sensitivity, feldspar contamination and heterogeneous bleaching. This was circumvented by subjecting the quartz to magnetic separation to remove the detrital feldspar contamination. While the contribution from feldspar inclusions in the luminescence signal was checked by employing the Infrared Stimulation step before the Blue Light Stimulated Luminescence (BGSL). The above techniques yielded reasonably clean OSL ages which were used to interpret the climatic events, their regional and global correlations and finally reconstruction of chronologically constrained landscape evolution model.

The study suggests that the fluvial landforms have evolved on a much older pre-existing substratum ($>$100 ka), carved over multiple cycles of erosion and deposition. The majority of the floods in the catchment occurred during transitional/moderate climate, when neither the ISM nor the westerlies were strengthened. The flood phases are clustered between 13-11 ka; 8-4 ka; 4-2 ka; and after 2 ka respectively for which the landslide lake outburst (LLOFs) in the Higher and the Trans-Himalayan catchment of the Satluj River is implicated during the interaction between the ISM and mid-latitude westerlies caused due to the negative Arctic Oscillation (-AO) implying a close coupling between the Himalayan floods and northern Atlantic climatic perturbations.

The optical chronology of the oldest preserved fluvial landforms indicate that the aggradation occurred between 18 and 8 ka and is ascribed to the post LGM strengthening of ISM. The study indicates that contribution from the tributary valleys increased significantly during the transitional climate which is dated to $\sim$12 ka and 9 ka. The younger sediments are dated between $\sim$6 ka and $\sim$0.4 ka. To summarize the chronology suggests that i) variability in ISM controls the sediment mobilisation and deposition on pre-existing surface which is at least $>$100 ka. (ii) The floods were caused due to a combination of the ISM, westerlies and AO and compares well with the major flood events across the mid-latitude regions in the world. iii) The valley-fill aggradation occurred during the strengthened monsoon conditions; where hill-slope processes contribute significantly to sediment supply especially in thrust zones through paleo-landslides, alluvial fans and debris flows. The incision occurred during relatively dry phases when the sediment supply in the system exhausted.

Bibliography

Compiled by Sebastien Huot

From 15th May 2016 to 30th November 2016

Alexanderson, H., Bernhardson, M., 2016. OSL dating and luminescence characteristics of aeolian deposits and their source material in Dalarna, central Sweden. Boreas 45, 876-893, http://dx.doi.org/10.1111/bor.12197.

Anderson, A., Stothert, K., Martinsson-Wallin, H., Wallin, P., Flett, I., Haberle, S., Heijnis, H., Rhodes, E., 2016. Reconsidering Precolumbian Human Colonization in the Galápagos Islands, Republic of Ecuador. Latin American Antiquity 27, 169-183, http://dx.doi.org/10.7183/1045-6635.27.2.169.

Ankjærgaard, C., Guralnik, B., Buylaert, J.P., Reimann, T., Yi, S.W., Wallinga, J., 2016. Violet stimulated luminescence dating of quartz from Luochuan (Chinese loess plateau): Agreement with independent chronology up to ~600 ka. Quaternary Geochronology 34, 33-46, http://dx.doi.org/10.1016/j.quageo.2016.03.001.

Antinao, J.L., McDonald, E., Rhodes, E.J., Brown, N., Barrera, W., Gosse, J.C., Zimmermann, S., 2016. Late Pleistocene-Holocene alluvial stratigraphy of southern Baja California, Mexico. Quaternary Science Reviews 146, 161-181, http://dx.doi.org/10.1016/j.quascirev.2016.06.008.

Antoine, P., Moncel, M.-H., Limondin-Lozouet, N., Locht, J.-L., Bahain, J.-J., Moreno, D., Voinchet, P., Auguste, P., Stoetzel, E., Dabkowski, J., Bello, S.M., Parfitt, S.A., Tombret, O., Hardy, B., 2016. Palaeoenvironment and dating of the Early Acheulean localities from the Somme River basin (Northern France): New discoveries from the High Terrace at Abbeville-Carrière Carpentier. Quaternary Science Reviews 149, 338-371, http://dx.doi.org/10.1016/j.quascirev.2016.07.035.

Arnold, L.J., Duval, M., Demuro, M., Spooner, N.A., Santonja, M., Pérez-González, A., 2016. OSL dating of individual quartz 'supergrains' from the Ancient Middle Palaeolithic site of Cuesta de la Bajada, Spain. Quaternary Geochronology 36, 78-101, http://dx.doi.org/10.1016/j.quageo.2016.07.003.

Bailiff, I.K., Sholom, S., McKeever, S.W.S., 2016. Retrospective and emergency dosimetry in response to radiological incidents and nuclear mass-casualty events: A review. Radiation Measurements 94, 83-139, http://dx.doi.org/10.1016/j.radmeas.2016.09.004.

Barlow, N.L.M., Bentley, M.J., Spada, G., Evans, D.J.A., Hansom, J.D., Brader, M.D., White, D.A., Zander, A., Berg, S., 2016. Testing models of ice cap extent, South Georgia, sub-Antarctic. Quaternary Science Reviews 154, 157-168, http://dx.doi.org/10.1016/j.quascirev.2016.11.007.

Barton, R.N.E., Bouzouggar, A., Collcutt, S.N., Carrión Marco, Y., Clark-Balzan, L., Debenham, N.C., Morales, J., 2016. Reconsidering the MSA to LSA transition at Taforalt Cave (Morocco) in the light of new multi-proxy dating evidence. Quaternary International 413, Part A, 36-49, http://dx.doi.org/10.1016/j.quaint.2015.11.085.

Batbaatar, J., Gillespie, A.R., 2016. Outburst floods of the Maly Yenisei. Part II – new age constraints from Darhad basin. International Geology Review 58, 1753-1779, http://dx.doi.org/10.1080/00206814.2016.1193452.

Biernacka, M., Majgier, R., Maternicki, K., Liang, M., Mandowski, A., 2016. Peculiarities of optically stimulated luminescence in halite. Radiation Measurements 90, 247-251, http://dx.doi.org/10.1016/j.radmeas.2016.02.022.

Blasi, A.M., Latorre, C.C., Cusminsky, G.C., Carignano, A.P., 2016. The Marine Isotopic Stage 3 (MIS 3) in Valleys of the Undulated Pampa, Buenos Aires Province, Argentina, in: Gasparini, M.G., Rabassa, J., Deschamps, C., Tonni, P.E. (Eds.), Marine Isotope Stage 3 in Southern South America, 60 KA B.P.-30 KA B.P. Springer International Publishing, Cham, pp. 129-146.

Borella, J., Quigley, M., Sohbati, R., Almond, P., Gravley, D.M., Murray, A., 2016. Chronology and processes of late Quaternary hillslope sedimentation in the eastern South Island, New Zealand. Journal of Quaternary Science 31, 691-712, http://dx.doi.org/10.1002/jqs.2905.

Borombovits, D.K., Streed, E.W., Pietsch, T.J., Olley, J.M., 2016. Spectral signature of single-grain quartz using a high-sensitivity TL imaging system. Radiation Measurements 95, 1-8, http://dx.doi.org/10.1016/j.radmeas.2016.10.002.

Bortolussi, C., Zoleo, A., Maritan, L., Collauto, A., Brustolon, M., Marrale, M., Parlato, A., Usai, D., 2016. Electron Paramagnetic Resonance and petrographic analysis for dating Mesolithic and Neolithic pottery from Al Khiday (Sudan). Radiation Measurements 89, 89-98, http://dx.doi.org/10.1016/j.radmeas.2016.03.008.

Brill, D., Jankaew, K., Brückner, H., 2016. Towards increasing the spatial resolution of luminescence chronologies – Portable luminescence reader measurements and standardized growth curves applied to a beach-ridge plain (Phra Thong, Thailand). Quaternary Geochronology 36, 134-147, http://dx.doi.org/10.1016/j.quageo.2016.09.003.

Bristow, C.S., Armitage, S.J., 2016. Dune ages in the sand deserts of the southern Sahara and Sahel. Quaternary International 410, Part B, 46-57, http://dx.doi.org/10.1016/j.quaint.2015.07.062.

Bullón, T., 2016. The upper Pleistocene on the northern face of the Guadarrama Mountains (central Spain): Palaeoclimatic phases and glacial activity. Geomorphology 268, 233-245, http://dx.doi.org/10.1016/j.geomorph.2016.06.015.

Burbidge, C.I., Cardoso, J., Cardoso, G.O., Franco, J., Santos, L., Caldeira, M., 2016. Parallel calibration transfer and systematic effects in retrospective absorbed dose estimation using OSL. Quaternary Geochronology 34, 92-101, http://dx.doi.org/10.1016/j.quageo.2016.04.001.

Cesta, J.M., Ward, D.J., 2016. Timing and nature of alluvial fan development along the Chajnantor Plateau, northern Chile. Geomorphology 273, 412-427, http://dx.doi.org/10.1016/j.geomorph.2016.09.003.

Chahid, D., Boudad, L., Lenoble, A., El Hmaidi, A., Chakroun, A., Jacobs, Z., 2016. Nouvelles données morpho-stratigraphiques et géochronologiques sur le cordon littoral externe (SIM 5-c) de Rabat–Témara, Maroc. Géomorphologie : relief, processus, environnement 22, 253-264, http://dx.doi.org/10.4000/geomorphologie.11419.

Chen, R., Pagonis, V., Lawless, J.L., 2016a. Evaluated thermoluminescence trapping parameters–What do they really mean? Radiation Measurements 91, 21-27, http://dx.doi.org/10.1016/j.radmeas.2016.04.006.

Chen, Y., Aitchison, J.C., Zong, Y., Li, S.-H., 2016b. OSL dating of past lake levels for a large dammed lake in southern Tibet and determination of possible controls on lake evolution. Earth Surface Processes and Landforms 41, 1467-1476, http://dx.doi.org/10.1002/esp.3907.

Chiba, T., Endo, K., Sugai, T., Haraguchi, T., Kondo, R., Kubota, J., 2016. Reconstruction of Lake Balkhash levels and precipitation/evaporation changes during the last 2000 years from fossil diatom assemblages. Quaternary International 397, 330-341, http://dx.doi.org/10.1016/j.quaint.2015.08.009.

Clark-Balzan, L., 2016. Source and characteristics of blue, infrared (IR), and post-IR IR stimulated signals from gypsum-rich samples. Ancient TL 34, 6-13.

Costa, P.J.M., Costas, S., González-Villanueva, R., Oliveira, M.A., Roelvink, D., Andrade, C., Freitas, M.C., Cunha, P.P., Martins, A., Buylaert, J.P., Murray, A., 2016. How did the AD 1755 tsunami impact on sand barriers across the southern coast of Portugal? Geomorphology 268, 296-311, http://dx.doi.org/10.1016/j.geomorph.2016.06.019.

Cremon, É.H., Rossetti, D.d.F., Sawakuchi, A.d.O., Cohen, M.C.L., 2016. The role of tectonics and climate in the late Quaternary evolution of a northern Amazonian River. Geomorphology 271, 22-39, http://dx.doi.org/10.1016/j.geomorph.2016.07.030.

Cunningham, A.C., 2016. External beta dose rates to mineral grains in shell-rich sediment. Ancient TL 34, 1-5.

Dalton, A.S., Finkelstein, S.A., Barnett, P.J., Forman, S.L., 2016. Constraining the Late Pleistocene history of the Laurentide Ice Sheet by dating the Missinaibi Formation, Hudson Bay Lowlands, Canada. Quaternary Science Reviews 146, 288-299, http://dx.doi.org/10.1016/j.quascirev.2016.06.015.

Das, A., Bhattacharya, F., Rastogi, B.K., Chauhan, G., Ngangom, M., Thakkar, M.G., 2016. Response of a dryland fluvial system to climate–tectonic perturbations during the Late Quaternary: Evidence from Rukmawati River basin, Kachchh, western India. Journal of Earth System Science, 1-20, http://dx.doi.org/10.1007/s12040-016-0733-7.

de Carvalho Faria Lima Lopes, L., de Almeida Prado Bacellar, L., Amorim Castro, P.d.T., 2016. Assessment of the debris-flow susceptibility in tropical mountains using clast distribution patterns. Geomorphology 275, 16-25, http://dx.doi.org/10.1016/j.geomorph.2016.09.026.

del Valle, L., Gómez-Pujol, L., Fornós, J.J., Timar-Gabor, A., Anechitei–Deacu, V., Pomar, F., 2016. Middle to Late Pleistocene dunefields in rocky coast settings at Cala Xuclar (Eivissa, Western Mediterranean): Recognition, architecture and luminescence chronology. Quaternary International 407, Part A, 4-13, http://dx.doi.org/10.1016/j.quaint.2016.01.050.

Desruelles, S., Fouache, E., Eddargach, W., Cammas, C., Wattez, J., Beuzen-Waller, T., Martin, C., Tengberg, M., Cable, C., Thornton, C., Murray, A., 2016. Evidence for early irrigation at Bat (Wadi Sharsah, northwestern Oman) before the advent of farming villages. Quaternary Science Reviews 150, 42-54, http://dx.doi.org/10.1016/j.quascirev.2016.08.007.

Diaz, N., King, G.E., Valla, P.G., Herman, F., Verrecchia, E.P., 2016. Pedogenic carbonate nodules as soil time archives: Challenges and investigations related to OSL dating. Quaternary Geochronology 36, 120-133, http://dx.doi.org/10.1016/j.quageo.2016.08.008.

Doerschner, N., Fitzsimmons, K.E., Ditchfield, P., McLaren, S.J., Steele, T.E., Zielhofer, C., McPherron, S.P., Bouzouggar, A., Hublin, J.-J., 2016a. A New Chronology for Rhafas, Northeast Morocco, Spanning the North African Middle Stone Age through to the Neolithic. PLoS ONE 11, e0162280, http://dx.doi.org/10.1371/journal.pone.0162280.

Doerschner, N., Hernandez, M., Fitzsimmons, K.E., 2016b. Sources of variability in single grain dose recovery experiments: Insights from Moroccan and Australian samples. Ancient TL 34, 14-25.

Dolan, J.F., McAuliffe, L.J., Rhodes, E.J., McGill, S.F., Zinke, R., 2016. Extreme multi-millennial slip rate variations on the Garlock fault, California: Strain super-cycles, potentially time-variable fault strength, and implications for system-level earthquake occurrence. Earth and Planetary Science Letters 446, 123-136, http://dx.doi.org/10.1016/j.epsl.2016.04.011.

Dortch, J., Cupper, M., Grün, R., Harpley, B., Lee, K., Field, J., 2016. The timing and cause of megafauna mass deaths at Lancefield Swamp, south-eastern Australia. Quaternary Science Reviews 145, 161-182, http://dx.doi.org/10.1016/j.quascirev.2016.05.042.

Du, S., Li, B., Chen, M., Xiang, R., Niu, D., Si, Y., 2016. Paleotempestology evidence recorded by eolian deposition in the Bohai Sea coastal zone during the last interglacial period. Marine Geology 379, 78-83, http://dx.doi.org/10.1016/j.margeo.2016.05.013.

Duller, G.A.T., 2016. Challenges involved in obtaining luminescence ages for long records of aridity: Examples from the Arabian Peninsula. Quaternary International 410, Part B, 69-74, http://dx.doi.org/10.1016/j.quaint.2016.01.028.

Eccleshall, S.V., Hormes, A., Hovland, A., Preusser, F., 2016. Constraining the chronology of Pleistocene glaciations on Svalbard: Kapp Ekholm re-visited. Boreas 45, 790-803, http://dx.doi.org/10.1111/bor.12191.

Fattahi, M., Heidary, M., Ghasemi, M., 2016. Employing Minimum age model (MAM) and Finite mixture modeling (FMM) for OSL age determination of two important samples from Ira Trench of North Tehran Fault. geochr 43-47, 38, http://dx.doi.org/10.1515/geochr-2015-0031.

Faulkner, D.J., Larson, P.H., Jol, H.M., Running, G.L., Loope, H.M., Goble, R.J., 2016. Autogenic incision and terrace formation resulting from abrupt late-glacial base-level fall, lower Chippewa River, Wisconsin, USA. Geomorphology 266, 75-95, http://dx.doi.org/10.1016/j.geomorph.2016.04.016.

Forman, S.L., Waters, M.R., 2016. Optically Stimulated Luminescence Dating and the Peopling of the Americas. PaleoAmerica 2, 6-10, http://dx.doi.org/10.1080/20555563.2015.1136722.

Friedrich, J., Kreutzer, S., Schmidt, C., 2016. Solving ordinary differential equations to understand luminescence: 'RLumModel', an advanced research tool for simulating luminescence in quartz using R. Quaternary Geochronology 35, 88-100, http://dx.doi.org/10.1016/j.quageo.2016.05.004.

Gaspar, R., Ferreira, J., Carrondo, J., Silva, M.J., García-Vadillo, F.J., 2016. Open-air Gravettian lithic assemblages from Northeast Portugal: The Foz do Medal site (Sabor valley). Quaternary International 406, Part A, 44-64, http://dx.doi.org/10.1016/j.quaint.2015.12.054.

Gonçalves Júnior, E.S., Soares, E.A.A., Tatumi, S.H., Yee, M., Mittani, J.C.R., 2016. Pleistocene-Holocene sedimentation of Solimões-Amazon fluvial system between the tributaries Negro and Madeira, Central Amazon. Brazilian Journal of Geology 46, 167-180.

Gribenski, N., 2016. Comparison of dating methods for paleoglacial reconstruction in Central Asia, Department of Physical Geography. Stockholm University.

Guo, Y.-J., Li, B., Zhang, J.-F., Yuan, B.-Y., Xie, F., Roberts, R.G., 2016a. Luminescence ages for three 'Middle Palaeolithic' sites in the Nihewan Basin, northern China, and their archaeological and palaeoenvironmental implications. Quaternary Research 85, 456-470, http://dx.doi.org/10.1016/j.yqres.2016.03.002.

Guo, Y., Huang, C.C., Zhou, Y., Pang, J., Zha, X., Zhou, L., Mao, P., 2016b. Extraordinary flood events and the response to monsoonal climatic change during the last 3000 years along the middle Yangtze River valley, China. Palaeogeography, Palaeoclimatology, Palaeoecology 462, 70-84, http://dx.doi.org/10.1016/j.palaeo.2016.09.005.

Halfen, A.F., Lancaster, N., Wolfe, S., 2016. Interpretations and common challenges of aeolian records from North American dune fields. Quaternary International 410, Part B, 75-95, http://dx.doi.org/10.1016/j.quaint.2015.03.003.

Hamdan, M.A., Ibrahim, M.I.A., Shiha, M.A., Flower, R.J., Hassan, F.A., Eltelet, S.A.M., 2016. An exploratory Early and Middle Holocene sedimentary record with palynoforms and diatoms from Faiyum lake, Egypt. Quaternary International 410, Part A, 30-42, http://dx.doi.org/10.1016/j.quaint.2015.12.049.

Hansen, J.M., Aagaard, T., Stockmarr, J., Møller, I., Nielsen, L., Binderup, M., Larsen, J.H., Larsen, B., 2016. Continuous record of Holocene sea-level changes and coastal development of the Kattegat island Læsø (4900 years BP to present). Bulletin of the Geological Society of Denmark 64, 1-55.

Harder, W., 2016. Testing the Meuse terrace chronology in northern Limburg using optically stimulated luminescence dating. Wageningen University.

Hardt, J., Lüthgens, C., Hebenstreit, R., Böse, M., 2016. Geochronological (OSL) and geomorphological investigations at the presumed Frankfurt ice marginal position in northeast Germany. Quaternary Science Reviews 154, 85-99, http://dx.doi.org/10.1016/j.quascirev.2016.10.015.

Heerema, C.J., 2016. Luminescence Dating of Submarine Canyons: Application to the Monterey Canyon, California, Department of Earth Sciences. Uppsala University.

Hesse, P.P., 2016. How do longitudinal dunes respond to climate forcing? Insights from 25 years of luminescence dating of the Australian desert dunefields. Quaternary International 410, Part B, 11-29, http://dx.doi.org/10.1016/j.quaint.2014.02.020.

Hickin, A.S., Lian, O.B., Levson, V.M., 2016. Coalescence of late Wisconsinan Cordilleran and Laurentide ice sheets east of the Rocky Mountain Foothills in the Dawson Creek region, northeast British Columbia, Canada. Quaternary Research 85, 409-429, http://dx.doi.org/10.1016/j.yqres.2016.02.005.

Hu, G., Huang, C.C., Zhou, Y., Pang, J., Zha, X., Guo, Y., Zhang, Y., Zhao, X., 2016a. Hydrological studies of the historical and palaeoflood events on the middle Yihe River, China. Geomorphology 274, 152-161, http://dx.doi.org/10.1016/j.geomorph.2016.09.004.

Hu, G., Yi, C.-L., Zhang, J.-F., Liu, J.-H., Jiang, T., Li, S.-H., 2016b. Late Quaternary glacial advances in the eastern Qilianshan, north-eastern Tibet, as inferred from luminescence dating of fluvioglacial sediments. Journal of Quaternary Science 31, 587-597, http://dx.doi.org/10.1002/jqs.2882.

Hudson, A.M., Olsen, J.W., Quade, J., Lei, G., Huth, T.E., Zhang, H., 2016. A regional record of expanded Holocene wetlands and prehistoric human occupation from paleowetland deposits of the western Yarlung Tsangpo valley, southern Tibetan Plateau. Quaternary Research 86, 13-33, http://dx.doi.org/10.1016/j.yqres.2016.04.001.

Hughes, A.L.C., Gyllencreutz, R., Lohne, Ø.S., Mangerud, J., Svendsen, J.I., 2016. The last Eurasian ice sheets – a chronological database and time-slice reconstruction, DATED-1. Boreas 45, 1-45, http://dx.doi.org/10.1111/bor.12142.

Ideker, C.J., 2016. A Light in the Dark: Luminescence Dating Intermountain Ware Ceramics from Four Archaeological Sites in Northwestern Wyoming, Anthropology. Utah State University.

Jacobs, Z., Jankowski, N.R., Dibble, H.L., Goldberg, P., McPherron, S.J.P., Sandgathe, D., Soressi, M., 2016. The age of three Middle Palaeolithic sites: Single-grain optically stimulated luminescence chronologies for Pech de l'Azé I, II and IV in France. Journal of Human Evolution 95, 80-103, http://dx.doi.org/10.1016/j.jhevol.2016.03.010.

Jankowski, N.R., Gully, G.A., Jacobs, Z., Roberts, R.G., Prideaux, G.J., 2016. A late Quaternary vertebrate deposit in Kudjal Yolgah Cave, south-western Australia: refining regional late Pleistocene extinctions. Journal of Quaternary Science 31, 538-550, http://dx.doi.org/10.1002/jqs.2877.

Jiang, D., Zhang, S., Li, W., 2016. Research on the Quaternary fluvial geomorphological surface sequence of the foreland region in southern Longmen Shan, eastern Tibet. Geomorphology 269, 133-148, http://dx.doi.org/10.1016/j.geomorph.2016.06.036.

Jin, J., Li, Z., Jiang, F., Deng, T., Hu, F.g., Ling, Z., 2016. Coastal environment of the past millennium recorded by a coastal dune in Fujian, China. Journal of Arid Land, 1-15, http://dx.doi.org/10.1007/s40333-016-0053-4.

Kalińska-Nartiša, E., Alexanderson, H., Nartišs, M., 2016a. Luminescence dating of aeolian–coastal events on the Kristianstad plain, SE Sweden. The Holocene, http://dx.doi.org/10.1177/0959683616652707.

Kalińska-Nartiša, E., Thiel, C., Nartišs, M., Buylaert, J.-P., Murray, A.S., 2016b. The north-eastern aeolian 'European Sand Belt' as potential record of environmental changes: A case study from Eastern Latvia and Southern Estonia. Aeolian Research 22, 59-72, http://dx.doi.org/10.1016/j.aeolia.2016.06.002.

Kalita, J.M., Wary, G., 2016b. Thermoluminescence response of natural white quartz collected from Gelephu, Bhutan. Nuclear Instruments and Methods in Physics Research Section B: Beam Interactions with Materials and Atoms 383, 177-182, http://dx.doi.org/10.1016/j.nimb.2016.07.012.

Kalita, J.M., Wary, G., 2016c. X-ray dose response of calcite—A comprehensive analysis for optimal application in TL dosimetry. Nuclear Instruments and Methods in Physics Research Section B: Beam Interactions with Materials and Atoms 383, 93-102, http://dx.doi.org/10.1016/j.nimb.2016.06.018.

Kijek, N., Chruścińska, A., 2016. Natural and laboratory OSL growth curve–Verification of the basic assumption of luminescence dating. Radiation Measurements 90, 233-237, http://dx.doi.org/10.1016/j.radmeas.2016.01.024.

King, G.E., Guralnik, B., Valla, P.G., Herman, F., 2016. Trapped-charge thermochronometry and thermometry: A status review. Chemical Geology 446, 3-17, http://dx.doi.org/10.1016/j.chemgeo.2016.08.023.

Klasen, N., Fiebig, M., Preusser, F., 2016. Applying luminescence methodology to key sites of Alpine glaciations in Southern Germany. Quaternary International 420, 249-258, http://dx.doi.org/10.1016/j.quaint.2015.11.023.

Knabb, K.A., Erel, Y., Tirosh, O., Rittenour, T., Laparidou, S., Najjar, M., Levy, T.E., 2016. Environmental impacts of ancient copper mining and metallurgy: Multi-proxy investigation of human-landscape dynamics in the Faynan valley, southern Jordan. Journal of Archaeological Science 74, 85-101, http://dx.doi.org/10.1016/j.jas.2016.09.003.

Kothyari, G.C., Luirei, K., 2016. Late Quaternary tectonic landforms and fluvial aggradation in the Saryu River valley: Central Kumaun Himalaya. Geomorphology 268, 159-176, http://dx.doi.org/10.1016/j.geomorph.2016.06.010.

Koul, D.K., Pagonis, V., Patil, P., 2016a. Reliability of single aliquot regenerative protocol (SAR) for dose estimation in quartz at different burial temperatures: A simulation study. Radiation Measurements 91, 28-35, http://dx.doi.org/10.1016/j.radmeas.2016.04.002.

Koul, D.K., Polymeris, G.S., Soni, A., Kulkarni, M.S., 2016b. Impact of firing on the OSL luminescence properties of natural quartz: A case study. Nuclear Instruments and Methods in Physics Research Section B: Beam Interactions with Materials and Atoms 370, 86-93, http://dx.doi.org/10.1016/j.nimb.2016.01.018.

Krajcarz, M.T., Cyrek, K., Krajcarz, M., Mroczek, P., Sudoł, M., Szymanek, M., Tomek, T., Madeyska, T., 2016a. Loess in a cave: Lithostratigraphic and correlative value of loess and loess-like layers in caves from the Kraków-Częstochowa Upland (Poland). Quaternary International 399, 13-30, http://dx.doi.org/10.1016/j.quaint.2015.08.069.

Krajcarz, M.T., Kot, M., Pavlenok, K., Fedorowicz, S., Krajcarz, M., Lazarev, S.Y., Mroczek, P., Radzhabov, A., Shnaider, S., Szymanek, M., Szymczak, K., 2016b. Middle Paleolithic sites of Katta Sai in western Tian Shan piedmont, Central Asiatic loess zone: Geoarchaeological investigation of the site formation and the integrity of the lithic assemblages. Quaternary International 399, 136-150, http://dx.doi.org/10.1016/j.quaint.2015.07.051.

Krauß, L., Zens, J., Zeeden, C., Schulte, P., Eckmeier, E., Lehmkuhl, F., 2016. A Multi-Proxy Analysis of two Loess-Paleosol Sequences in the Northern Harz Foreland, Germany. Palaeogeography, Palaeoclimatology, Palaeoecology 461, 401-417, http://dx.doi.org/10.1016/j.palaeo.2016.09.001.

Lamothe, M., 2016. Luminescence dating of interglacial coastal depositional systems: Recent developments and future avenues of research. Quaternary Science Reviews 146, 1-27, http://dx.doi.org/10.1016/j.quascirev.2016.05.005.

Lancaster, N., Wolfe, S., Thomas, D., Bristow, C., Bubenzer, O., Burrough, S., Duller, G., Halfen, A., Hesse, P., Roskin, J., Singhvi, A., Tsoar, H., Tripaldi, A., Yang, X., Zárate, M., 2016. The INQUA Dunes Atlas chronologic database. Quaternary International 410, Part B, 3-10, http://dx.doi.org/10.1016/j.quaint.2015.10.044.

Layzell, A.L., Mandel, R.D., Rittenour, T.M., Smith, J.J., Harlow, R.H., Ludvigson, G.A., 2016. Stratigraphy, morphology, and geochemistry of late Quaternary buried soils on the High Plains of southwestern Kansas, USA. CATENA 144, 45-55, http://dx.doi.org/10.1016/j.catena.2016.05.003.

Lebrun, B., Chantal, T., Benoît, C., Michel, R., Laurent, L., Alice, L., Irka, H., Abdoulaye, C., Norbert, M., Éric, H., 2016. Establishing a West African chrono-cultural framework: First luminescence dating of sedimentary formations from the Falémé Valley, Eastern Senegal. Journal of Archaeological Science: Reports 7, 379-388, http://dx.doi.org/10.1016/j.jasrep.2016.05.001.

Li, B., Jacobs, Z., Roberts, R.G., 2016a. Investigation of the applicability of standardised growth curves for OSL dating of quartz from Haua Fteah cave, Libya. Quaternary Geochronology 35, 1-15, http://dx.doi.org/10.1016/j.quageo.2016.05.001.

Li, G., Rao, Z., Duan, Y., Xia, D., Wang, L., Madsen, D.B., Jia, J., Wei, H., Qiang, M., Chen, J., Chen, F., 2016b. Paleoenvironmental changes recorded in a luminescence dated loess/paleosol sequence from the Tianshan Mountains, arid central Asia, since the Penultimate Glaciation. Earth and Planetary Science Letters 448, 1-12, http://dx.doi.org/10.1016/j.epsl.2016.05.008.

Li, H., Yang, X., 2016. Spatial and temporal patterns of aeolian activities in the desert belt of northern China revealed by dune chronologies. Quaternary International 410, Part B, 58-68, http://dx.doi.org/10.1016/j.quaint.2015.07.015.

Li, Y., Song, Y., Lai, Z., Han, L., An, Z., 2016c. Rapid and cyclic dust accumulation during MIS 2 in Central Asia inferred from loess OSL dating and grain-size analysis. Scientific Reports 6, 32365, http://dx.doi.org/10.1038/srep32365

Liu, J., Murray, A.S., Buylaert, J.-P., Jain, M., Chen, J., Lu, Y., 2016a. Stability of fine-grained TT-OSL and post-IR IRSL signals from a c. 1 Ma sequence of aeolian and lacustrine deposits from the Nihewan Basin (northern China). Boreas 45, 703-714, http://dx.doi.org/10.1111/bor.12180.

Liu, S., Lai, Z., Wang, Y., Fan, X., Wang, L., Tian, M., Jiang, Y., Zhao, H., 2016b. Growing pattern of mega-dunes in the Badain Jaran Desert in China revealed by luminescence ages. Quaternary International 410, Part B, 111-118, http://dx.doi.org/10.1016/j.quaint.2015.09.048.

Malinsky-Buller, A., Barzilai, O., Ayalon, A., Bar-Matthews, M., Birkenfeld, M., Porat, N., Ron, H., Roskin, J., Ackermann, O., 2016. The age of the Lower Paleolithic site of Kefar Menachem West, Israel—Another facet of Acheulian variability. Journal of Archaeological Science: Reports 10, 350-362, http://dx.doi.org/10.1016/j.jasrep.2016.10.010.

Mao, P., Pang, J., Huang, C., Zha, X., Zhou, Y., Guo, Y., Zhou, L., 2016. A multi-index analysis of the extraordinary paleoflood events recorded by slackwater deposits in the Yunxi Reach of the upper Hanjiang River, China. CATENA 145, 1-14, http://dx.doi.org/10.1016/j.catena.2016.05.016.

Marković, S.B., Fitzsimmons, K.E., Sprafke, T., Gavrilović, D., Smalley, I.J., Jović, V., Svirčev, Z., Gavrilov, M.B., Bešlin, M., 2016. The history of Danube loess research. Quaternary International 399, 86-99, http://dx.doi.org/10.1016/j.quaint.2015.09.071.

Matter, A., Mahjoub, A., Neubert, E., Preusser, F., Schwalb, A., Szidat, S., Wulf, G., 2016. Reactivation of the Pleistocene trans-Arabian Wadi ad Dawasir fluvial system (Saudi Arabia) during the Holocene humid phase. Geomorphology 270, 88-101, http://dx.doi.org/10.1016/j.geomorph.2016.07.013.

McCloskey, G.L., Wasson, R.J., Boggs, G.S., Douglas, M., 2016. Timing and causes of gully erosion in the riparian zone of the semi-arid tropical Victoria River, Australia: Management implications. Geomorphology 266, 96-104, http://dx.doi.org/10.1016/j.geomorph.2016.05.009.

Miao, X., Wang, H., Hanson, P.R., Mason, J.A., Liu, X., 2016. A new method to constrain soil development time using both OSL and radiocarbon dating. Geoderma 261, 93-100, http://dx.doi.org/10.1016/j.geoderma.2015.07.004.

Miller, G.H., Fogel, M.L., Magee, J.W., Gagan, M.K., 2016. Disentangling the impacts of climate and human colonization on the flora and fauna of the Australian arid zone over the past 100 ka using stable isotopes in avian eggshell. Quaternary Science Reviews 151, 27-57, http://dx.doi.org/10.1016/j.quascirev.2016.08.009.

Nimick, D.A., McGrath, D., Mahan, S.A., Friesen, B.A., Leidich, J., 2016. Latest Pleistocene and Holocene glacial events in the Colonia valley, Northern Patagonia Icefield, southern Chile. Journal of Quaternary Science 31, 551-564, http://dx.doi.org/10.1002/jqs.2847.

Olszak, J., Adamiec, G., 2016. OSL-based chronostratigraphy of river terraces in mountainous areas, Dunajec basin, West Carpathians: a revision of the climatostratigraphical approach. Boreas 45, 483-493, http://dx.doi.org/10.1111/bor.12163.

Ozturk, M.Z., Erginal, A.E., Kiyak, N.G., Demirci, A., Ekinci, Y.L., Curebal, İ., Avcıoglu, M., Ozturk, T., 2016. Records of repeated drought stages during the Holocene, Lake Iznik (Turkey) with reference to beachrock. Quaternary International 408, Part A, 16-24, http://dx.doi.org/10.1016/j.quaint.2015.08.077.

Palamakumbura, R.N., Robertson, A.H.F., Kinnaird, T.C., van Calsteren, P., Kroon, D., Tait, J.A., 2016. Quantitative dating of Pleistocene deposits of the Kyrenia Range, northern Cyprus: implications for timing, rates of uplift and driving mechanisms. Journal of the Geological Society, http://dx.doi.org/10.1144/jgs2015-130.

Panno, S.V., Chirienco, M.I., Bauer, R.A., Lundstrom, C.C., Zhang, Z., Hackley, K.C., 2016. Possible Earthquakes Recorded in Stalagmites from a Cave in South-Central Indiana. Bulletin of the Seismological Society of America 106, 2364-2375, http://dx.doi.org/10.1785/0120150240.

Pederson, J.L., Janecke, S.U., Reheis, M.C., Kaufman, D.S., Oaks Jr, R.Q., 2016. Chapter 2 - The Bear River's History and Diversion: Constraints, Unsolved Problems, and Implications for the Lake Bonneville Record, Volume 20. in: Charles, G.O., John, F.S. (Eds.), Developments in Earth Surface Processes. Elsevier, pp. 28-59.

Pellicer, X.M., Corella, J.P., Gutiérrez, F., Roqué, C., Linares, R., Carbonel, D., Zarroca, M., Guerrero, J., Comas, X., 2016. Sedimentological and palaeohydrological characterization of Late Pleistocene and Holocene tufa mound palaeolakes using trenching methods in the Spanish Pyrenees. Sedimentology 63, 1786-1819, http://dx.doi.org/10.1111/sed.12290.

Peng, J., Dong, Z., Han, F., 2016a. Optically stimulated luminescence dating of sandy deposits from Gulang county at the southern margin of the Tengger Desert, China. Journal of Arid Land 8, 1-12, http://dx.doi.org/10.1007/s40333-015-0137-6.

Peng, J., Dong, Z., Han, F., Gao, L., 2016b. Aeolian activity in the south margin of the Tengger Desert in northern China since the Late Glacial Period revealed by luminescence chronology. Palaeogeography, Palaeoclimatology, Palaeoecology 457, 330-341, http://dx.doi.org/10.1016/j.palaeo.2016.06.028.

Peng, J., Pagonis, V., Li, B., 2016c. On the intrinsic accuracy and precision of the standardised growth curve (SGC) and global-SGC (gSGC) methods for equivalent dose determination: A simulation study. Radiation Measurements 94, 53-64, http://dx.doi.org/10.1016/j.radmeas.2016.09.006.

Polymeris, G.S., 2016. Thermally assisted OSL (TA-OSL) from various luminescence phosphors; an overview. Radiation Measurements 90, 145-152, http://dx.doi.org/10.1016/j.radmeas.2016.01.035.

Pope, R.J.J., Candy, I., Skourtsos, E., 2016. A chronology of alluvial fan response to Late Quaternary sea level and climate change, Crete. Quaternary Research 86, 170-183, http://dx.doi.org/10.1016/j.yqres.2016.06.003.

Portenga, E.W., Bishop, P., Gore, D.B., Westaway, K.E., 2016a. Landscape preservation under post-European settlement alluvium in the south-eastern Australian tablelands, inferred from portable OSL reader data. Earth Surface Processes and Landforms 41, 1697-1707, http://dx.doi.org/10.1002/esp.3942.

Portenga, E.W., Westaway, K.E., Bishop, P., 2016b. Timing of post-European settlement alluvium deposition in SE Australia: A legacy of European land-use in the Goulburn Plains. The Holocene 26, 1472-1485, http://dx.doi.org/10.1177/0959683616640047.

Prasad, A.K., Lapp, T., Kook, M., Jain, M., 2016. Probing luminescence centers in Na rich feldspar. Radiation Measurements 90, 292-297, http://dx.doi.org/10.1016/j.radmeas.2016.02.033.

Preoteasa, L., Vespremeanu-Stroe, A., Tătui, F., Zăinescu, F., Timar-Gabor, A., Cîrdan, I., 2016. The evolution of an asymmetric deltaic lobe (Sf. Gheorghe, Danube) in association with cyclic development of the river-mouth bar: Long-term pattern and present adaptations to human-induced sediment depletion. Geomorphology 253, 59-73, http://dx.doi.org/10.1016/j.geomorph.2015.09.023.

Przegiętka, K., Molewski, P., Juśkiewicz, W., Palczewski, P., Chabowski, M., 2016. OSL dating of modern fluvial sediments in the lower Vistula River: testing zeroing assumption. Bulletin of Geography 10, 107-121.

Pupim, F.d.N., Sawakuchi, A.O., Mineli, T.D., Nogueira, L., 2016. Evaluating isothermal thermoluminescence and thermally transferred optically stimulated luminescence for dating of Pleistocene sediments in Amazonia. Quaternary Geochronology 36, 28-37, http://dx.doi.org/10.1016/j.quageo.2016.08.003.

Quick, L.J., Meadows, M.E., Bateman, M.D., Kirsten, K.L., Mäusbacher, R., Haberzettl, T., Chase, B.M., 2016. Vegetation and climate dynamics during the last glacial period in the fynbos-afrotemperate forest ecotone, southern Cape, South Africa. Quaternary International 404, Part B, 136-149, http://dx.doi.org/10.1016/j.quaint.2015.08.027.

Rante, R., Fouache, E., Mirzaakhmedov, D., 2016. Dynamics of human settlements ensuing from river transformation and changes in commercial behaviour: The birth of the "North-eastern Silk Road". Journal of Archaeological Science: Reports 9, 437-447, http://dx.doi.org/10.1016/j.jasrep.2016.08.008.

Rémillard, A.M., St-Onge, G., Bernatchez, P., Hétu, B., Buylaert, J.-P., Murray, A.S., Vigneault, B., 2016. Chronology and stratigraphy of the Magdalen Islands archipelago from the last glaciation to the early Holocene: new insights into the glacial and sea-level history of eastern Canada. Boreas 45, 604-628, http://dx.doi.org/10.1111/bor.12179.

Rengers, F.K., Tucker, G.E., Mahan, S.A., 2016. Episodic bedrock erosion by gully-head migration, Colorado High Plains, USA. Earth Surface Processes and Landforms 41, 1574-1582, http://dx.doi.org/10.1002/esp.3929.

Reuther, J.D., Potter, B.A., Holmes, C.E., Feathers, J.K., Lanoë, F.B., Kielhofer, J., 2016. The Rosa-Keystone Dunes Field: The geoarchaeology and paleoecology of a late Quaternary stabilized dune field in Eastern Beringia. The Holocene, http://dx.doi.org/10.1177/0959683616646190.

Rodrigues, K., Rink, W.J., Collins, M.B., Williams, T.J., Keen-Zebert, A., López, G.I., 2016. OSL ages of the Clovis, Late Paleoindian, and Archaic components at Area 15 of the Gault Site, Central Texas, U.S.A. Journal of Archaeological Science: Reports 7, 94-103, http://dx.doi.org/10.1016/j.jasrep.2016.03.014.

Ross, J., Westaway, K., Travers, M., Morwood, M.J., Hayward, J., 2016. Into the Past: A Step Towards a Robust Kimberley Rock Art Chronology. PLoS ONE 11, e0161726, http://dx.doi.org/10.1371/journal.pone.0161726.

Saikia, R.R., Amin, N., Nagar, Y.C., 2016. Dating of Paleochannel Sediment of Jorhat District of Assam, North Eastern India. International Research Journal of Engineering and Technology 3, 156-164.

Sancho, C., Calle, M., Peña-Monné, J.L., Duval, M., Oliva-Urcia, B., Pueyo, E.L., Benito, G., Moreno, A., 2016. Dating the Earliest Pleistocene alluvial terrace of the Alcanadre River (Ebro Basin, NE Spain): Insights into the landscape evolution and involved processes. Quaternary International 407, Part A, 86-95, http://dx.doi.org/10.1016/j.quaint.2015.10.050.

Sarkar, A., Mukherjee, A.D., Bera, M.K., Das, B., Juyal, N., Morthekai, P., Deshpande, R.D., Shinde, V.S., Rao, L.S., 2016. Oxygen isotope in archaeological bioapatites from India: Implications to climate change and decline of Bronze Age Harappan civilization. Scientific Reports 6, 26555, http://dx.doi.org/10.1038/srep26555.

Sauer, D., Kadereit, A., Kühn, P., Kösel, M., Miller, C.E., Shinonaga, T., Kreutzer, S., Herrmann, L., Fleck, W., Starkovich, B.M., Stahr, K., 2016. The loess-palaeosol sequence of Datthausen, SW Germany: Characteristics, chronology, and implications for the use of the Lohne Soil as a marker soil. CATENA 146, 10-29, http://dx.doi.org/10.1016/j.catena.2016.06.024.

Sawakuchi, A.O., Mendes, V.R., Pupim, F.d.N., Mineli, T.D., Ribeiro, L.M.A.L., Zular, A., Guedes, C.C.F., Giannini, P.C.F., Nogueira, L., Sallun Filho, W., Assine, M.L., 2016. Optically stimulated luminescence and isothermal thermoluminescence dating of high sensitivity and well bleached quartz from Brazilian sediments: from Late Holocene to beyond the Quaternary? Brazilian Journal of Geology 46, 209-226, http://dx.doi.org/10.1590/2317-488920160030295.

Schirrmeister, L., Meyer, H., Andreev, A., Wetterich, S., Kienast, F., Bobrov, A., Fuchs, M., Sierralta, M., Herzschuh, U., 2016. Late Quaternary paleoenvironmental records from the Chatanika River valley near Fairbanks (Alaska). Quaternary Science Reviews 147, 259-278, http://dx.doi.org/10.1016/j.quascirev.2016.02.009.

Schmidt, C., Zöller, L., 2016. Lumineszenzdatierung als Schlüssel zur Vergangenheit. Chemie in unserer Zeit 50, 188-197, http://dx.doi.org/10.1002/ciuz.201600703.

Schmidt, C., Zöller, L., Hambach, U., 2015. Dating of sediments and soils, Erlanger Geographische Arbeiten band 42. in: Bernhard, L., Bäumler, R., Schmidt, M. (Eds.), Soils and Sediments as Archives of Landscape Change. Palm und Enke Verlag, pp. 119-146.

Sharma, S., Chand, P., Bisht, P., Shukla, A.D., Bartarya, S.K., Sundriyal, Y.P., Juyal, N., 2016. Factors responsible for driving the glaciation in the Sarchu Plain, eastern Zanskar Himalaya, during the late Quaternary. Journal of Quaternary Science 31, 495-511, http://dx.doi.org/10.1002/jqs.2874.

Shellberg, J.G., Spencer, J., Brooks, A.P., Pietsch, T.J., 2016. Degradation of the Mitchell River fluvial megafan by alluvial gully erosion increased by post-European land use change, Queensland, Australia. Geomorphology 266, 105-120, http://dx.doi.org/10.1016/j.geomorph.2016.04.021.

Simkins, L.M., DeWitt, R., Simms, A.R., Briggs, S., Shapiro, R.S., 2016. Investigation of optically stimulated luminescence behavior of quartz from crystalline rock surfaces: A look forward. Quaternary Geochronology 36, 161-173, http://dx.doi.org/10.1016/j.quageo.2016.09.002.

Singh, A.K., Menon, S.N., Kadam, S.Y., Koul, D.K., Datta, D., 2016. OSL studies of local bricks for retrospective dosimetric application. Nuclear Instruments and Methods in Physics Research Section B: Beam Interactions with Materials and Atoms 383, 14-20, http://dx.doi.org/10.1016/j.nimb.2016.06.007.

Sinha, S., Sinha, R., 2016. Geomorphic evolution of Dehra Dun, NW Himalaya: Tectonics and climatic coupling. Geomorphology 266, 20-32, http://dx.doi.org/10.1016/j.geomorph.2016.05.002.

Smedley, R.K., Pearce, N.J.G., 2016. Internal U, Th and Rb concentrations of alkali-feldspar grains: Implications for luminescence dating. Quaternary Geochronology 35, 16-25, http://dx.doi.org/10.1016/j.quageo.2016.05.002.

Sohbati, R., Borella, J., Murray, A., Quigley, M., Buylaert, J.-P., 2016. Optical dating of loessic hillslope sediments constrains timing of prehistoric rockfalls, Christchurch, New Zealand. Journal of Quaternary Science 31, 678-690, http://dx.doi.org/10.1002/jqs.2895.

Sophady, H., Forestier, H., Zeitoun, V., Puaud, S., Frère, S., Celiberti, V., Westaway, K., Mourer, R., Mourer-Chauviré, C., Than, H., Billault, L., Tech, S., 2016. Laang Spean cave (Battambang province): A tale of occupation in Cambodia from the Late Upper Pleistocene to Holocene. Quaternary International 416, 162-176, http://dx.doi.org/10.1016/j.quaint.2015.07.049.

Soria-Jáuregui, Á., González-Amuchástegui, M.J., Mauz, B., Lang, A., 2016. Dynamics of Mediterranean late Quaternary fluvial activity: An example from the River Ebro (north Iberian Peninsula). Geomorphology 268, 110-122, http://dx.doi.org/10.1016/j.geomorph.2016.06.006.

Srivastava, P., Sangode, S.J., Parmar, N., Meshram, D.C., Jadhav, P., Singhvi, A.K., 2016. Mineral magnetic characteristics of the late Quaternary coastal red sands of Bheemuni, East Coast (India). Journal of Applied Geophysics 134, 77-88, http://dx.doi.org/10.1016/j.jappgeo.2016.08.005.

Stauch, G., 2016. Multi-decadal periods of enhanced aeolian activity on the north-eastern Tibet Plateau during the last 2ka. Quaternary Science Reviews 149, 91-101, http://dx.doi.org/10.1016/j.quascirev.2016.07.027.

Stevens, T., Buylaert, J.-P., Lu, H., Thiel, C., Murray, A., Frechen, M., Yi, S., Zeng, L., 2016. Mass accumulation rate and monsoon records from Xifeng, Chinese Loess Plateau, based on a luminescence age model. Journal of Quaternary Science 31, 391-405, http://dx.doi.org/10.1002/jqs.2848.

Stimpson, C.M., Lister, A., Parton, A., Clark-Balzan, L., Breeze, P.S., Drake, N.A., Groucutt, H.S., Jennings, R., Scerri, E.M.L., White, T.S., Zahir, M., Duval, M., Grün, R., Al-Omari, A., Al Murayyi, K.S.M., Zalmout, I.S., Mufarreh, Y.A., Memesh, A.M., Petraglia, M.D., 2016. Middle Pleistocene vertebrate fossils from the Nefud Desert, Saudi Arabia: Implications for biogeography and palaeoecology. Quaternary Science Reviews 143, 13-36, http://dx.doi.org/10.1016/j.quascirev.2016.05.016.

Sun, C., Wan, T., Xie, X., Shen, X., Liang, K., 2016. Knickpoint series of gullies along the Luoyunshan Piedmont and its relation with fault activity since late Pleistocene. Geomorphology 268, 266-274, http://dx.doi.org/10.1016/j.geomorph.2016.06.026.

Swezey, C.S., Fitzwater, B.A., Whittecar, G.R., Mahan, S.A., Garrity, C.P., Alemán González, W.B., Dobbs, K.M., 2016. The Carolina Sandhills: Quaternary eolian sand sheets and dunes along the updip margin of the Atlantic Coastal Plain province, southeastern United States. Quaternary Research 86, 271-286, http://dx.doi.org/10.1016/j.yqres.2016.08.007.

Thomas, D.S.G., Burrough, S.L., 2016. Luminescence-based dune chronologies in southern Africa: Analysis and interpretation of dune database records across the subcontinent. Quaternary International 410, Part B, 30-45, http://dx.doi.org/10.1016/j.quaint.2013.09.008.

Toyoda, S., Nagashima, K., Yamamoto, Y., 2016. ESR signals in quartz: Applications to provenance research – A review. Quaternary International 397, 258-266, http://dx.doi.org/10.1016/j.quaint.2015.05.048.

Tripaldi, A., Zárate, M.A., 2016. A review of Late Quaternary inland dune systems of South America east of the Andes. Quaternary International 410, Part B, 96-110, http://dx.doi.org/10.1016/j.quaint.2014.06.069.

Tsakalos, E., 2016. Geochronology and exoscopy of quartz grains in environmental determination of coastal sand dunes in SE Cyprus. Journal of Archaeological Science: Reports 7, 679-686, http://dx.doi.org/10.1016/j.jasrep.2015.11.031.

Tsakalos, E., Athanassas, C., Tsipas, P., Triantaphyllou, M., Geraga, M., Papatheodorou, G., Filippaki, E., Christodoulakis, J., Kazantzaki, M., 2016. Luminescence geochronology and paleoenvironmental implications of coastal deposits of southeast Cyprus. Archaeological and Anthropological Sciences, 1-20, http://dx.doi.org/10.1007/s12520-016-0339-7.

Turner, D.G., Ward, B.C., Froese, D.G., Lamothe, M., Bond, J.D., Bigelow, N.H., 2016. Stratigraphy of Pleistocene glaciations in the St Elias Mountains, southwest Yukon, Canada. Boreas 45, 521-536, http://dx.doi.org/10.1111/bor.12172.

Valla, P.G., Lowick, S.E., Herman, F., Champagnac, J.-D., Steer, P., Guralnik, B., 2016. Exploring IRSL50 fading variability in bedrock feldspars and implications for OSL thermochronometry. Quaternary Geochronology 36, 55-66, http://dx.doi.org/10.1016/j.quageo.2016.08.004.

van Gorp, W., Schoorl, J.M., Temme, A.J.A.M., Reimann, T., Wijbrans, J.R., Maddy, D., Demir, T., Veldkamp, T., 2016. Catchment response to lava damming: integrating field observation, geochronology and landscape evolution modelling. Earth Surface Processes and Landforms 41, 1629-1644, http://dx.doi.org/10.1002/esp.3981.

Vespremeanu-Stroe, A., Preoteasa, L., Zăinescu, F., Rotaru, S., Croitoru, L., Timar-Gabor, A., 2016. Formation of Danube delta beach ridge plains and signatures in morphology. Quaternary International 415, 268-285, http://dx.doi.org/10.1016/j.quaint.2015.12.060.

von Suchodoletz, H., Gärtner, A., Hoth, S., Umlauft, J., Sukhishvili, L., Faust, D., 2016. Late Pleistocene river migrations in response to thrust belt advance and sediment-flux steering — The Kura River (southern Caucasus). Geomorphology 266, 53-65, http://dx.doi.org/10.1016/j.geomorph.2016.04.026.

Ward, I., Salvemini, F., Veth, P., 2016. 3D visualisation and dating of an embedded chert artefact from Barrow Island. Journal of Archaeological Science: Reports 7, 432-436, http://dx.doi.org/10.1016/j.jasrep.2016.05.023.

Weisrock, A., Balescu, S., Ouammou, A., Abdessadok, S., Ghaleb, B., Rousseau, L., Huot, S., Lamothe, M., Falguères, C., 2016. Géomorphologie, stratigraphie, géochronologie et oscillations glacio-eustatiques dans le domaine de la basse terrasse côtière, à l'embouchure de l'Assif Tamraght (Baie de Tarhazout, Agadir, Maroc) pendant le MIS 5 et le MIS 4. Géomorphologie : relief, processus, environnement 22, 265-286, http://dx.doi.org/10.4000/geomorphologie.11439.

Wood, R., Jacobs, Z., Vannieuwenhuyse, D., Balme, J., O'Connor, S., Whitau, R., 2016. Towards an Accurate and Precise Chronology for the Colonization of Australia: The Example of Riwi, Kimberley, Western Australia. PLoS ONE 11, e0160123, http://dx.doi.org/10.1371/journal.pone.0160123.

Woodbridge, K.P., Parsons, D.R., Heyvaert, V.M.A., Walstra, J., Frostick, L.E., 2016. Characteristics of direct human impacts on the rivers Karun and Dez in lowland south-west Iran and their interactions with earth surface movements. Quaternary International 392, 315-334, http://dx.doi.org/10.1016/j.quaint.2015.10.088.

Wulf, S., Fedorowicz, S., Veres, D., Łanczont, M., Karátson, D., Gertisser, R., Bormann, M., Magyari, E., Appelt, O., Hambach, U., Gozhyk, P.F., 2016. The 'Roxolany Tephra' (Ukraine) − new evidence for an origin from Ciomadul volcano, East Carpathians. Journal of Quaternary Science 31, 565-576, http://dx.doi.org/10.1002/jqs.2879.

Yi, C., Bi, W., Li, J., 2016a. ESR dating of glacial moraine deposits: Some insights about the resetting of the germanium (Ge) signal measured in quartz. Quaternary Geochronology 35, 69-76, http://dx.doi.org/10.1016/j.quageo.2016.06.003.

Yi, S., Buylaert, J.-P., Murray, A.S., Lu, H., Thiel, C., Zeng, L., 2016b. A detailed post-IR IRSL dating study of the Niuyangzigou loess site in northeastern China. Boreas 45, 644-657, http://dx.doi.org/10.1111/bor.12185.

Zeeden, C., Kels, H., Hambach, U., Schulte, P., Protze, J., Eckmeier, E., Marković, S.B., Klasen, N., Lehmkuhl, F., 2016. Three climatic cycles recorded in a loess-palaeosol sequence at Semlac (Romania) – Implications for dust accumulation in south-eastern Europe. Quaternary Science Reviews 154, 130-142, http://dx.doi.org/10.1016/j.quascirev.2016.11.002.

Zhang, J., 2016. Responses of late Quaternary sediments to climate change: Luminescence dating of coastal, lacustrine and aeolian deposits from northern China and Germany. Freien Universität Berlin.

Zhou, L., Huang, C.C., Zhou, Y., Pang, J., Zha, X., Xu, J., Zhang, Y., Guo, Y., 2016. Late Pleistocene and Holocene extreme hydrological event records from slackwater flood deposits of the Ankang east reach in the upper Hanjiang River valley, China. Boreas 45, 673-687, http://dx.doi.org/10.1111/bor.12181.

Zhuang, Y., Bao, W., French, C., 2016. Loess and early land use: Geoarchaeological investigation at the early Neolithic site of Guobei, Southern Chinese Loess Plateau. CATENA 144, 151-162, http://dx.doi.org/10.1016/j.catena.2016.05.005.

Zhuo, H., Lu, H., Wang, S., Ahmad, K., Sun, W., Zhang, H., Yi, S., Li, Y., Wang, X., 2016. Chronology of newly-discovered Paleolithic artifact assemblages in Lantian (Shaanxi province), central China. Quaternary Research 86, 316-325, http://dx.doi.org/10.1016/j.yqres.2016.08.008.

Zilhão, J., Ajas, A., Badal, E., Burow, C., Kehl, M., López-Sáez, J.A., Pimenta, C., Preece, R.C., Sanchis, A., Sanz, M., Weniger, G.-C., White, D., Wood, R., Angelucci, D.E., Villaverde, V., Zapata, J., 2016. Cueva Antón: A multi-proxy MIS 3 to MIS 5a paleoenvironmental record for SE Iberia. Quaternary Science Reviews 146, 251-273, http://dx.doi.org/10.1016/j.quascirev.2016.05.038.

Zöller, L., Schmidt, C., 2016. OSL-Altersbestimmungen an den spätsaale- bis eemzeitlichen Ablagerungen von Jänschwalde. Brandenburgische Geowissenschaftliche Beiträge /Arbeitsber. Bodendenkmalpfl. Brandenburg, Sonderband 2016, 191-197.

Ancient TL

ISSN 0735-1348

Aims and Scope

Ancient TL is a journal devoted to Luminescence dating, Electron Spin Resonance (ESR) dating, and related techniques. It aims to publish papers dealing with experimental and theoretical results in this field, with a minimum of delay between submission and publication. Ancient TL also publishes a current bibliography, thesis abstracts, letters, and miscellaneous information, e.g., announcements for meetings.

Frequency

Two issues per annum in June and December

Submission of articles to Ancient TL

Ancient TL has a reviewing system in which direct dialogue is encouraged between reviewers and authors. For instructions to authors and information on how to submit to Ancient TL, please visit the website at:
http://www.ecu.edu/cs-cas/physics/ancient-timeline/ancient-tl1.cfm

Journal Enquiries

For enquiries please contact the editor:
Regina DeWitt, Department of Physics, East Carolina University, Howell Science Complex, 1000 E. 5th Street, Greenville, NC 27858, USA; Tel: +252-328-4980; Fax: +252-328-0753 (dewittr@ecu.edu)

Subscriptions to Ancient TL

Ancient TL Vol. 32 No.2 December 2014 was the last issue to be published in print. Past and current issues are available for download free of charge from the Ancient TL website:
http://www.ecu.edu/cs-cas/physics/ancient-timeline/ancient-tl5.cfm